Hot electron spectroscopy studies of indirect tunnel barriers

Sivaraya, Sivapathasundaram

Award date:
1999

Awarding institution:
University of Bath

Hot Electron Spectroscopy Studies of Indirect Tunnel Barriers

Submitted by Sivapathasundaram Sivaraya

for the degree of

Doctor of Philosophy

of the University of Bath

1999

S. Sivaraya

ProQuest LLC
789 East Eisenhower Parkway
P.O. Box 1346
Ann Arbor, MI 48106-1346

Abstract

The main goal of this thesis is to gain an understanding of electron transport through indirect AlAs potential barriers. This has been achieved by incorporating them as emitter barriers in a three-terminal Tunnelling Hot Electron Transfer Amplifier (THETA) device. Hot Electron spectroscopy was performed downstream of these barriers to measure the actual energy distribution of electrons which have passed through them.

Hot electron spectroscopy of a 15nm indirect AlAs emitter barrier transistor reveals that only about 1% of the tunnelling electrons are collected close to their injection energy in contrast to an otherwise identical structure with a nominally direct $Al_{0.5}Ga_{0.5}As$ emitter barrier where the fraction is 30%. Moreover three or four peaks could be clearly resolved in the broad background of scattered electrons in the device with the AlAs barrier.

Measurements on AlAs barrier transistor under hydrostatic pressure show clear evidence for the real space transfer of electrons from the emitter electrode into X-point states in the barrier adjacent to the emitter Fermi band. A detailed analysis reveals that the transferred electrons relax down through the ladder of X-point subbands before being reemitted into the base layer at the well defined but lower energies of the longitudinal subbands.

Acknowledgements

I would like to thank my supervisor Dr. Simon Bending for accepting me as a graduate student in his group and for his excellent supervision and scientific guidance throughout the project. He has taught me many measurement techniques and explained several theoretical concepts. I am greatly indebted to Simon for his help in getting financial support, without which this thesis would not have been possible.

It is a pleasure to take this opportunity to express my sincere gratitude to the many people who helped me.

Dr. Mohamed Henini of the School of Physics and Astronomy, University of Nottingham for providing excellent samples.

Dr. Ahmet Oral, Dr. Geoff Nash, Dr. Simon Wooton, Jonathan Pinto and Julian Cluff for teaching me the art of semiconductor fabrication.

Ms. Virginia Lam for making available her tunnelling subroutines and for her processing notes.

Dr. Alain Nogaret for his assistance with pressure cell experiments and for interesting discussions.

Mr. Bob Draper, Ms. Wendy Lambson and Mr. Ravi Rao for their technical support.

Kevin Rodgers and Mark Acres deserve special thanks for their help with computing.

I am grateful to my colleagues Graeme Moore, Dr. Hooman kazemi, Dr. Gary Howells, Matt James, Jim Patridge, Dr. Sasha Grigorenko, Jon Ipe, Jim Gregory, Alex Brook and David Lawton for their support and encouragement.

I would like to acknowledge financial support from the ORS awards scheme and the Department of Physics. I would especially like to thank Prof. David Bullett and Dr. David Parkin for their help in getting financial support from Esther Parkin

Trust. Thanks are also due to University Hardship fund committee members for the financial support during writing up.

Finally a special thanks goes to my grand father, mother and brothers for their encouragement and support over the years.

Contents

Chapter 1

Introduction

1.1 Motivation

It has been consistently demonstrated that III-V semiconductor materials (eg: GaAs) are superior to Silicon for making high-speed devices (Larson *et al.* 1986, Sekiguchi *et al.* 1992, and Kelly 1995). The superiority of GaAs comes from the fact that the electron effective mass is small at the bottom of conduction band minimum leading to a high electron velocity for a given carrier concentration. There are many GaAs-based products operating at high frequencies which are available in the market place, for example Laser diodes in CD players and the GaAs/AlGaAs High Electron Mobility Transistor (HEMT) in high frequency systems such as mobile telephones, satellite antenna sets and Global Positioning System (GPS) navigator receivers. However, there are several areas still waiting for devices operating at ever high frequency. They include astronomical observations, remote environmental monitoring, plasma analysis and anti-collision radar.

The high frequency operation of a device is fundamentally limited by the time taken by carriers to traverse the active region of the structure and the charging time (Weisbuch and Vinter 1991). For example the channel length of a Field Effect Transistor (FET) limits its high frequency operation. Due to the technological difficulties associated with sub-micron lithography there is a limit on the minimum possible size of a device based on lateral transport. The advent of modern growth technologies such as Molecular Beam Epitaxy (MBE) and Metal Organic Chemical Vapour Deposition (MOCVD) techniques opened up a way of creating barriers and

wells of very small dimensions along the growth direction. The resulting heterojunctions can be utilised to achieve transport perpendicular to the ultra-thin layers. They also offer an opportunity to build very short devices based on ballistic transport in which the scattering of carriers with impurities may be neglected (Jaros 1990).

The GaAs/ $Al_xGa_{1-x}As$ system is one of the most actively studied heterostructures. In this almost perfectly epitaxial system the barrier height can be tuned by varying the Al mole fraction in ternary $Al_xGa_{1-x}As$ (Adachi 1985). Many devices have been proposed based on the quantum transport of carriers via AlGaAs potential barriers including the three terminal hot electron transistor (Heiblum 1981), single barrier diodes (Delagebeaudeuf *et al.* 1982), double barrier resonant tunnelling diodes (Chang *et al.* 1974) and superlattice structures (Esaki and Tsu 1970). The transport processes taking place in optically direct $Al_xGa_{1-x}As$ ($x<0.45$) barriers are fairly well understood. In the case of indirect $Al_xGa_{1-x}As$ ($x>0.45$) barriers, however, the X-point conduction band minima fall below the Γ-point conduction band minimum opening up new transport channel/channels. These complex X-point related transport processes are poorly understood yet there are good reasons for using indirect AlAs barriers in a number of devices. Firstly, it is known that growth of the binary AlAs alloy on top of GaAs yields a very good interface with negligible interface roughness scattering (Landheer *et al.* 1989). Secondly, the random alloy scattering mechanism is not present in AlAs. Thirdly, the Γ-point barrier provides very strong quantum confinement provided that the X-point plays no significant role. Understanding transport through indirect AlAs barriers is therefore of great technological importance. From the academic point of view they also provide an excellent model system to investigate transport via different points in the Brillouin zone.

The transport of electrons via longitudinal X-point minima and the importance of X-point subbands in transport through AlAs barrier, have been confirmed by a number of investigations (Mendez *et al.* 1986;Bonnefoi *et al.* 1986). Hydrostatic pressure is frequently applied to the indirect AlAs barrier to change the X-point conduction band offset without altering other parameters such as the

interface quality and the Γ-point conduction band offset (Mendez *et al.* 1986, Austing *et al.* 1993, Othaman *et al.* 1993, and Carbonneau *et al.* 1993).

The scope of this thesis is to understand the electronic transport processes taking place in thin indirect AlAs barriers. In most of the previous studies transport mechanisms were deduced from current-voltage measurements performed on single barrier and double barrier structures. In the work reported in this thesis transport via thin indirect AlAs barriers was studied by incorporating them into a vertical tunnelling hot electron transistor structure (Heiblum *et al.* 1985a) and by performing hot electron spectroscopy (Hayes *et al.* 1985) on the carriers transmitted through them. The hot electron spectroscopy technique has the advantage of probing the transport mechanisms occurring during transport through the barrier as a function of the applied bias across it. Hot electron spectroscopy techniques have been successfully applied to study several physical phenomena (see chapter 4). In all these studies direct emitter barriers were used to inject the electrons into the base region and it has been shown that about 50% of injected electrons are collected with energy close to their injection energy in the collector current for a 30nm wide base layer (Heiblum *et al.* 1985a).

1.2 Overview of the Thesis

The vertical tunnelling hot electron transistor structures used in this work were grown by MBE and consisted of n^+-GaAs contact electrodes and undoped $Al_xGa_{1-x}As$ barriers. Chapter 2 introduces the basic properties of $GaAs/Al_xGa_{1-x}As$ heterostructures with the goal of understanding transport processes through the Emitter barrier of the transistor. An outline of previous experimental observations of X-point related transport processes in indirect AlAs barriers is also presented in this Chapter.

At low temperatures the transport of electrons via thin potential barriers occurs predominantly by quantum mechanical tunnelling. The quantum mechanical tunnelling probability through a potential barrier and the associated current flow are calculated in Chapter 3.

A brief description of the hot electron transistor and the physical phenomena studied using such structures together with an introduction to the hot electron spectroscopy technique with the Tunnelling Hot Electron Transfer Amplifier (THETA) are given in Chapter 4.

The transistors were fabricated using conventional photolithography and wet etching techniques. The fabrication steps used to construct the transistors in the University of Bath Physics Department clean room are described in detail in Chapter 5. Transistor characterisation was performed at low temperatures and under various hydrostatic pressures. The measurement techniques, electronic circuits and the hydrostatic pressure measurement methods are also included in Chapter 5.

The current-voltage and transconductance-voltage characteristics of the transistor with direct emitter barriers have been modelled. Airy function transfer matrix methods were used to calculate the tunnelling probability of biased structures. Chapter 6 presents the details of calculations of the tunnelling probability and current flowing through the device structures. Calculations of in-plane voltage drop in base, band bending, the leverage factor for the collector barrier and subbands in a finite trapezoidal quantum well are also given in this chapter.

We have measured two types of transistor structure which were identical except for the composition of the emitter barrier where the AlAs mole fraction was x=0.5 in the first case and x=1 in the other. The results of measurements on these devices and an analysis of the results are presented in Chapter 7.

The final Chapter of this thesis is devoted to the conclusions drawn from this work and suggestions for future work.

Chapter 2

Basic Properties of GaAs/$Al_xGa_{1-x}As$ Heterostructures

2.1 Introduction

Gallium arsenide (GaAs) is a III-V compound semiconductor and was first synthesised by Goldsmith in 1920 (Blakemore 1982). GaAs crystals can be grown by various techniques. The Liquid-encapsulated Czochralski (LEC) technique is used to grow bulk GaAs. Epitaxial growth techniques such as Liquid Phase Epitaxy (LPE), Vapour Phase Epitaxy (VPE) and Molecular Beam Epitaxy (MBE) are widely employed to grow thin layers of GaAs (Kirkpatrick *et al.* 1985).

Materials from group III can be easily mixed with GaAs to form ternary compounds as they have very similar atomic radii to those of Ga atoms. An important example of the ternary compounds is $Al_xGa_{1-x}As$ where x is the mole fraction of AlAs. The energy gap of the $Al_xGa_{1-x}As$ alloy can be tuned by varying x from 0 to 1 – a technique known as 'Band gap engineering'. Modern growth techniques such as Molecular Beam Epitaxy (MBE) and Metal Organic Chemical Vapour Deposition (MOCVD) techniques allow one to grow layers of GaAs and $Al_xGa_{1-x}As$ alternatively to fabricate potential barriers and quantum wells along the growth direction forming single barrier, double barrier and superlattice structures.

The electronic properties of GaAs and its alloys (e.g $Al_xGa_{1-x}As$) can be altered in a controlled manner by adding substitutional impurity atoms from group III or Group IV atoms. Silicon (Beryllium) is a widely used impurity atom for n-type (p-type) doped GaAs. The impurities are introduced into the crystal by diffusion, during

epitaxy, or by ion implantation with the epitaxial technique offering the greatest degree of control over the doping profile.

A detailed overview of the properties and numerical values of important parameters are given in several review articles on GaAs, AlAs and $Al_xGa_{1-x}As$ (Adachi 1985,1993, Blakemore 1987, Madelung 1991, Pavesi and Guzzi 1994). In this chapter a brief description of the properties relevant to the work reported in this thesis will be given including a detailed account of transport via $Al_xGa_{1-x}As$ barriers and experimental observations of X-point related transport. We shall confine the discussion to transport processes taking place via heterojunctions grown in the [100] direction.

2.2 Crystal Structure

GaAs and AlAs crystallise in the zinc blende structure (Fig 2.1) with a lattice constant (a) of 5.653 Å and 5.6611Å respectively (Adachi 1985). The lattice structure consists of two interpenetrating face centered cubic (fcc) lattices of Ga and As displaced by a distance (a/4,a/4,a/4) along the body diagonal. The bonding between Ga and As atoms is a mixture of covalent (~70%) and ionic (~30%) bonding due to the partial transfer of a valance electron from Ga to As (Wight 1985).

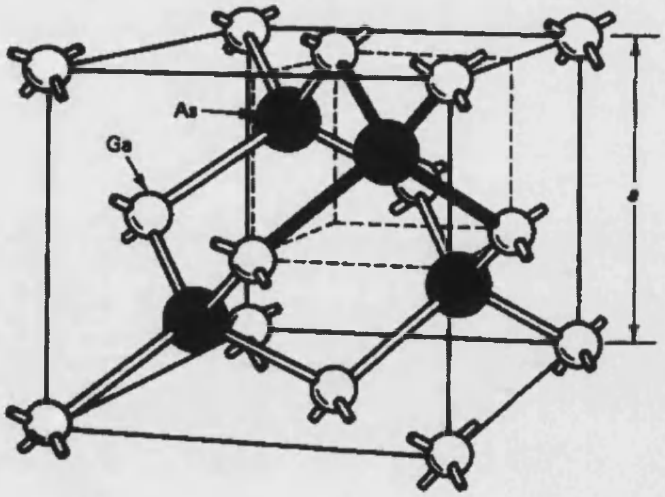

Fig.2.1 Zinc blende crystal structure of GaAs .

The lattice constant of $Al_xGa_{1-x}As$ ($a(Al_xGa_{1-x}As)$) can be estimated using the following formula (Jaros 1990).

$$a(Al_xGa_{1-x}As) = a(AlAs) + [a(GaAs) - a(AlAs)](1-x) \qquad (2.2.1)$$

where $a(AlAs)$ and $a(GaAs)$ are the lattice constants of AlAs and GaAs respectively. Substituting the values for $a(AlAs)$ and $a(GaAs)$ we get,

$$a(Al_xGa_{1-x}As) = 5.6533 + 0.0078x \qquad (2.2.2)$$

The first Brillouin zone of GaAs is an octahedron which has been truncated by (100) planes at a distance $2\pi/a$ from the zone centre (Fig 2.2). The most important high symmetry points Γ [$2\pi/a(0,0,0)$], X [$2\pi/a(0,0,1)$] and L [$2\pi/a(1/2,1/2,1/2)$] are indicated in the figure. The lines connecting the Γ-X and Γ-L points lie along the [100] and [111] directions respectively.

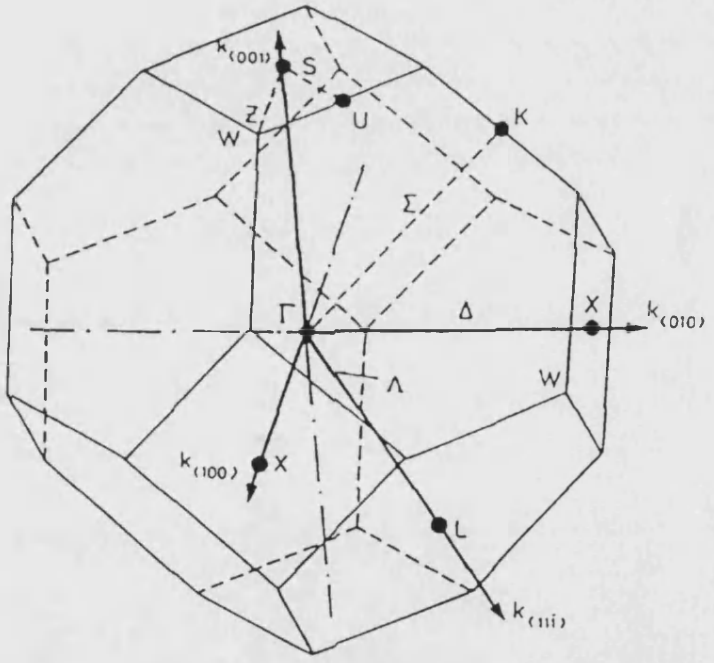

Fig 2.2 First Brillouin zone for GaAs

2.3 Band Structures

An understanding of the energy band structure of a semiconductor is of great importance in order to optimise the performance of devices. Experimentally, however, it is very difficult to obtain a complete description of the full band structure of a semiconductor, as experiments tend to give information at only a few specific points in the Brillouin zone.

Several theoretical methods have been developed to obtain the full band structure of a crystal. The most widely employed methods are the orthogonalised plane-wave method, the pseudopotential method and the **k.p** method (Sze 1981). The calculated band structure (Energy (E) versus momentum (k) relation) of GaAs and AlAs are shown in Fig. 2.3.

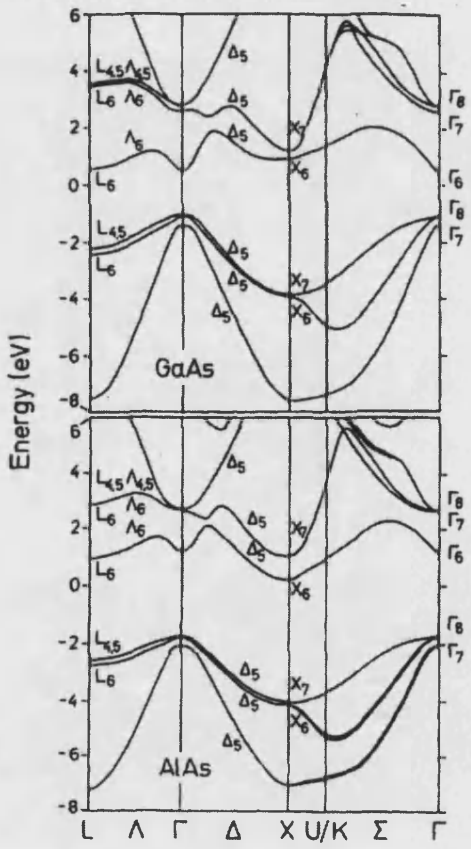

Fig. 2.3 Theoretical band structure of GaAs and AlAs (Palevesi *et al.* 1996)

For GaAs the minimum of the conduction band and the maximum of the valance band occur at the same point (Γ-point) in the Brillouin zone. Thus GaAs has a direct gap band structure. For AlAs the minimum of the conduction band is at the X-point in the Brillouin zone making it an indirect-gap semiconductor (Jaros 1990).

In the region around the conduction band edge, assuming a simple parabolic band, the E-k relationship can be approximated as (Jacobini and Lugli 1989),

$$E = \sum_{i,j} \frac{\hbar^2}{2}\left(\frac{1}{m^*}\right)_{i,j} k_i k_j \qquad (2.3.1)$$

where $\left(\frac{1}{m}\right)_{i,j} = \frac{1}{\hbar^2}\left(\frac{\partial^2 E}{\partial k_i \partial k_j}\right)_{k=0}$ is the inverse effective mass tensor and the crystal momentum k is measured from the centre of the valleys.

At the L-point and X-point the conduction band minima have an axial symmetry. Therefore the E-k relationship for the conduction band at the L-point and X-point can be approximated as,

$$E = \frac{\hbar^2}{2}\left[\frac{k_l^2}{m_l^*} + \frac{k_t^2}{m_t^*}\right] \qquad (2.3.2)$$

leading to an ellipsoidal constant energy surface (Fig. 2.4a and Fig. 2.4b) with longitudinal (m_l^*) and transverse (m_t^*) components of effective mass.

Since the conduction band minimum has cubic symmetry at the Γ-point the E-k relationship for the conduction band at the Γ-point becomes,

$$E = \frac{\hbar^2}{2m^*}k^2 \qquad (2.3.3)$$

leading to a spherical constant energy surface (Fig. 2.4c) with a single effective mass.

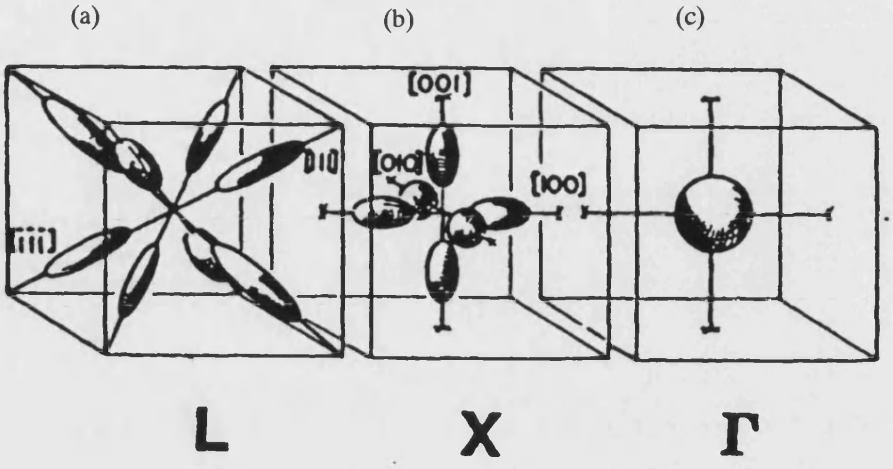

Fig. 2.4 Constant- energy surfaces characterising the conduction band structure (a) near the L-point (b) near the X-point and (c) near the Γ-point (Sze 1981).

For GaAs the conduction band effective mass at the Γ-point ($m_{\Gamma}^{*}(GaAs)$) is usually taken to be $0.067m_0$, where m_0 is the rest mass of electron (Adachi 1985, Jaros 1990). The effective masses of AlAs at X-point are not well known and a range of values have been reported for longitudinal and transverse X-point effective masses in the literature. In this work the following recently reported values were used (Table 2.1) (for see example Carbonneau *et al.* 1993, Othaman *et al.* 1993 and Teisser *et al.* 1996).

Effective mass/m_0	GaAs	AlAs
m_{Γ}^{*}	0.067	0.103
$m_{X_l}^{*}$	1.30	1.100
$m_{X_t}^{*}$	0.230	0.200

Table 2.1 Effective masses of electrons (in units of the free electron mass, m_0) in GaAs and AlAs .

2.4 Heterostructures

In the semiconductor literature a heterostructure is defined as a semiconductor structure in which the chemical composition changes with position. Heterostructures are the building blocks of most high-speed devices produced by modern growth technologies. Heterostructures are generally grown by epitaxial growth techniques such as Molecular Beam Epitaxy (MBE) and Metal Organic Chemical Vapour Deposition (MOCVD). These allow the growth of layers as thin as a single monolayer with near atomic precision control of the doping profile.

In an ideal heterojunction the identity of constituent atoms changes abruptly at the interface. High quality heterojunctions can be fabricated by bringing semiconductors having closely matched lattice constant together (Fig. 2.5). For example the very close lattice constants of GaAs and $Al_xGa_{1-x}As$ produce high quality heterojunctions. It has been demonstrated that high quality heterojuctions of two lattice mismatched materials can also be formed. The key concept lies in making one semiconductor layer sufficiently thin that the lattice mismatch can be accommodated by strain within it (Jaros 1990).

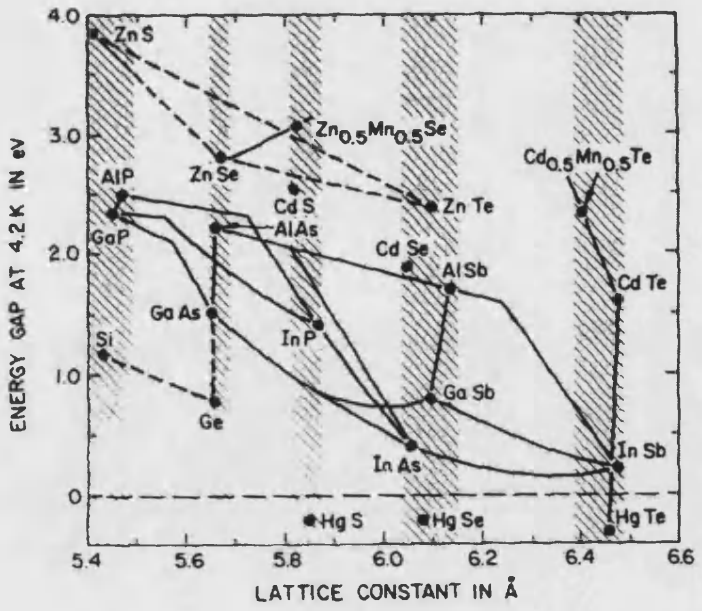

Fig. 2.5 The energy gaps of some important semiconductor crystals as a function of lattice constant at low temperature (Esaki 1987).

The band alignment of all known heterostructures can be categorised into three kinds: Type I, Type II and Type III as shown in Fig. 2.6. The band offsets of $GaAs/Al_xGa_{1-x}As$ are important parameters that determine the transport and optical properties of heterostructures. There have been several theoretical and experimental efforts to establish band offsets precisely. A brief review of this topic can be found in these references (Yu et al. 1992, Frensley 1994). On the theoretical side several models have been proposed to predict the band offsets. Anderson (1960) proposed a simple model in terms of electron affinities of semiconductors. Various other models were also proposed by several workers (Yu *et al.* 1992) yet the uncertainties in the experiments and theoretical treatments are so large as to account for the difference in the models.

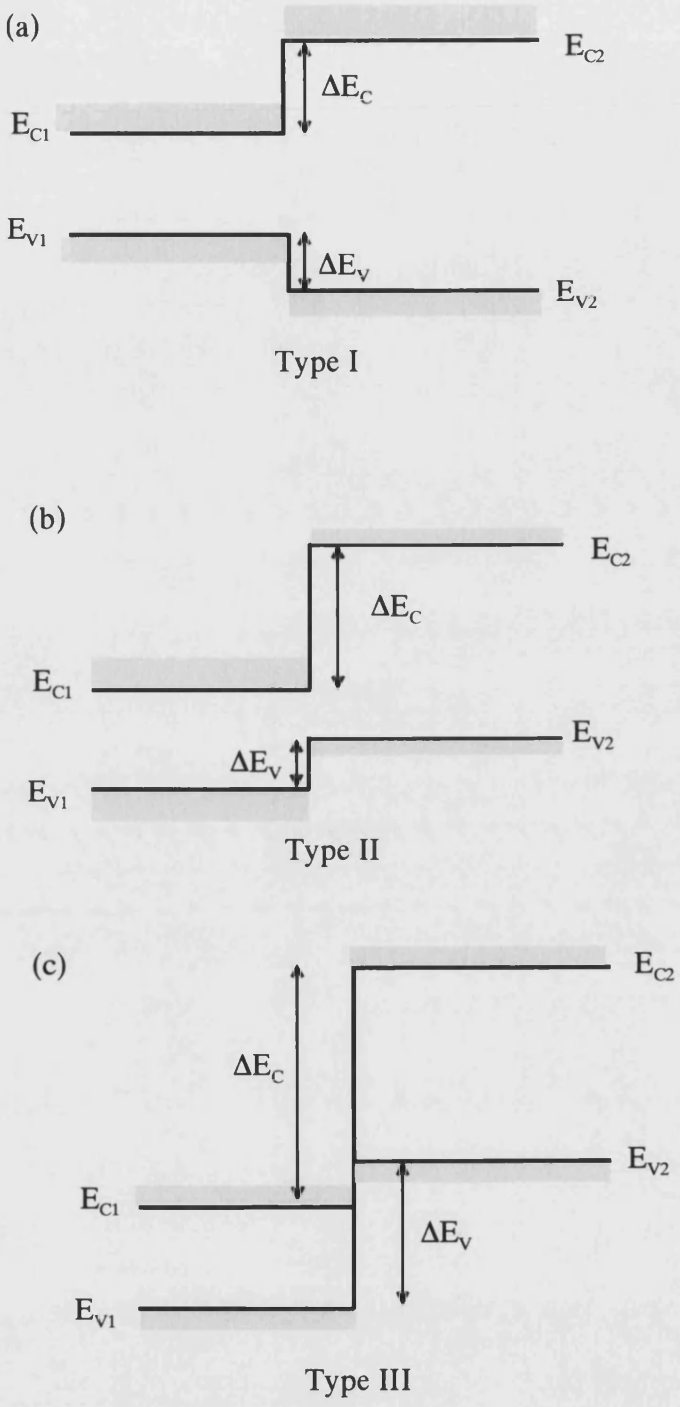

Fig. 2. 6 Band alignments of three types of heterojunctions .

In $GaAs/Al_xGa_{1-x}As$ heterojunctions the early experiments using quantum well optical absorption, current-voltage measurements, capacitance-voltage measurements and quantum well photoluminescence techniques yielded a conduction

band offset of $0.85\Delta E_g$ where ΔE_g is the difference in the fundamental energy gaps of the two materials which form the heterojunction. Later several experimental investigations revealed that the 85:15 rule is incorrect and yielded conduction band offsets of (0.55 - 0.65) ΔEg (Yu *et al.* 1992, Batey and Wright 1986).

Experimental studies showed that the conduction band offset of GaAs/$Al_xGa_{1-x}As$ heterostructures could be tuned by varying the fraction (x) of AlAs (Fig.2. 7). The energy gap of $Al_xGa_{1-x}As$ becomes indirect above x≈0.45 because the X-point minima fall below the Γ-point minimum at this composition.

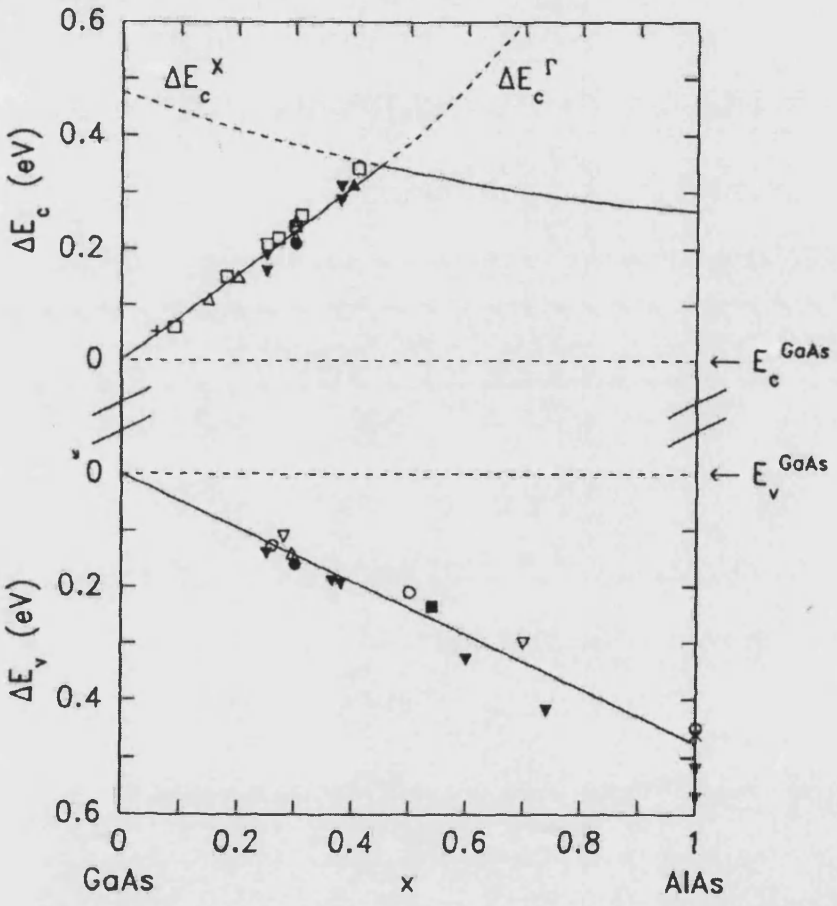

Fig 2.7 Conduction band and valence band offsets of GaAs/$Al_xGa_{1-x}As$ heterojunctions (Yu *et al.* 1992).

2. 5 Transport Through an $Al_xGa_{1-x}As$ Barrier

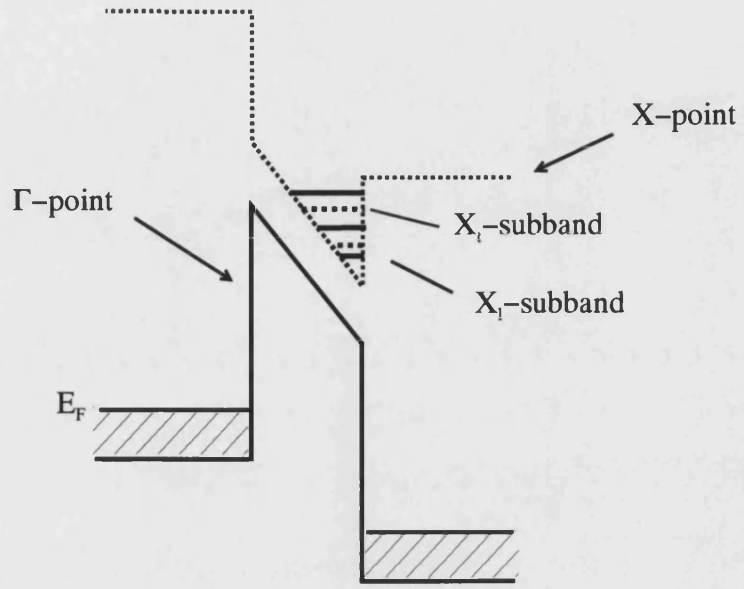

Fig. 2.8 A schematic diagram of a direct single barrier $GaAs/Al_xGa_{1-x}As/GaAs$ ($x<0.45$) structure.

When a bias voltage is applied across the direct $Al_xGa_{1-x}As$ ($x<0.45$) barrier sandwiched between n^+-GaAs (Fig. 2.8) electrons originating from the Fermi band of the GaAs emitter electrode can tunnel via the Γ-point barrier, a process we describe as Γ(GaAs)- Γ($Al_xGa_{1-x}As$)- Γ(GaAs). In this elastic transport process the momentum parallel to the interfaces is conserved.

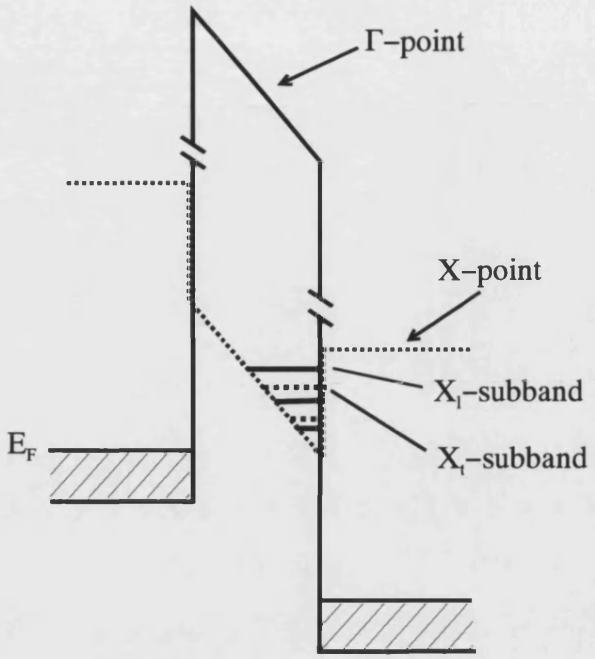

Fig. 2.9 A schematic diagram of an indirect GaAs/AlAs/GaAs single barrier structure.

In the AlAs barrier (Fig. 2.9) even though the X-point minima of the conduction band form the lowest barrier (~0.12eV Finley *et al.* 1998) to the incident electrons, elastic transport processes of the type Γ(GaAs)- Γ(AlAs)- Γ(GaAs) can always take place. However the large Γ-point barrier (~1eV) makes the current density associated with this process rather small; particularly for thick barriers. For thin barriers (<4nm) Γ-point related transport may however contribute significantly. Due to the broken translational symmetry of the lattice in the tunnelling direction [100], there exists a mixing between Γ-states in the GaAs electrode and longitudinal X-states (X_l) in the barrier allowing the elastic transfer of Γ–electrons via this high effective mass (~$1.1m_0$) X-point channel. The conservation of parallel momentum in the Γ(GaAs)- X_l(AlAs)- Γ(GaAs) process can be easily understood with the aid of the constant energy surfaces of GaAs and AlAs (Carnahan 1994) . For transport in the [100] direction the fact that the parallel momentum is less than the Fermi wavevector (Fig. 2.10) allows Γ(GaAs)- X_l(AlAs)- Γ(GaAs) transport to take place elastically.

The transverse X-minima have relatively low effective masses (~$0.2m_0$) in the direction perpendicular to [100] direction and may contribute considerably to current flow. Since the parallel momentum is very much greater than the Fermi wavevector (Fig. 2.10) transport via X_t requires an additional momentum scattering event in order to conserve the momentum. This can take place via the emission or absorption of zone boundary phonons or by interface roughness or random alloy scattering. It has been assumed in many works that the low scattering probability for electrons to transfer into the X_t minima makes this transport process unimportant.

Transport via L-point minima lying in the [111] directions is unimportant for device structures grown in the [100] direction as the tunnelling electrons must undergo very strong scattering to access these L-point minima. For device structures grown in the [111] direction transport via the L-point can however take place as an elastic processes.

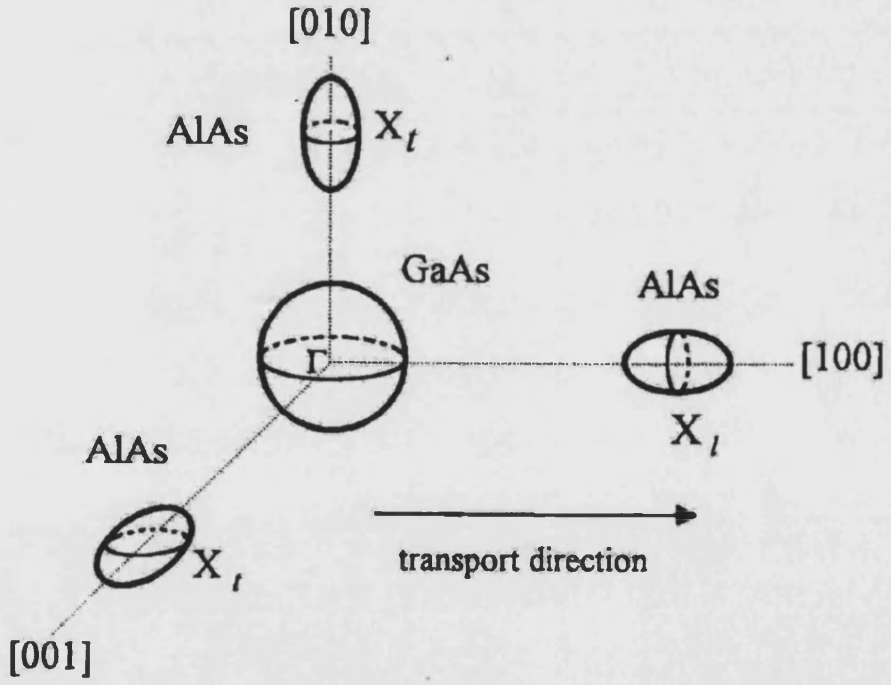

Fig. 2.10 Constant energy surfaces for GaAs and AlAs in k-space.

2.6 The Effect of Hydrostatic Pressure

The application of hydrostatic pressure isotropically compresses the lattice of a semiconductor causing changes in the energy gap and effective masses (Robert *et al.* 1984).

Since changes in valence band offsets with applied pressure are negligible for thin layers, hydrostatic pressure applied to semiconductor heterostructures may be used to induce changes in conduction band offsets (Fig. 2.11) and effective masses without altering extrinsic parameters such as doping profile and interface quality.

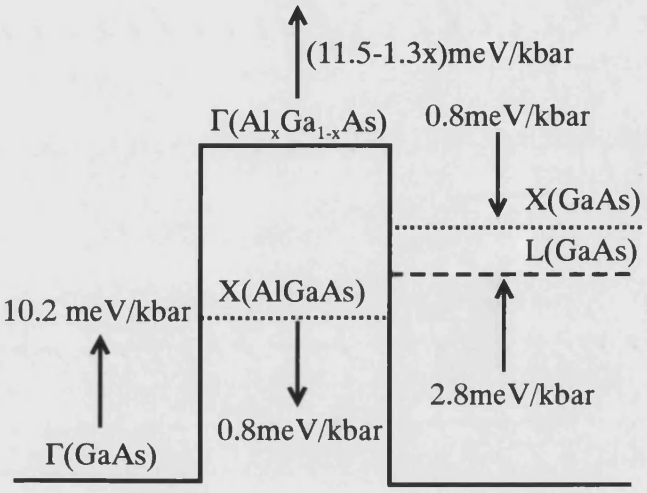

Fig. 2.11 Pressure induced changes of Γ, X and L points conduction band edges of the GaAs and $Al_xGa_{1-x}As$.

We see from the above figure that hydrostatic pressure applied to GaAs/AlAs heterostructures reduces the X(AlAs)–Γ(GaAs) conduction band discontinuity at a rate of –11meV/kbar (Mendez *et al.* 1986) without changing the Γ(AlAs)- Γ(GaAs) offset.

The pressure induced increase in the effective mass of the electrons is most pronounced around the Γ-point minimum of the conduction band and around the X-point minima the change is negligibly small (Adams and Dunstan 1990).

2.7 Observations of X-point Related Transport in Single Barriers

In previous reports on tunnelling via AlAs barriers, it has often been assumed that electron always tunnel through the Γ-point barrier despite the fact that the X-point barrier displays the lowest barrier height for the incoming carriers (Osburn 1980, Hase *et al.* 1984). It was Mendez and co-workers (1986) who first experimentally observed evidence for the influence of the X-point on transport through Double Barrier Resonant Tunnelling Diodes (DBRTD). It was shown that the X-point quasi-bound states in the AlGaAs quantum well influence the current flowing through the DBRTD.

X-point related tunnelling processes were observed by Hase *et al.* (1986) and by Bonnefoi *et al.* (1986) in GaAs/AlGaAs/GaAs single barriers. They argued that the Γ-point barrier is insufficient to account for the shape of the experimental current-voltage characteristics of the structures. From I-V measurements on a series of single barrier diodes of different barrier width Landheer *et al.* (1989) concluded that the Γ-point process remains the major current carrying mechanism for AlAs barriers of width up to about 3nm. For AlAs barriers of width above 4nm X-point related processes were shown to be dominant. Rossmanith *et al.* (1991, 1993) provided further evidence for the influence of X-point barriers from thermionic emission measurements on single barrier AlAs structures under various hydrostatic pressures.

Beresford *et al.* (1989) observed a clear negative differential resistance in the current-voltage characteristic of a single AlAs barrier structure giving evidence for the existence of subbands in an AlAs quantum well formed by the X-point conduction band minima. Carbonneau *et al.* (1993) and Othamann *et al.* (1993) also reported clear evidence for an X-point related resonance in AlAs single barrier diodes which shifted towards lower voltages under hydrostatic pressure.

In all the works described above the transport processes and the resonances observed were related to longitudinal X-point barriers and to the longitudinal X-point subbands. Evidence for transfer via transverse X-point subbands has been observed by Finley *et al.* (1996, 1998) in addition to the momentum conserving transfer via X_l

subbands. The phonons required to conserve momentum during X_t transport have also been observed in their studies.

Electroluminescence spectroscopic techniques (Petrov *et al.* 1996, Finley *et al.* 1998) have been shown to be an excellent tool for probing transport mechanisms occurring in the barrier and the elecrode region. Finley *et al.* (1998) observed transfer of carriers into excited X-point subbands and subsequent relaxation within the AlAs barrier down through the ladder of X-point subbands using electroluminescence. They demonstrated that intervalley scattering plays a major role in transport processes occurring in AlAs barriers. The scattered carriers are then emitted into the transport region from the X_l subbands of the AlAs quantum well.

Chapter 3

Quantum Theory of Electron Transport

3.1 Introduction

Electronic transport across potential barriers can take place via three different mechanisms as illustrated in Fig. 3.1. The relative importance of these mechanisms depends on the nature of the barrier, applied bias across the barrier and the temperature.

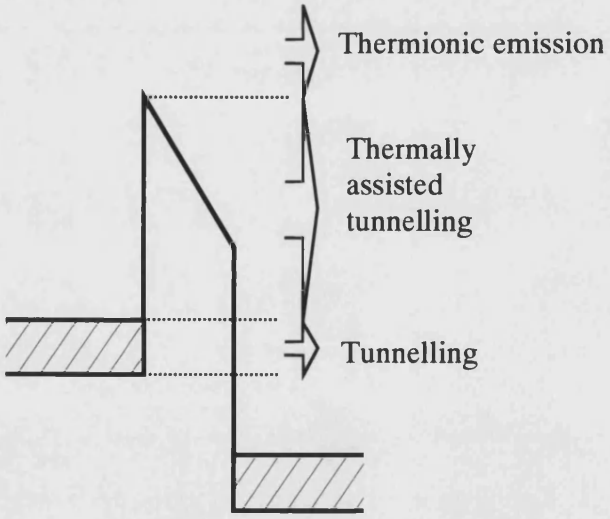

Fig. 3.1 Schematic representation of various transport mechanisms through the barrier.

When the barrier is made thin enough the electrons tunnel through the classically forbidden region at zero temperature. At finite temperature electrons

acquire some thermal energy and tunnel through the barrier, a phenomenon called thermally assisted tunnelling. If the thermal energy acquired by the electrons is comparable to the barrier height they pass the barrier via thermionic emission.

Historically the concept of tunnelling is almost as old as quantum mechanics itself. There have been several observation such as the ionisation of hydrogen by an electric field by Oppenheimer (1928) and the emission of alpha particles by Gamow (1928) for which a tunnelling model was used to explain the experimental results. The idea of tunnelling in solids was first used by Fowler and Nordheim (1928) to explain field emission in metals which was observed by Lillenfield (1922). The most conclusive experimental evidence for quantum mechanical tunnelling in solids was, however, found by Esaki (1957) after his invention of the tunnel diode. Giaever (1960) discovered quasiparticle tunnelling between Superconductors. Based on Giaever's work Josephson (1962) predicted and subsequently observed the phase coherence between two superconductors separated by a thin tunnel barrier (i.e the Josephson effect).

In the following sections detailed accounts of the derivation of the tunnelling current, transmission coefficient and themionic emission current are given.

3.2 Tunnelling Current

The current flowing through a barrier can be calculated fairly easily using the Fermi Golden rule for transition rates between two quantum states. Fig.3.2 shows a tunnel barrier (e.g. $Al_xGa_{1-x}As$) sandwiched between two metallic electrodes (e.g. n^+- GaAs). In the absence of any applied bias, no net current flows through the barrier. When a voltage V is applied, the occupied states on the one side of the barrier will coincide with the empty states on the other side causing a net current to flow. We calculate the tunnelling current through the barrier using an approach similar to the one given by Duke (1969) in his review of the Theory of Metal-Insulator-Metal tunnelling.

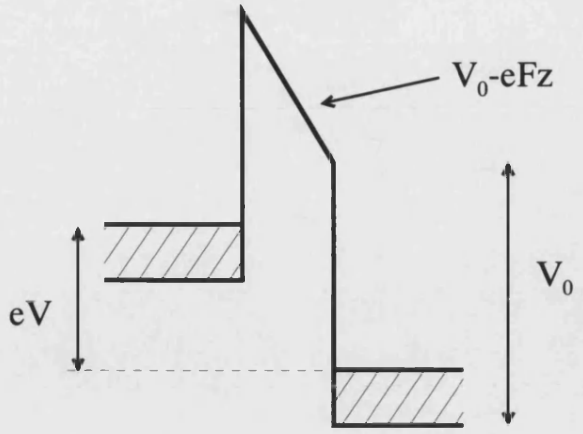

Fig.3.2 Schematic illustration of a potential barrier.

Using the Fermi's golden rule one can easily show that the current flow from the left to right of the barrier is given by,

$$J_{LR} = (-e)\int 2.\frac{d^3k_L}{(2\pi)^3} v_{zL} f_L(E_L)[1 - f_R(E_R)]D_{LR}(E_R,V) \qquad (3.2.1)$$

where e is the magnitude of the electronic charge, $f_L(E_L)$ and $f_R(E_R)$ are the Fermi-Dirac distribution functions in the left and right electrodes respectively, v_{zL} is the velocity towards the barrier in the left hand electrode, $D_{LR}(E_R,V)$ is the transmissivity of the barrier for electrons incident from the left hand electrode, and V is the applied bias.

Similarly the current flowing from right to left is given by,

$$J_{RL} = (-e)\int 2.\frac{d^3k_R}{(2\pi)^3} v_{zR}[1 - f_R(E_R)]f_L(E_L + eV)D_{RL}(E,V) \qquad (3.2.2)$$

The net current flowing through the barrier is then

$$J = J_{LR} - J_{RL} \qquad (3.2.3)$$

To subtract the two currents we need to be able to relate $D_{LR}(E,V)$ to $D_{RL}(E,V)$ and $v_{zL}d^3k_L$ to $v_{zR}d^3k_R$. These can be related by making the effective mass approximation in the electrodes and assuming that the exact potential of the barrier is approximated by taking the local average of the microscopic potential.

In addition we have the following momentum and energy conservation laws:

1. For perfect infinite plane junctions the transverse (or parallel) component of k is conserved.

$$k_{tL} = k_{tR} = K_{tbarrier} \tag{3.2.4}$$

2. In the absence of inelastic processes the total energy of the tunnelling electrons is conserved. If we measure the energy relative to the conduction band edge of the left electrode then

$$E_L = E_R - eV + E_{FL} - E_{FR} = E \tag{3.2.5}$$

One can show that D_{LR} equals D_{RL} by solving the Schrödinger equation for this tunnelling problem and that D only depends on the longitudinal (or z) component of energy for a perfect parabolic band.

Using the effective mass model the total energy of an electron in the electrodes is expressed as

$$E_i = \frac{\hbar^2}{2m^*}\left\{\left(k_{xi}^2 + k_{yi}^2\right) + k_{zi}^2\right\} \tag{3.2.6}$$

$$= E_{ti} + E_{zi} \tag{3.2.7}$$

This assumes an isotropic effective mass m^* in the electrodes.

The velocity of the tunnelling election is given by the simple relation

$$v_{zi} = \frac{1}{\hbar}\frac{\partial E(k_i)}{\partial k_{zi}}; \quad i = (L,R) \tag{3.2.8}$$

Making use of the conservation laws and the effective mass approximation, we can show that

$$d^2k_{tL} = d^2k_{tR} = d^2k_t \tag{3.2.9}$$

$$dE_L = dE_R \tag{3.2.10}$$

$$v_{zi}dk_{zi} = \frac{1}{\hbar}dE_i; \quad i{:}L,R \tag{3.2.11}$$

Using the energy conservation law the subscript in the Fermi-Dirac functions of the left and right electrodes can be dropped and they can be related as follows.

$$f_R(E_R) = f_L(E_L + eV) = f(E + eV) \tag{3.2.12}$$

Using the above relationships we can now combine J_{LR} and J_{RL} to get the net current flow

$$J = \frac{2e}{(2\pi)^3 \hbar} \int dE[f(E) - f(E + eV)] d^2k_t D(E_z, V) \tag{3.2.13}$$

Since D depends only on E_z we convert the integration dk_t into one over dE_t by using the following identity

$$d^2k_t = \frac{2\pi m^*}{\hbar^2} dE_t \tag{3.2.14}$$

Using this conversion the net current density becomes

$$J = \int dE_z N(E_z) D(E_z, V) \tag{3.2.15}$$

$$\text{where } N(E_z) = \int [f(E) - f(E + eV)] dE_t \tag{3.2.16}$$

is called the electron supply function which can be evaluated as

$$N(E_z) = \frac{m^* e k_B T}{2\pi^2 \hbar^3} \ln \left\{ \frac{1 + \exp[(E_F - E_z)/k_B T]}{1 + \exp[(E_F - E_z - eV)/k_B T]} \right\} \tag{3.2.17}$$

where k_B is the Boltzmann constant and T is the absolute temperature.

3.3 Quantum Mechanical Tunnelling Theory

The starting point of the quantum description of the theory of matter is probably the hypothesis proposed by de Broglie in 1923 that particles may also have wavelike characteristic although the quantum nature of electromagnetic radiation was already proposed by Max Planck in 1900. On the basis of de Broglie's hypothesis Schrödinger in 1926 developed the theoretical foundation of quantum mechanics that

resulted in a most important mathematical equation known as the Schrödinger equation. Another approach called Matrix mechanics was also developed in the same period by Heisenberg.

The nature of the solutions of the Schrödinger equation, the wave functions, implies that they can penetrate classically forbidden regions e.g. a barrier whose potential energy is higher than the kinetic energy of the incident wave/particle. The tunnelling probability for a particle incident on a barrier can be calculated by solving the Schrödinger equation in different potential regions and imposing the appropriate boundary conditions at the interfaces. For simple cases such as a single barrier under flat band conditions, the exact solution of the Schrödinger equation can be easily found. For more general barriers the Schrödinger equation is normally solved by approximate analytical methods. For example the tunnelling probability through a single barrier under bias may be solved using an approximation scheme developed by Wentzel, Kramers and Brillouin (Bohm 1986) provided the barrier potential varies slowly in space. In device structures where the potential varies linearly across the barrier, the Schrödinger equation in the barrier region can be solved exactly using an Airy function approach (Kelly 1984).

In the rest of this section a description of the Airy function transfer matrix method (Brennen and Summers 1987; Allen and Richardson 1996) to find the transmission probability through a tilted potential barrier will be given.

We start by considering a potential barrier under bias sandwiched between two conducting regions (Fig. 3.3). We assume that there is no voltage drop in the cladding layer, i.e. band bending at the interfaces is ignored.

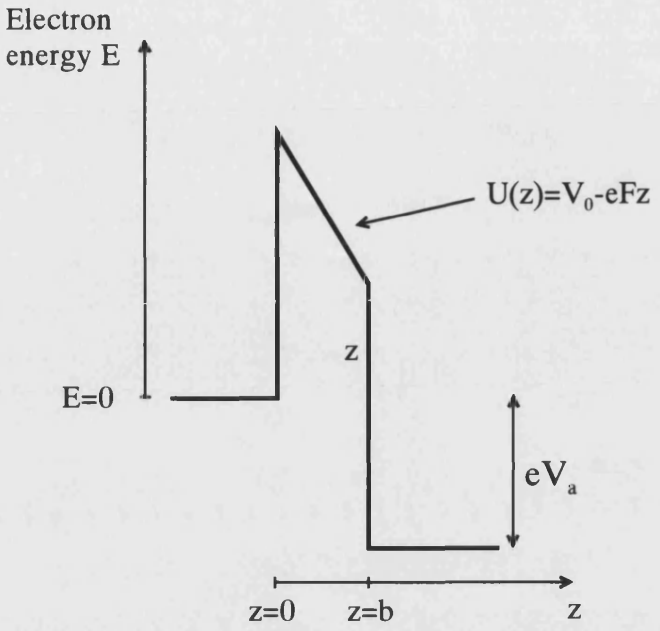

Fig. 3.3 Schematic illustration of a single barrier potential of barrier height V_0 and width b under bias V_a.

The one-dimensional potential in the three regions is given by

$$U(z) = 0 \qquad z < 0 \tag{3.3.1}$$

$$= V_0 - eFz \qquad 0 \le z \le b \tag{3.3.2}$$

$$= -eV_a \qquad z \ge b \tag{3.3.3}$$

where $F = \frac{V_a}{b}$ is the electric field in the barrier.

The time independent three-dimensional Schrödinger equation for a general potential can be written as

$$-\frac{\hbar^2}{2m^*}\nabla^2\Psi(x,y,z) + U(x,y,z)\Psi(x,y,z) = E\Psi(x,y,z) \tag{3.3.4}$$

For a one-dimensional potential energy the three-dimensional Schrödinger equation can be separated into transverse (referred to as the x, y plane) and longitudinal part (referred to as the z-axis) using the effective mass approximation.

$$-\frac{\hbar^2}{2m^*}\frac{d^2\psi(\vec{r})}{dr^2} = E_t\psi(\vec{r}) \qquad (3.3.5)$$

and

$$-\frac{\hbar^2}{2m^*}\frac{d^2\psi(z)}{dz^2} + U(z)\psi(z) = E_l\psi(z) \qquad (3.3.6)$$

where $\vec{r}$ in equation (3.3.5) represents a vector in the x-y plane, and $E_t(E_l)$ is the energy associated with the transverse (longitudinal) motion.

The total wave function $\Psi(x,y,z) = \psi(\vec{r}).\psi(z)$ (3.3.7)

$$= C\psi(z)e^{i\vec{k}.\vec{r}} \qquad (3.3.8)$$

$$= C\psi(z)e^{ik_x x}e^{ik_y y} \qquad (3.3.9)$$

where C is an arbitrary constant.

The total energy $E = E_t + E_l$ (3.3.10)

where the transverse energy can be written in terms of a transverse momentum k_t as

$$E_t = \frac{\hbar^2 k_t^2}{2m^*} \qquad (3.3.11)$$

$$= \frac{\hbar^2}{2m^*}\left(k_x^2 + k_y^2\right) \qquad (3.3.12)$$

The solutions of the one-dimensional Schrödinger equation in the regions $z < 0$ and $z \geq b$ are given by

$$\psi_1(z) = e^{ik_1 z} + \mathrm{Re}^{-ik_1 z} \quad z < 0 \qquad (3.3.13)$$

$$\psi_3(z) = Te^{ik_2 z} \qquad z \geq b \qquad (3.3.14)$$

where $k_1 = \sqrt{\frac{2m_1^* E_l}{\hbar^2}}$, (3.3.15)

$$k_2 = \sqrt{\frac{2m_1^*(E_l + eV_a)}{\hbar^2}}, \qquad (3.3.16)$$

R is the amplitude of the reflected wave assuming unity amplitude for the incoming wave, T is the amplitude of the transmitted wave and m_1^* is the effective mass in the region $z < 0$ and $z \geq b$.

In the region $0 \leq z \leq b$ the one-dimensional Schrödinger equation becomes

$$\frac{d^2\psi(\rho)}{d\rho^2} - \rho\psi(\rho) = 0 \qquad (3.3.17)$$

where $\rho = \left(\frac{2m_2^* eF}{\hbar^2}\right)^{1/3} \left\{\frac{V_0 - E_l}{eF} - z\right\}$ (3.3.18)

and m_2^* is the effective mass in the region $0 \leq z \leq b$.

The solution can be written in terms of Airy functions Ai and Bi as

$$\psi_2(\rho) = C_1 Ai(\rho) + C_2 Bi(\rho) \qquad (3.3.19)$$

where C_1 and C_2 are arbitrary constants.

By using the boundary conditions that ψ and $\frac{1}{m^*}\frac{d\psi}{dz}$ are continuous at $z = 0$ and $z = b$ we obtain the following equations.

$$1 + R = C_1 Ai(z = 0) + C_2 Bi(z = 0) \qquad (3.3.20)$$

$$i\frac{k_1}{m_1^*}(1 - R) = \frac{1}{m_2^*}\lambda_1\left[C_1 Ai'(z = 0) + C_2 Bi'(z = 0)\right] \qquad (3.3.21)$$

$$Te^{ik_2 b} = C_1 Ai(z = b) + C_2 Bi(z = b) \qquad (3.3.22)$$

$$\frac{ik_2}{m_1^*}e^{ik_2 b}T = \frac{1}{m_2^*}\lambda_2\left[C_1 Ai'(z = b) + C_2 Bi'(z = b)\right] \qquad (3.3.23)$$

where $\lambda_1 = \left(\frac{2m_1^* eF}{\hbar^2}\right)^{1/3}$ (3.3.24)

and $\lambda_2 = \left(\frac{2m_2^* eF}{\hbar^2}\right)^{1/3}$. (3.3.25)

which in matrix form becomes

$$\begin{pmatrix}1\\R\end{pmatrix}=\frac{1}{2ik_1}\begin{pmatrix}ik_1 & 1\\ ik_1 & -1\end{pmatrix}\begin{pmatrix} Ai(z=0) & Bi(z=0)\\ \lambda_1\frac{m_1^*}{m_2^*}Ai'(z=0) & \lambda_1\frac{m_1^*}{m_2^*}Bi'(z=0)\end{pmatrix}\times$$

$$\begin{pmatrix} Ai(z=b) & Bi(z=b)\\ \lambda_2\frac{m_1^*}{m_2^*}Ai'(z=b) & \lambda_2\frac{m_1^*}{m_2^*}Bi'(z=b)\end{pmatrix}^{-1}\begin{pmatrix} e^{ik_2b} & 0\\ ik_2e^{ik_2b} & 0\end{pmatrix}\begin{pmatrix}T\\0\end{pmatrix}$$

(3.3.26)

$$=M_{total}\begin{pmatrix}T\\0\end{pmatrix} \tag{3.3.27}$$

where

$$M_{total}=\frac{1}{2ik_1}\begin{pmatrix}ik_1 & 1\\ ik_1 & -1\end{pmatrix}\begin{pmatrix} Ai(z=0) & Bi(z=0)\\ \lambda_1\frac{m_1^*}{m_2^*}Ai'(z=0) & \lambda_1\frac{m_1^*}{m_2^*}Bi'(z=0)\end{pmatrix}\times$$

$$\begin{pmatrix} Ai(z=b) & Bi(z=b)\\ \lambda_2\frac{m_1^*}{m_2^*}Ai'(z=b) & \lambda_2\frac{m_1^*}{m_2^*}Bi'(z=b)\end{pmatrix}^{-1}\begin{pmatrix} e^{ik_2b} & 0\\ ik_2e^{ik_2b} & 0\end{pmatrix} \tag{3.3.28}$$

The matrix M_{total} can be expressed in a convenient way as,

$$M_{total}=\frac{1}{2ik_1}\begin{pmatrix}ik_1 & 1\\ ik_1 & -1\end{pmatrix}S(z=0)S^{-1}(z=a)\begin{pmatrix} e^{ik_2b} & 0\\ ik_2e^{ik_2b} & 0\end{pmatrix} \tag{3.3.30}$$

where

$$S(z=0)=\begin{pmatrix} Ai(z=0) & Bi(z=0)\\ \lambda_1\frac{m_1^*}{m_2^*}Ai'(z=0) & \lambda_1\frac{m_1^*}{m_2^*}Bi'(z=0)\end{pmatrix}\text{ and} \tag{3.3.31}$$

$$S(z=b)=\begin{pmatrix} Ai(z=b) & Bi(z=b)\\ \lambda_2\frac{m_1^*}{m_2^*}Ai'(z=b) & \lambda_2\frac{m_1^*}{m_2^*}Bi'(z=b)\end{pmatrix} \tag{3.3.32}$$

are the interface matrices at $z=0$ and $z=b$ respectively.

The transmission coefficient defined as the ratio of transmitted flux to incident flux can be easily shown to be

$$D = \frac{k_3}{k_1} T^* T \tag{3.3.33}$$

From equation (3.3.27) T can be expressed as

$$T = \frac{1}{\left| M_{total}^{11} \right|^2} \tag{3.3.34}$$

where M_{total}^{11} is one of the elements of the matrix M_{total} and can be shown to be,

$$M_{total}^{11} = \left(u_{11} + \frac{k_1}{k_2} u_{22} \right) + i \left(\frac{1}{k_2} u_{21} - k_1 u_{12} \right) \tag{3.3.35}$$

where the u_{ij}'s are elements of the matrix $U = S(z=0) \times S^{-1}(z=b)$.

Hence the final expression for transmission coefficient becomes

$$D = \frac{4k_2/k_1}{\left(u_{11} + \frac{k_1}{k_2} u_{22} \right)^2 + \left(\frac{1}{k_2} u_{21} - k_1 u_{12} \right)^2} \tag{3.3.36}$$

3.4 Thermionic Emission Theory

The formula for the thermally activated current flowing through the barrier can be derived by substituting the classical values for the transmission coefficient into the equation (3.2.18).

$$J = \int_0 dE_z N(E_z) D(E_z, V) dE_t \tag{3.4.1}$$

Substituting classical values

$$D(E_z, V) = 1 \text{ for } E_z > V_0 \tag{3.4.2}$$

$$D(E_z, V) = 0 \text{ for } E_z < V_0 \tag{3.4.3}$$

the 3D Richardson law can be obtained.

$$J = A^* T^2 \exp\left(-\frac{V_0 - E_F}{k_B T}\right) \tag{3.4.4}$$

where $A^* = \frac{em^* k_B^2}{2\pi^2 \hbar^3}$ (3.4.5)

and is called the Richardson constant.

Chapter 4

Hot Electron Spectroscopy; Experimental Method

4.1 Introduction

There are many semiconductor devices in which non-equilibrium electron transport plays a major role in their characteristics. The Gunn diode (Gunn 1963) is one of the best-known devices that uses nonequilibrium electrons for its operation. A non-equilibrium ensemble of electrons can be generated by several different methods with kinetic energy in excess of the Fermi energy of the equilibrium electrons, thus, the name "Hot Electrons". In bulk semiconductors the energy can be transferred to the electrons by applying electric or electromagnetic fields. Other techniques include the use of a band discontinuity in a heterojunction, thermionic emission over a potential barrier, and quantum mechanical tunnelling via a thin potential barrier (Fig. 4.1).

In the following sections detailed descriptions of hot electron transistors and their operation principles are presented.

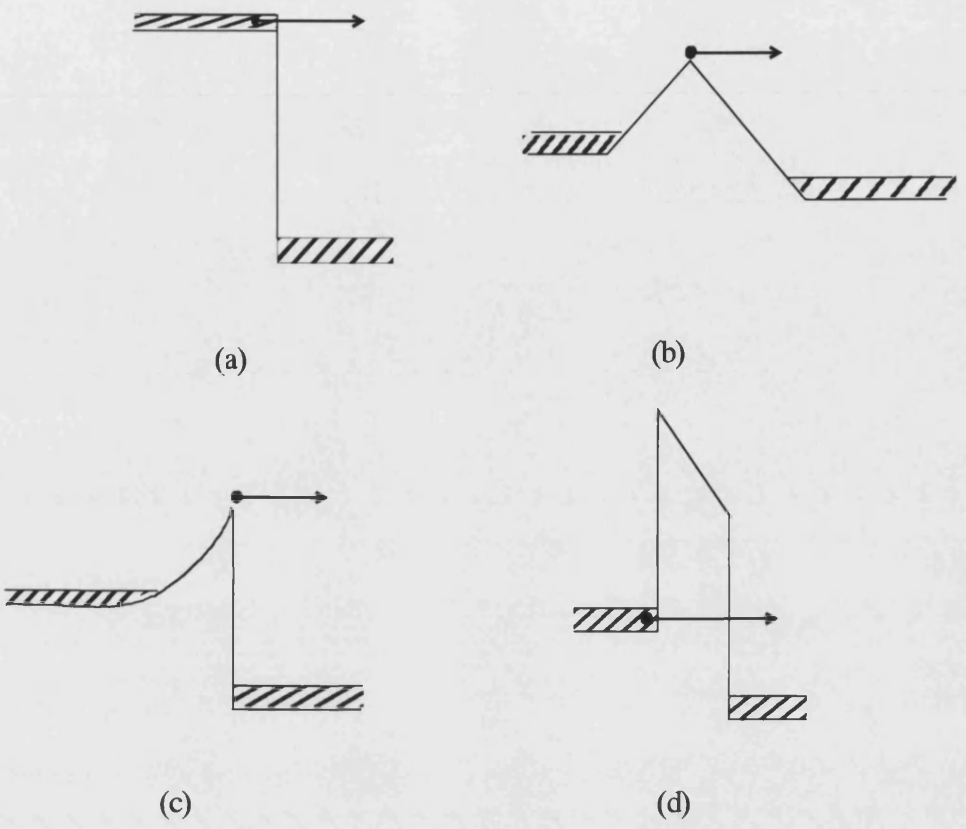

Fig. 4.1 An illustration of the generation of hot electrons (a) by the band discontunity within a heterojunction (b) thermionic emission over a triangular barrier (c) thermionic emission over a Schottky barrier and (d) tunnelling through a potential barrier.

4.2 Hot Electron Transistors

The hot electron transistor is a three-terminal device that relies on hot electrons for its operation. Many studies have been made of vertical hot electron transistors in which electron transport takes place perpendicular to the hetero-interface. Lateral hot electron transistors (Palevki *et al.* 1989a, 1989b) have also been fabricated in a 2DEG in order to study lateral tunnelling and ballistic transport. Since the structure we studied is a vertical hot electron transistor, we shall not attempt to describe lateral hot electron transistor structures in this chapter.

Since the principles of operation and the structure of hot electron transistors (which will be described later in this chapter) resemble bipolar transistors, standard transistor notations are usually used to describe the terminals and characteristics of hot electron transistors.

4.2.1 A Brief History

Mead (1960) proposed the first hot electron transistor structure consisting of two oxide layers sandwiched between metal layers resulting in a Metal-Oxide-Metal-Oxide-Metal (MOMOM) structure (Fig. 4.2 a). The first oxide layer was made thin enough to allow electrons to tunnel through it when an external bias is applied across it and the second one is thick to prevent tunnelling of carriers. The gain of this transistor was found to be very low owing to the difficulties associated with fabricating a pin-hole free thin base layer to realise ballistic electron transport as well as the quantum mechanical reflection of carriers at the base-collector barrier interface.

Spratt *et al.* (1961) attempted to obtain higher gain by making the collector barrier smaller. They replaced the collector oxide barrier by a metal-semiconductor Schottky barrier (Fig.4.2 b) and reported a high gain for this MOMS structure. Later it was proved that the experimentally observed high gain was due to pinholes in the base region. Kisaki (1973) made a modification to Mead's MOMOM structure by using a p-type silicon (Si) base and an n-type Si collector resulting in a MOpn structure (Fig. 4.2 c). Another variation of this structure was realised by replacing the emitter barrier of the MOMS structure with a metal-semiconductor Schottky barrier resulting in a SMS structure or a metal base transistor (Fig. 4.2 d) (Atalla and Kahng 1962; Geppert 1962).

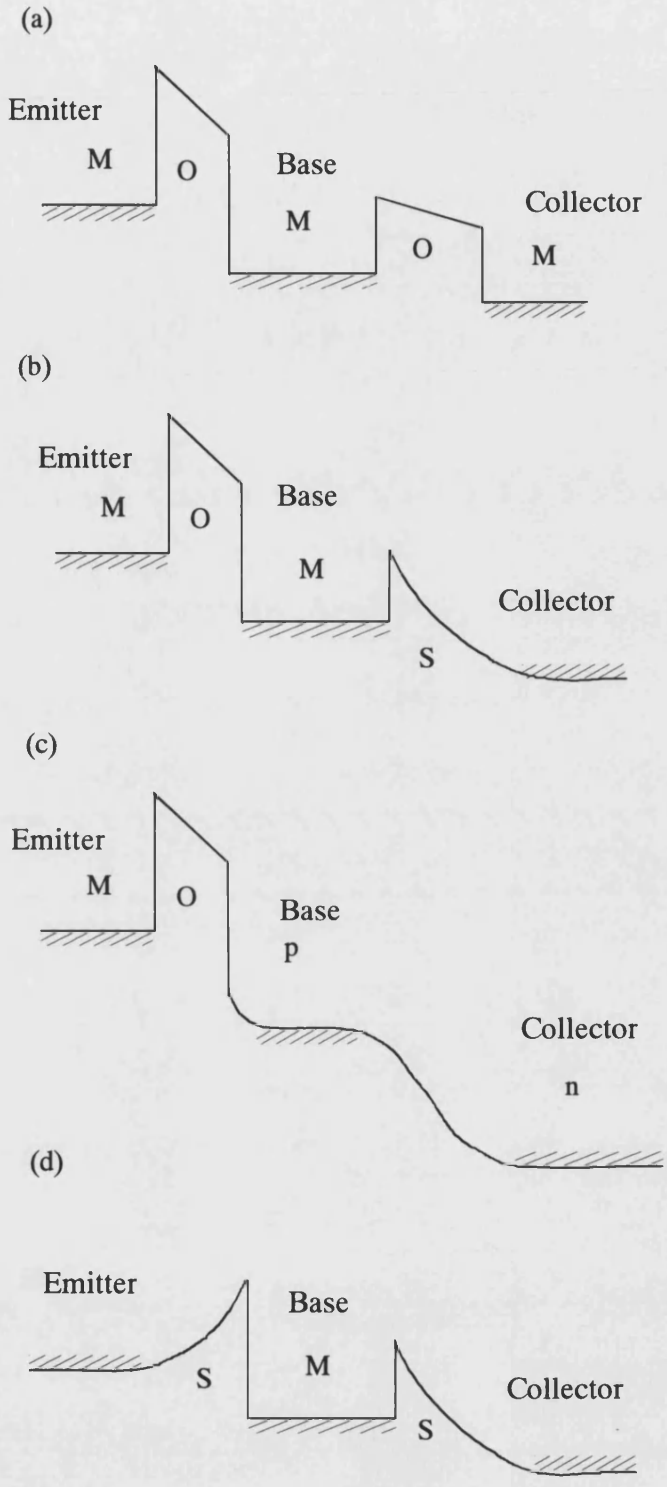

Fig 4.2 Schematic diagram of the structure of (a) Mead's MOMOM (b) the MOMS (c) the MOpn and (d) the SMS (or metal base transistor).

All these different schemes ended up with the same problem of low current gain. A decade later a renewal of interest in the hot electron transistor was due to Shannon (1979) who fabricated a hot electron transistor in Si where the emitter barrier was formed by a Schottky contact to the Si and the collector barrier was fabricated by implanting p-type dopant into the n-type Si (Fig. 4.3 a). Shannon's proposal and advances in molecular beam epitaxial (MBE) growth techniques allowed Hollis *et al.* (1983) to create triangular shaped potential barriers in GaAs by introducing a thin p-type dopant layer in the structure resulting in the Planar Doped Barrier Transistor (PDBT) (Fig. 4.3 b). Hayes *et al.* (1984) utilised the PDBT to perform an energetic analysis of the electrons injected over the emitter barrier. Long *et al.* (1986) made a modification to the PDBT by replacing the emitter barrier with a linearly graded AlGaAs barrier (Fig. 4.3 c).

The subject of the hot electron transistor was thoroughly reviewed by Heiblum (1981) together with a proposal for a new type of hot electron transistor called the Tunnelling Hot Electron Transfer Amplifier (THETA). The THETA device is essentially the semiconductor analogue of Mead's MOMOM structure where n^+-GaAs replaces the metal electrodes and undoped $Al_xGa_{1-x}As$ replaces the oxide layers (Fig. 4.3 d). The first THETA device employing GaAs-AlGaAs heterostructures was fabricated by Yokoyama *et al.* (1984) followed by Heiblum *et al.* (1985a) and Hase *et al.* (1985). A review of the development of the THETA is given by Heiblum and Fischetti (1990).

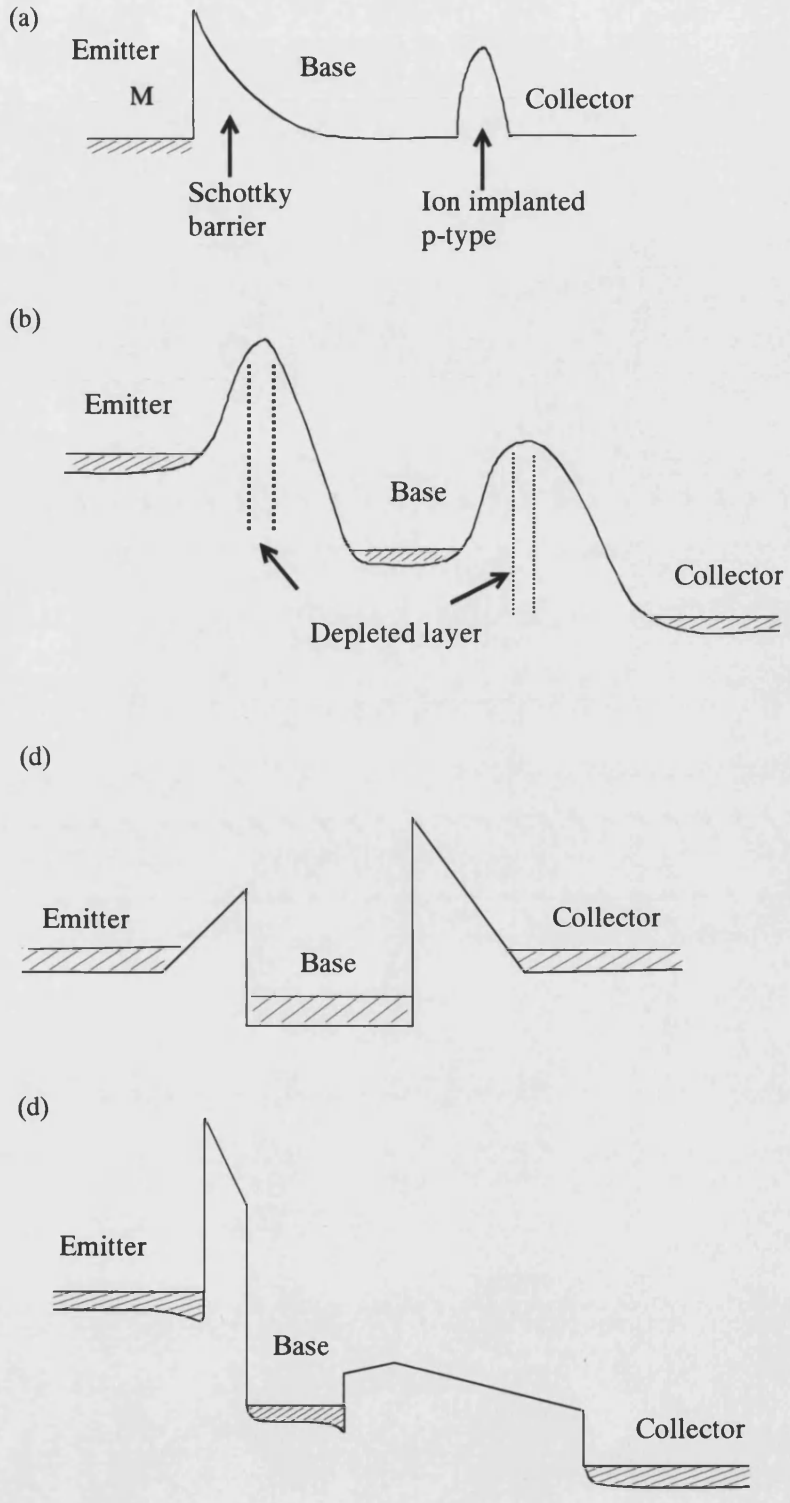

Fig. 4.3 Conduction band profiles of (a) Shannon's "Camel" transistor (b) the Planar Doped Barrier Transistor (PDBT) (c) the Graded-Gap emitter barrier transistor and (d) the Tunnelling Hot Electron Transfer Amplifier (THETA).

4.2.2 Operation Principles of THETA

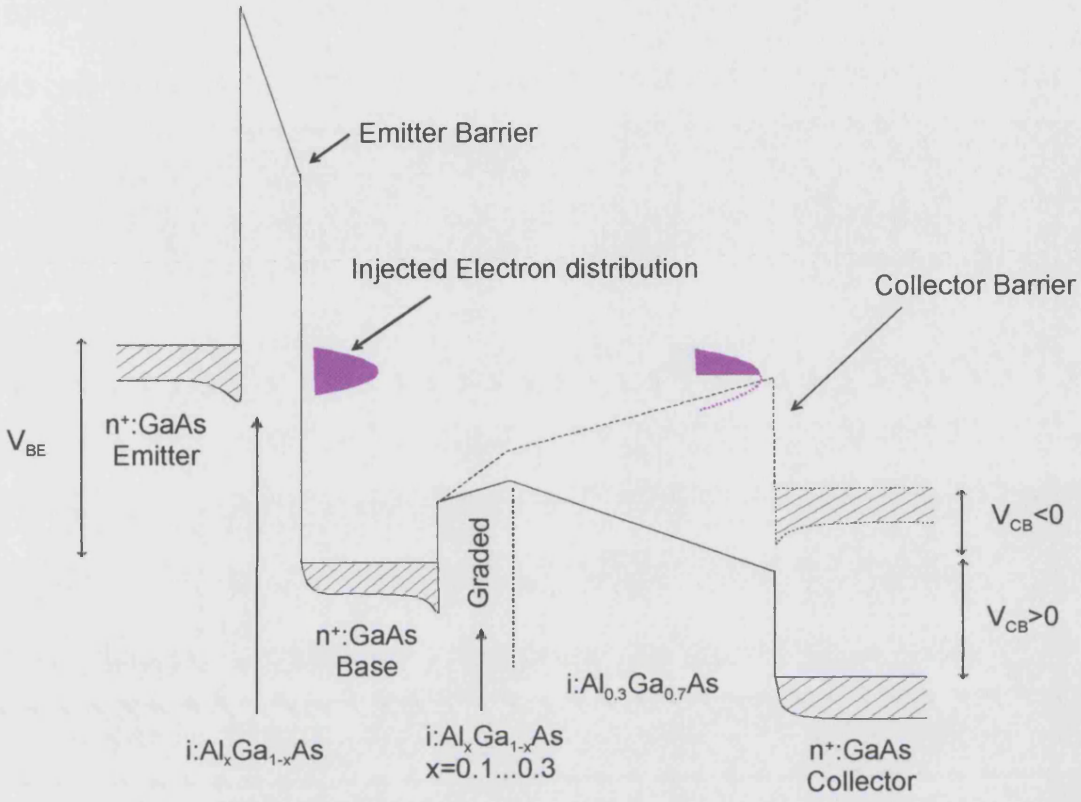

Fig 4.4 Schematic conduction band profile of a THETA device.

Upon applying a bias to the emitter barrier electrons are tunnel injected through the emitter barrier into the narrow base. The energy distribution of the injected electrons forms a quasimonoenergetic peak due to the convolution of the transmission coefficient for the electrons through the emitter barrier and the Fermi-Dirac distribution. In the base region the injected electrons possess excess energy which depends on the applied bias.

Since the base region is very narrow scattering between injected electrons and thermalised electrons, longitudinal optical (LO) phonon and ionised donors is minimised and a substantial fraction of the injected electrons can traverse the narrow base region quasi-ballistically.

The collector barrier is graded on the base side to provide a bias dependent barrier height and to reduce the quantum mechanical reflection at the base- collector barrier interface (Chandra and Eastman 1982, Heiblum *et al.* 1986). Upon negatively and positively biasing the collector barrier a spectral analysis of the electrons which traverse the base region quasi-ballistically can be performed.

4.2.3 Hot Electron Spectroscopy Using the THETA Device

The current-voltage characteristic of a THETA device is found to be monotonic and featureless despite the presence of a strongly peaked ballistic component. Consequently a method of energy spectroscopy is found to be a valuable tool for characterising ballistic transport. Electron spectroscopy in GaAs was proposed by Hesto *et al.* (1980). Using Monte Carlo simulations these authors were able to characterise the ballistic transport of electrons and LO phonon scattering in a submicron GaAs region. Hayes *et al.* (1985) first realised the technique called "Hot Electron Spectroscopy" in planar doped barrier transistors. Heiblum *et al.* (1985a) subsequently used this method in the THETA device to analyse the energy of electrons injected into the base layer.

Since the structure studied in this work is similar to the THETA device, we shall only describe hot electron spectroscopy performed using it.

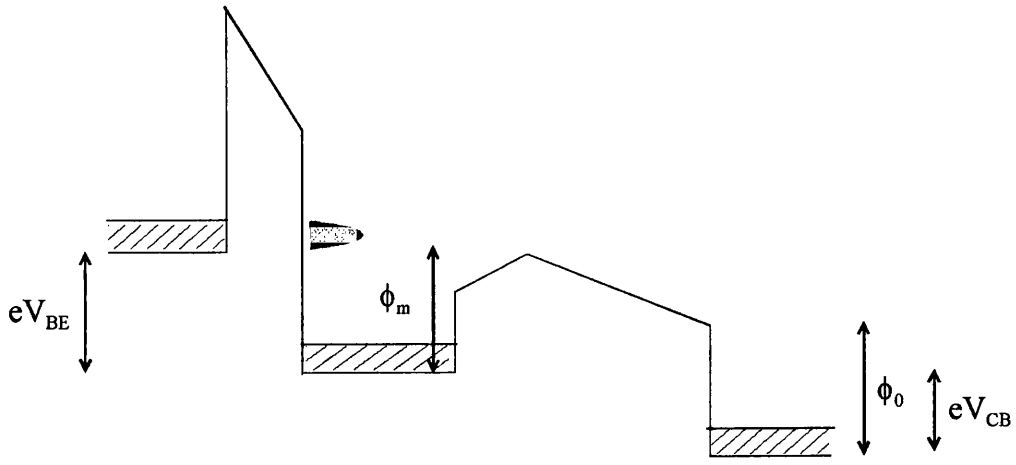

Fig. 4.5 Schematic conduction band edge profile of a transistor structure. Band bending at the interfaces is not shown.

At a given applied bias across both emitter and collector barriers the collector current flowing in a THETA device can be written as,

$$I_C = Ae\int_{\phi_m}^{\infty} n(E_z)v(E)dE_z \qquad (4.2.3.1)$$

where A is the area of the emitter contact, ϕ_m is the energy of the highest point of the collector barrier (or effective barrier height), $n(E_z)$ is the energy distribution of the incident electrons which is strongly peaked and $v(E)$ is the group velocity of the electrons.

Let $\Delta\phi$ be the change in the effective barrier height due to the change in base-collector bias ΔV_{CB}.

The change in the collector current due to the change in ϕ_m can be written as

$$\Delta I_C = Aen(E_z)v(E)\Delta\phi \qquad (4.2.3.2)$$

It is reasonable to assume that group velocity of the electrons is approximately constant across the narrow distribution of injected electrons.

We then obtain from equation (4.2.3.2),

$$\frac{dI_C}{d\phi} \propto n(E_z) \qquad (4.2.3.3)$$

Re-writing this in terms of V_{CB} we obtain,

$$\frac{dI_C}{d\left(V_{CB}/K\right)} \propto n(E_z) \qquad (4.2.3.4)$$

where $K\left(=\frac{\Delta\phi}{\Delta V_{CB}}\right)$ is called the "leverage factor".

For the reverse biased collector barrier K≅1 and for the forward biased graded collector barrier we calculate the value of K to be 7.7 taking band bending at the interfaces into account. A detailed description of this calculation is given in Chapter 5.

4.3 The Hot Electron Transistor as a Laboratory Tool

Although the high-speed operation of hot electron transistors remains a distant goal, they still provide excellent tools for investigating fundamental physical phenomena. In this section an attempt is made to give a brief account of the physics which can be studied with tunnelling hot electron transistors.

4.3.1 Ballistic Transport

Based on Monte Carlo calculations Shur and Eastman (1981) proposed that the ballistic transport of electrons should be observable at low temperatures in submicron GaAs devices. Using the hot electron transistor as an energy spectrometer experimental evidence for ballistic transport of electrons in GaAs was given by Levi *et al.* (1985), Heiblum *et al.* (1985a) and Bending *et al.* (1989a). Using a p-type THETA device the ballistic transport of light-holes was also demonstrated by Heiblum *et. al.* (1988)

4.3.2 Energy Relaxation

The energy loss of electrons injected into the narrow base region is mainly due to scattering from longitudinal optical (LO) phonons, plasmons, ionised impurities and unavoidable imperfections in the crystal. If the injection energy of electrons exceeds the L-Γ (X–Γ) separation, a fraction of electrons may be scattered to the L-point (X-point) conduction band minima.

Using a specially designed THETA structure (Fig. 4.6) LO phonon emission by hot electrons in an n^+-GaAs base and an undoped collector barrier were reported by Heiblum *et al.* (1989). Note that LO phonon emission was not observed in the original THETA structure shown in Fig 4.3 d. Recently LO phonon emission by holes has been demonstrated by employing a p-type THETA device with a high purity GaAs base (Sprinzak *et al.* 1997).

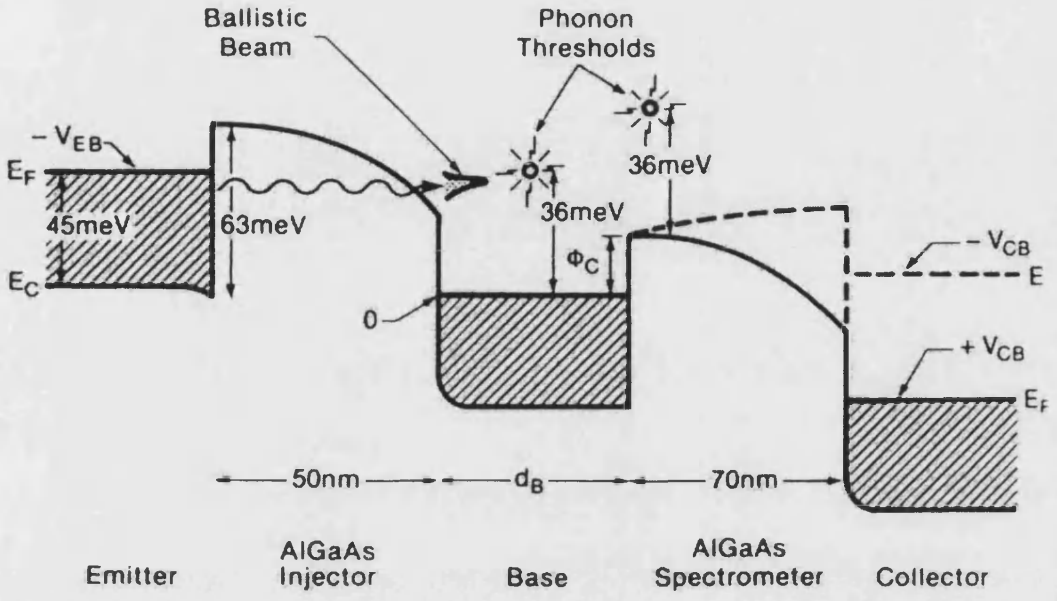

Fig. 4.6 Conduction band profile of a specially designed THETA device structure for resolving energy relaxation mechanisms taking place in the base region (Heiblum *et al.* 1989).

Hayes *et al.* (1986) suggested that hot electrons are scattered in heavily doped GaAs by coupled plasmon/phonon collective modes as at high carrier concentrations the longitudinal plasmon and phonon modes do not exist independently. Hayes *et al.* (1986) and Heiblum *et al.* (1989) looked for these coupled modes in heavily doped GaAs, but no clear experimental evidence was found to support their involvement.

Geim *et al.* (1992) investigated the scattering of hot electrons in the base region of a THETA device. They illuminated the device with light of different wavelengths and found that the distribution of hot electrons is affected by scattering from ionised impurities.

Using a THETA device with a 10 nm thick n^+-GaAs base, a thick high purity n^--GaAs drift region and a lower collector barrier of a few tens of millielectronvolts (Fig. 4.7) Brill *et al.* (1996) showed that a very long mean free path for ballistic

transport can be achieved at low temperatures for electrons injected into high purity GaAs with energy below the threshold for LO-phonon emission. They also suggested that the major energy loss mechanism is impact ionisation and excitation of neutral donors by hot electrons.

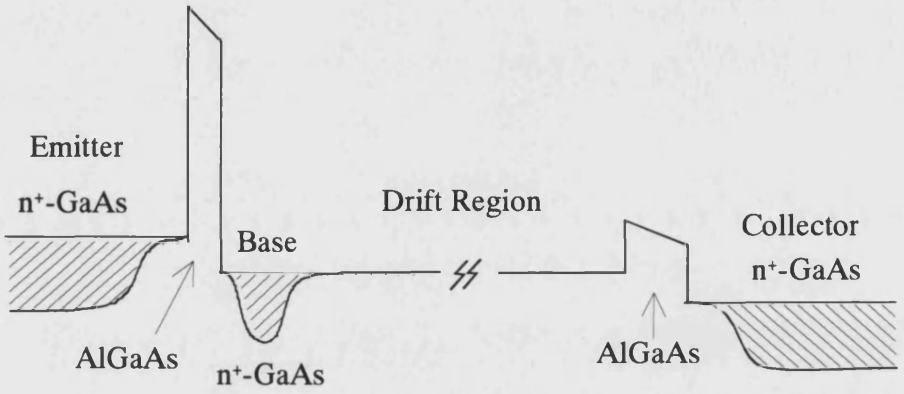

Fig. 4.7 Schematic conduction band profile of a modified THETA device containing a narrow (10nm) base layer and a thick high purity GaAs drift region (Brill *et al.* 1996).

By applying hydrostatic pressure to reduce the L-Γ separation, evidence for transfer of electrons to the L valley was reported by Heiblum *et al.* (1986). The electrons which transfer to the L-point conduction band minima will be reflected by the L-point AlGaAs barrier at the base/collector interface and contribute to the base current.

4.3.3 Two Dimensional Electron Gas Base HET

The hot electron transistor requires low resistance Ohmic contacts to the electrodes in order to realise near ideal high frequency performance. This is normally achieved by heavily doping the GaAs contact regions. The heavily doped base, however, increases the scattering of injected electrons and reduces device gain. In order to overcome this problem a hot electron transistor structure with a two dimensional electron gas base was proposed by Bending *et al.* (1989b). The 2DEG

can be formed in the base region at the base-collector (or base-emitter) interface by asymetrically doping the collector (emitter) barrier. A hot electron transistor structure with a modulation doped collector barrier which produces a 2DEG at the base-collector interface (Fig 4.8) was reported by Mathews *et al.* (1990).

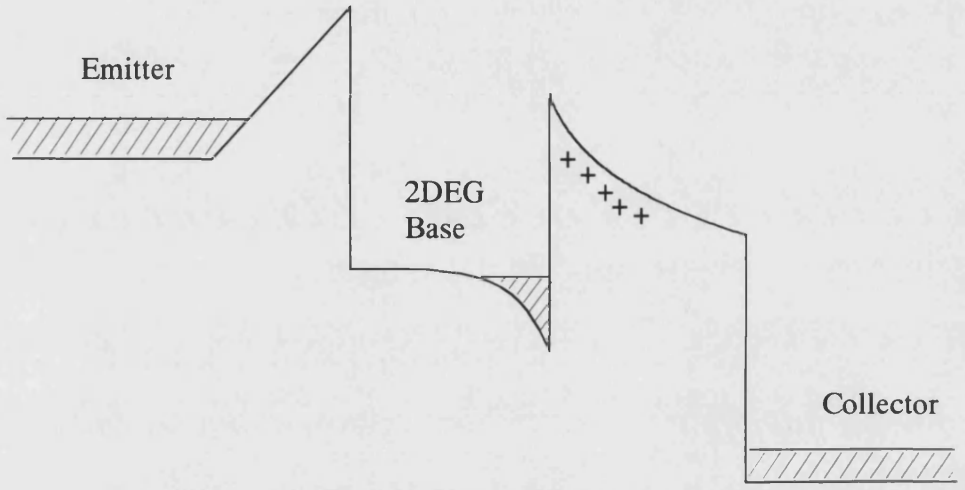

Fig 4.8 Schematic conduction band edge profile of a two-dimensional electron gas base hot electron transistor (Mathews *et al.* 1990).

4.3.4 Electron – Electron Interactions

Using a 2DEG base hot electron transistor Mathews *et al.* (1990) studied the interaction between the hot electrons and the thermalised electrons in the base layer. Employing a THETA device with a low collector barrier (Fig. 4.9) Brill *et al.* (1994) also showed that the electrons in the base Fermi sea are excited over the collector barrier by the injected hot electrons. They found that the transfer factor exceeds unity for high enough injection energies.

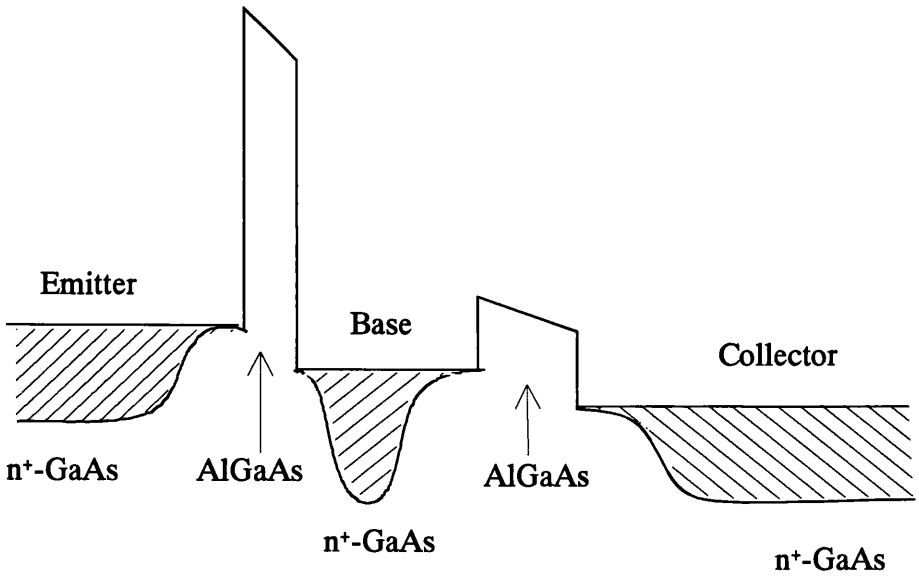

Fig. 4.9 Schematic conduction band profile of a THETA device with a low collector barrier for studying electron-electron interactions (Brill *et al.* 1994).

The fact that the base current reverses in direction when the d.c current transfer ratio exceeds unity caused Dellow *et al.* (1994) to propose a high frequency device which is capable of producing 700 GHz radiation.

4.3.5 Resonant Tunnelling

Yokoyama *et al.* (1985) proposed a Resonant-tunnelling Hot electron Transistor (RHET) (Fig. 4.10) which uses a double barrier resonant tunnelling structure as the emitter. The main advantage of this design is that the resonant tunnelling emitter generates a mononenergetic beam of hot electrons and the collector current displays a region of negative transconductance. It was demonstrated that RHET's are capable of performing Exclusive-NOR and flip-flop logic function when connected to appropriate circuitry (Mori *et al.* 1986).

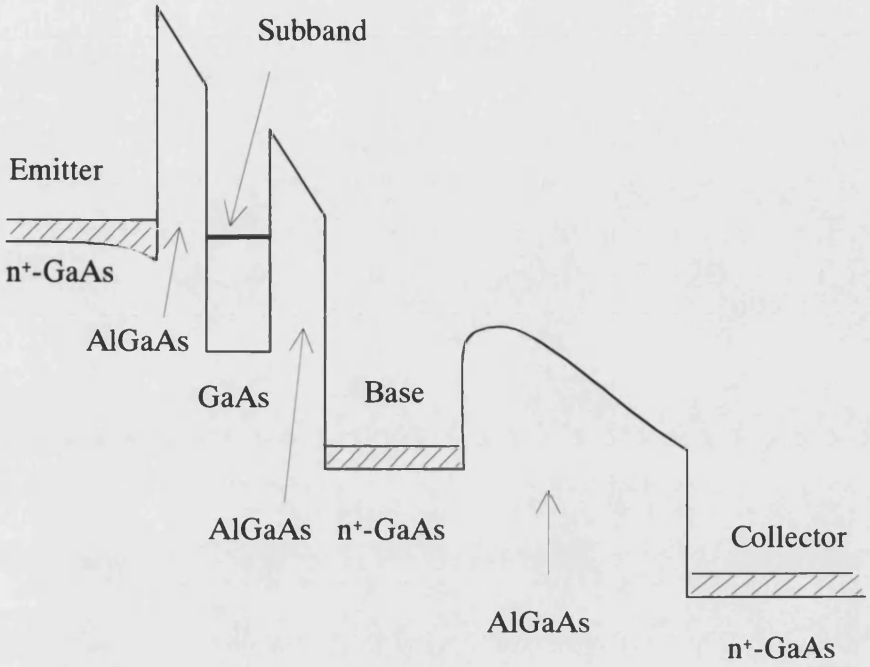

Fig. 4.10 Schematic conduction band edge profile of a Resonant tunnelling Hot Electron Transistor (RHET) (Yokoyama *et al.* 1985).

Bending *et al.* (1989c) incorporated a narrow quantum well into the collector barrier to study resonant tunnelling processes. Lam *et al.* (1995) demonstrated the breakdown of parallel momentum conservation in tunnelling through an AlAs/GaAs/AlAs double barrier structure incorporated into the collector barrier of a THETA device (Fig. 4.11). Miniband transport through a superlattice was also investigated by replacing the collector barrier by an AlGaAs/GaAs superlattice (Fig. 4.12) (Lam *et al.* 1993, Rauch *et al.* 1997).

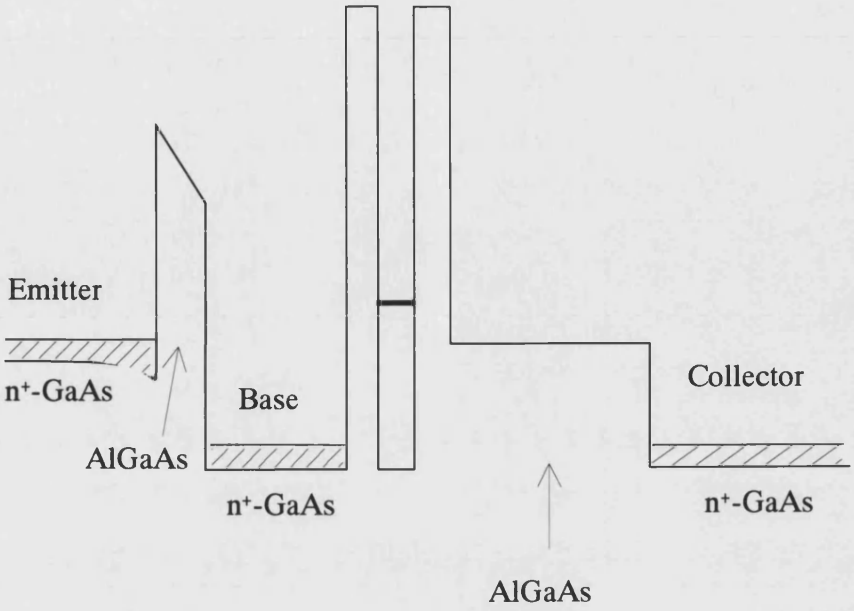

Fig. 4.11 Schematic conduction band profile of a THETA device containing a double barrier structure (Lam *et al.* 1995).

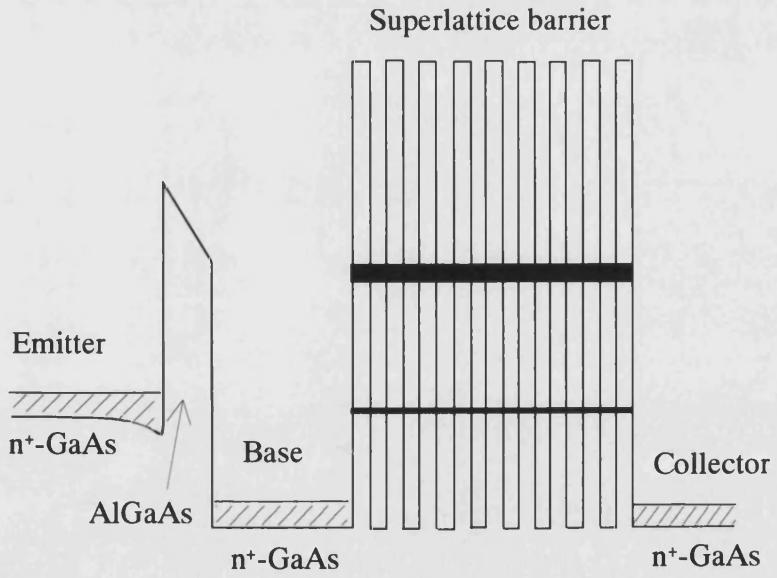

Fig. 4.12 Schematic conduction band profile of a THETA device containing a superlattice structure.

4.3.6 Tunnelling Through Indirect Barrier

The work described in this thesis is mainly concerned with the transport of electrons through indirect AlAs barriers. The investigations were performed by incorporating the indirect AlAs barrier into the emitter barrier of a tunnelling hot electron transistor structure (Fig. 4.13).

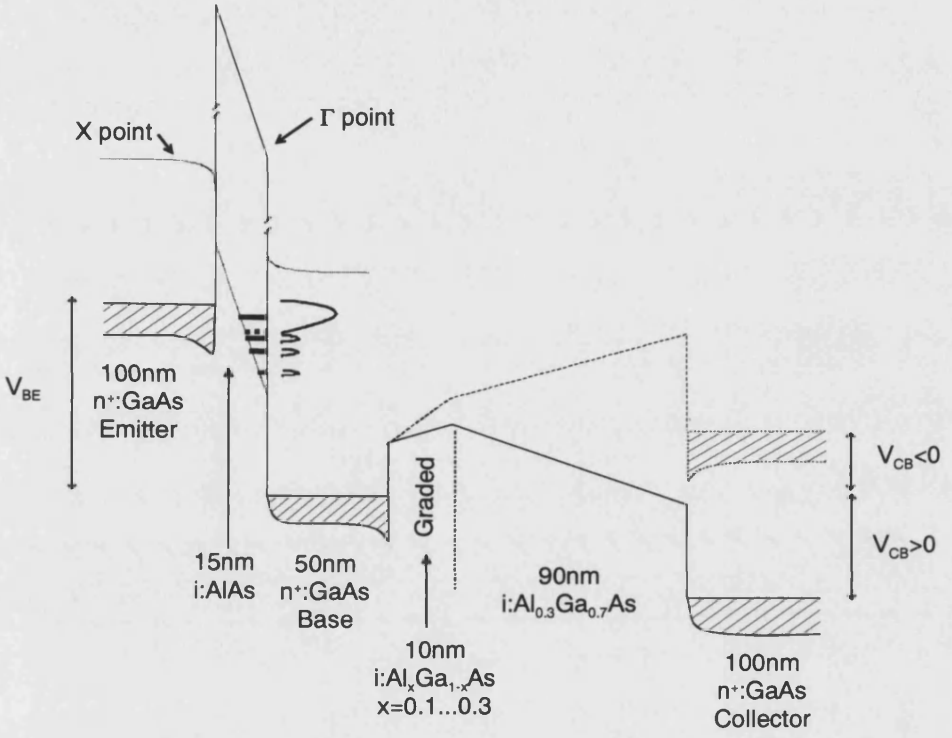

Fig. 4.13 Schematic conduction band profile of a THETA device with an AlAs emitter barrier. The solid (dotted) line represents the Γ-point (X-point) conduction band minima. The calculated edges of the longitudinal and transverse X-point subbands are also shown.

We have studied transport mechanisms in AlAs barriers by performing hot electron spectroscopy on the electrons injected into the base and comparing the results with a direct $Al_{0.5}Ga_{0.5}As$ emitter barrier transistor. Since X-point related transport processes become important in indirect AlAs barriers, we have applied hydrostatic pressure to systematically vary the Γ-X offset leaving the Γ-Γ offset unaffected. In this way the relative importance of the Γ and X minima in transport can be assessed.

Chapter 5

Experimental Methods

5.1 Introduction

The transistor structures were grown by Molecular Beam Epitaxy (MBE) at the School of Physics and Astronomy, University of Nottingham. The transistors were fabricated using the clean room facilities in the Department of Physics, University of Bath. The following sections give a detailed account of the processing techniques used to realise the devices, measurement set up, measurement circuits and characterisation techniques.

5.2 Sample details

The device structures were grown on (100) oriented n^+-GaAs substrates by molecular beam epitaxy (MBE). The devices are composed of three n^+-GaAs regions separated by $Al_xGa_{1-x}As$ potential barriers of thickness 15nm and 100nm respectively. A key consideration is that the central n^+-GaAs layer be very narrow (50nm) to allow ballistic transport through it. We have studied two types of device structure which are identical except for the 15nm $Al_xGa_{1-x}As$ emitter injection barrier where x=0.5 in the first case and x=1.0 in the second. A detailed description of the layers is given in table (5.1).

Layer No.	Thickness (nm)	Material	Doping density	Descriptions
1	10	GaAs	2-5x10^{18} cm^{-3}	Cap layer
2	220	GaAs	1x$10^{18}$$cm^{-3}$	Emitter
3	3	AlAs	1x$10^{18}$$cm^{-3}$	Etch stop layer
4	30	GaAs	1x$10^{18}$$cm^{-3}$	Emitter
5	5	GaAs	Undoped	Spacer
6	15	$Al_{0.5}Ga_{0.5}As$ or AlAs	Undoped	Emitter barrier
7	5	GaAs	Undoped	Spacer
8	50	GaAs	1x$10^{18}$$cm^{-3}$	Base
9	10	$Al_xGa_{1-x}As$ x: 0.1 to 0.3	Undoped	Graded region of collector barrier
10	90	$Al_{0.3}Ga_{0.7}As$	Undoped	Collector barrier
11	500	GaAs	1x$10^{18}$$cm^{-3}$	Collector
12	195		2x$10^{18}$$cm^{-3}$	Supperlattice buffer
13	30	GaAs	2x$10^{18}$$cm^{-3}$	
14		GaAs		Substrate

Table 5.1 Description of device structures grown by MBE.

The sequence of MBE grown layers for the transistor structure and the conduction band edge profile without applied bias are shown in Fig. 5.1.

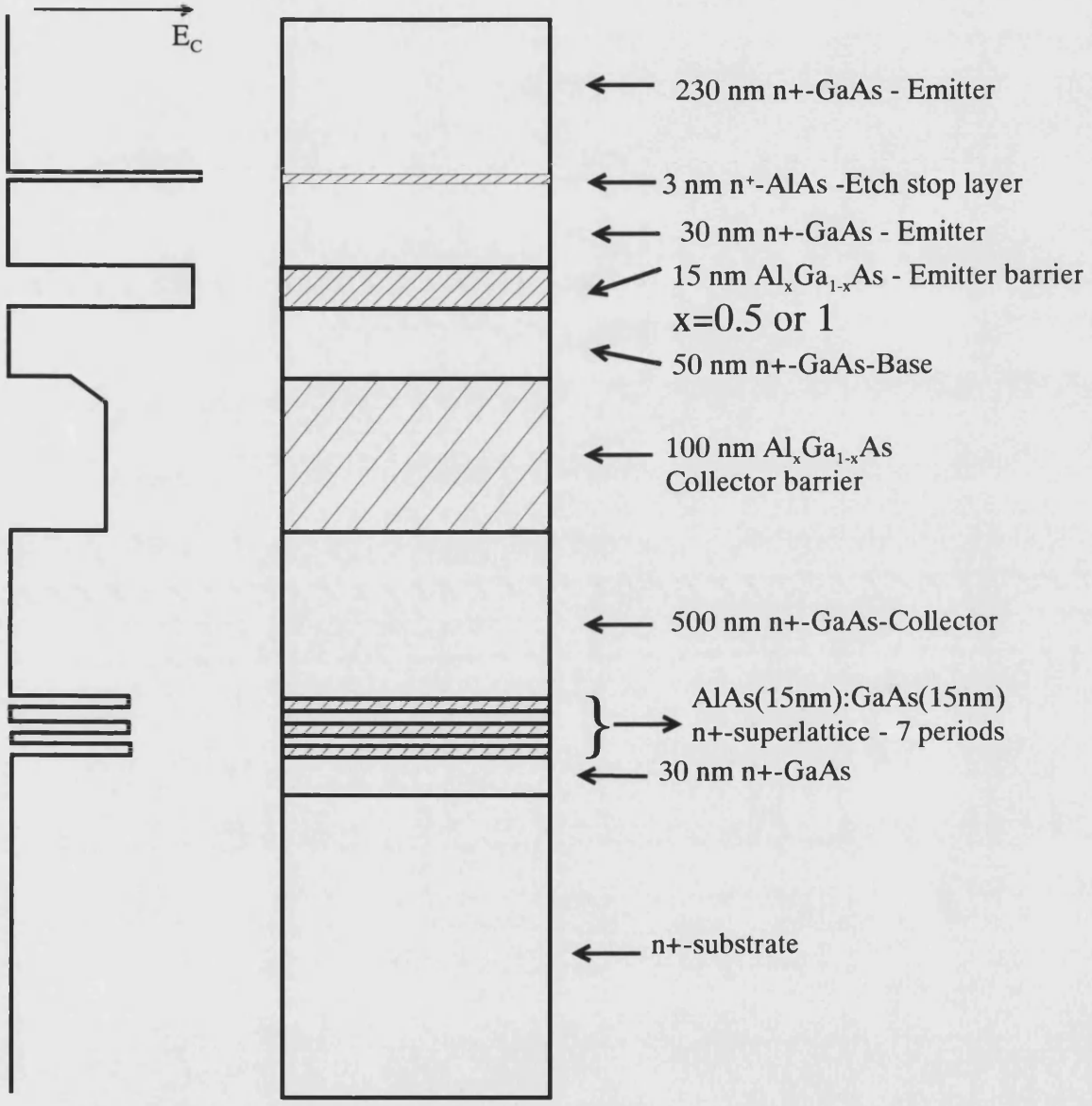

Fig. 5.1 (a) A sketch of conduction band profile and (b) MBE growth layer sequence of the transistor.

5nm undoped GaAs spacers are incorporated on both sides of the barriers in order to prevent the diffusion of dopants into them. The collector electrode is terminated by 7 periods of a doped $Al_{0.1}Ga_{0.9}As$/GaAs superlattice buffer for trapping impurities and dislocations. The collector barrier is graded from x=0.1 to 0.3 over 10nm on the base side in order to reduce quantum mechanical reflections and to provide a voltage dependent barrier height. A thin layer (3nm) of doped AlAs is included in the emitter contact of the structure to act as an etch stop.

5.3 Photolithography

In semiconductor fabrication photolithography refers to the process of transferring a pattern from a mask to a wafer/chip coated with an organic polymer called resist or photoresist which is sensitive to ultra violet (u.v) light. Photoresist is classified into two categories: positive and negative photoresist. When the positive (negative) resist is exposed to u.v light the exposed area becomes soluble (insoluble) in an appropriate developer solution. To coat samples with a nearly uniform layer of resist they are placed on a spinner chuck and held by a vacuum. One or two drops of photo resist is applied to the chip and spun off. Spinning levels the resist by the action of the centripetal force and evaporates the solvents to partially dry the resist film. The thickness of the photoresist depends on the spin speed and on the viscosity of the photoresist (Moreau 1988). The photoresist coated sample is then soft baked (or prebaked) at 90°C for 30 minutes to remove solvents present in the photoresist and to convert the resist into a solid film. The soft baking also improves adhesion of the resist onto the substrate and slightly decreases the thickness of the resist film (Moreau 1988). Fig. 5.2 illustrates the process of formation of a pattern using positive resist.

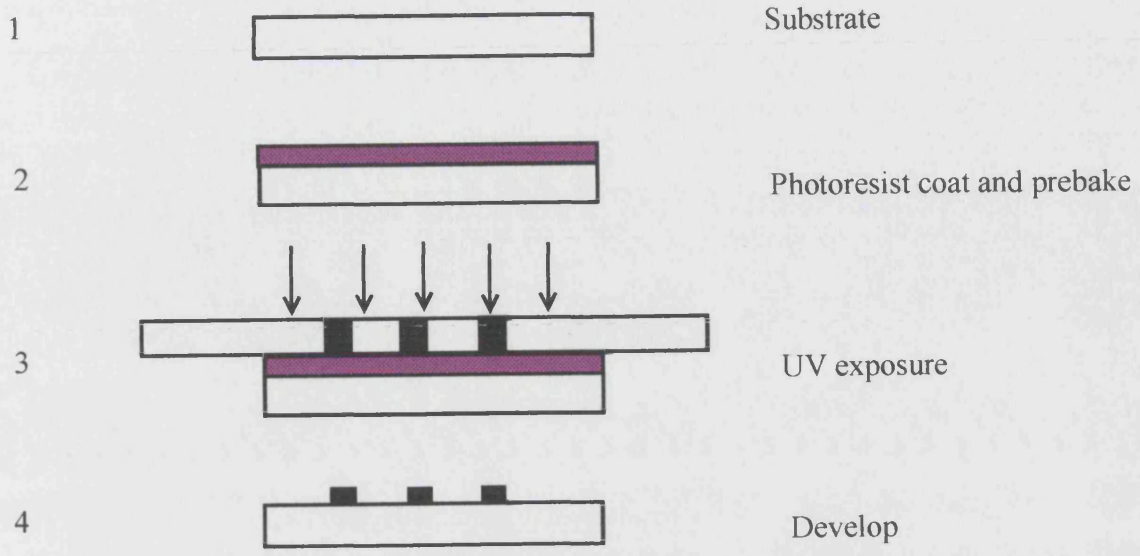

Fig. 5.2 A schematic of the lithographic steps of spinning, exposing and developing a pattern in a positive photoresist.

When the sample is patterned for deposition, it is necessary to form an overhang profile for getting successful lift-off of unwanted deposited film from the substrate as illustrated in Fig. 5.3. There are several methods to achieve this. The most simple method is to treat the photoresist in chlorobenzene after the resist was exposed to uv light (Hatzaki *et al.* 1980). The cholorobenzene removes lower molecular weight resin from the outer most surface of the photoresist, thus reducing the dissolution rate in the developer solution.

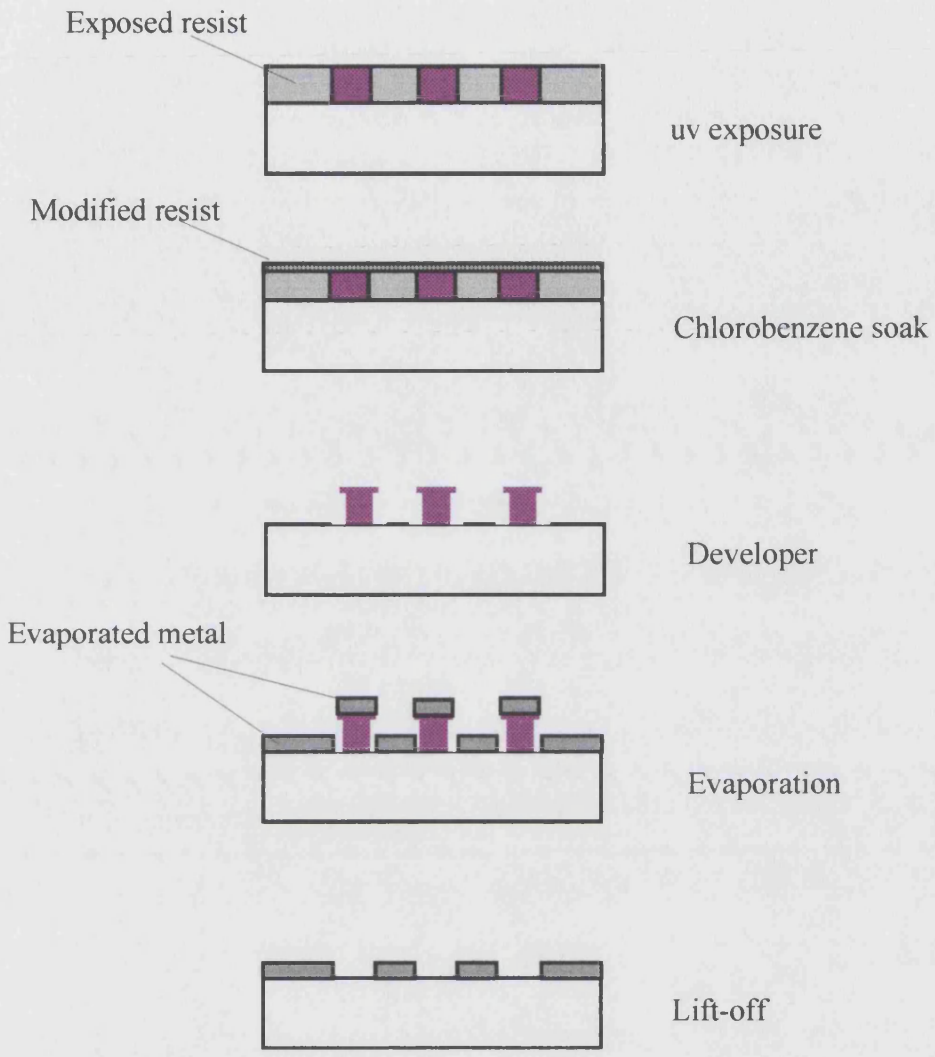

Fig. 5.3 Schematic of lift-off process with chlorobenzene treated resist.

When the sample is patterned for etching the developed resist is post baked at 85°C for 30 minutes in order to restore the adhesion of the resist after weakening by the developer.

5.4 Contact formation

Semiconductors are contacted by depositing metals or metallic alloys onto them. This results in a built-in potential at the junction because of electron diffusion across the junction to line up the Fermi levels of the metal and the semiconductor (Sze 1981) as shown in Fig. 5.4.

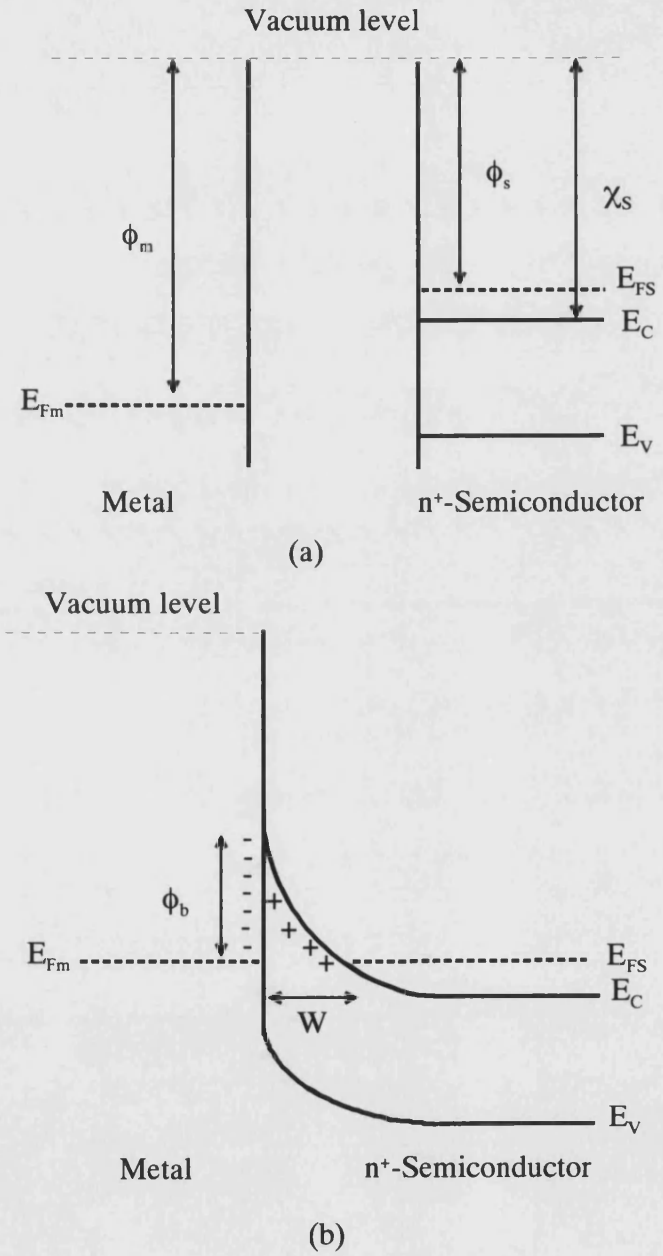

Fig. 5.4 A schematic diagram of the formation of a Schottky barrier.

The height of the Schottky barrier is given by

$$e\phi_b = e\phi_m - e\phi_S - (E_{FS} - E_C) \quad (5.4.1)$$

$$= e\phi_m - e\phi_S - e\chi_s \quad (5.4.2)$$

where ϕ_m is the work function of the metal (in volts), ϕ_S is the work function of the semiconductor (in volts) and χ_s is the electron affinity of the semiconductor.

The width of the depletion region in the absence of an applied bias across the junction is given by (Singh 1994),

$$W = \left(\frac{2\varepsilon V_{bi}}{eN_d} \right)^{1/2} \quad (5.4.3)$$

where V_{bi} is the built in potential, N_d is the doping density, and ε is the dielectric constant for the semiconductor.

According to equation 5.4.2 the Schottky barrier height depends on the metal and the semiconductor work functions. However in practice the Schottky barrier height of GaAs is only weakly dependent on the metal work function due to the pinning of Fermi level at the semiconductor surface states (Singh 1994).

The current flows across the Schottky barrier via a number of different mechanisms. The dominant mechanism is thermionic emission over the barrier. Electrons can also tunnel through the barrier quantum mechanically. Other mechanisms include recombination in the space charge region and hole injection from the metal to the semiconductor.

To realise near-ideal Ohmic contacts it is important to obtain low contact resistances to the device in order to get very much less voltage drop across the contacts than the active regions of the device. This is achieved by heavily doping the semiconductor layer underneath the metal. Heavy doping reduces the depletion layer width making electron tunnelling the dominant transport process (Fig. 5.5). In the tunnelling regime the contact resistance decreases exponentially with increasing doping density.

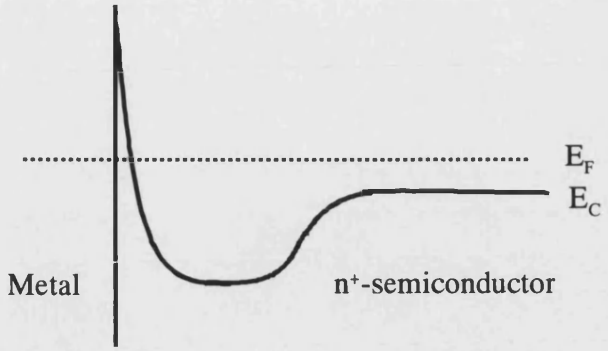

Fig. 5.5 Band diagram of an Ohmic contact.

Ohmic contacts to n^+-GaAs are usually made by alloying an evaporated eutectic mixture of Au/Ge (88%:12%) (Sze 1981) under an inert gas. During alloying the Ga diffuses into the metal leaving behind vacant gallium sites in the GaAs lattice which are then occupied by the inter-diffusion of germanium, thus heavily doping the surface layer just beneath the metal. Nickel is sometimes used to prevent balling up of the contact metallisation and to aid the inter-diffusion of the Ge into GaAs during alloying (Williams 1984). It was omitted here since rather shallow Ohmic contacts were required.

5.5 Wet Etching

In order to restrict the current flow within the desired regions unwanted areas of the material are made inactive. Among the several techniques available to achieve this (such as ion implantation, plasma etching) the most commonly used one is wet etching using an appropriate choice of chemical solutions. The etchant is a mixture of two or more chemical solutions, one of which oxidises the semiconductor while the other removes the oxide from the surface. The rates of the following processes determine the etch rate of the overall semiconductor material (Sze 1985): transport of the etchant to the surface, the chemical reaction that oxidises the material, and the removal of the oxide from the surface.

5.6 Fabrication of Transistors

We fabricated batches of transistors of dimensions 30μm×10μm, 45μm×15μm, 60μm×20μm, and 75μm×25μm using conventional photolithography, metallisation and wet etching techniques. To facilitate handling the samples are normally mounted on a clean cover slip using photo resist and baked at 85°C for 30 minutes. The samples were coated with Shipley Microposit SU1813 photoresist and exposed through a u.v mask using a Karl Suss mask aligner. Microposit 351 developer diluted (1:3.5) in water was used for developing the exposed resist.

The following sections give detailed accounts of the fabrication methods used to realise the transistors.

5.6.1 Sample preparation

The MBE grown wafer was scribed into 4mm×5mm chips. The indium on the backside of the wafer, which is used to mount the substrate for MBE growth, was then lapped off. The chips were first degreased in trichloroethane in an ultrasonic bath for 5 minutes followed by ultrasonic cleaning in acetone and propanol for 5 minutes. Finally the chips were rinsed in hot propanol for 5 minutes and dried by blowing N_2 gas over them.

5.6.2 Back collector contact

The cleaned chips were mounted on a pre-cleaned microscope slide face down using a drop of photo resist and were baked at 85°C for 30 minutes. The metal sources and Tungsten boats were cleaned ultrasonically in trichloroethane, acetone and propanol for 5 minutes in each solvent. Before loading the chips into the evaporator the native oxide was removed by dipping the chips in conc HCl : H_20 1:1 solution for 1 minute followed by rinsing in distilled water for 1 minute. The chips were then dried by blowing N_2 gas over them.

The metals and samples were loaded into a thermal evaporator chamber and a vacuum of 1×10^{-6} mbar was obtained. The boats and metals were outgassed by

heating them. The substrate heater was turned up to 80°C and an Ar plasma glow process was performed to clean the samples. Au/Ge/Ni (135nm:67.5nm:20nm) was then evaporated onto the chips in that order. The chips were removed from the evaporator and lifted off from the microscope slide by soaking them in acetone. The samples were then cleaned in acetone and propanol ultrasonically and dried by blowing N_2 over them.

The samples were placed on the silicon wafer sample stage of a Halogen lamp thermal annealer with the collector (rear) side of the sample in contact with the Si wafer to prevent contamination of the top emitter layer during alloying. The contact metallisation was alloyed at 430°C for 30 seconds in the Halogen lamp furnace in an inert forming gas (mixture of 85% of N_2 and 15% of H_2) environment.

5.6.3 Emitter and Base contacts

Since contacting the base layer directly is difficult to achieve without shorting collector barrier it was contacted indirectly from the emitter layer. We defined three parallel emitter mesas, the outer two of which are used as base contacts and the middle one as an emitter. The series resistance introduced due to the presence of the emitter barrier can be electronically subtracted using a three-point measurement technique (to be described in section 5.7.2).

The emitter/base contacts were defined using photolithography. Ohmic contacts to the emitter/base were formed by evaporating Au(45nm)/Ge(22.5nm)/ Ti(15nm)/Au(150nm) and alloying them at 350°C for 10 seconds in the forming gas environment. Note that the alloying temperature was reduced to 350°C in order to make shallow Ohmic contacts.

5.6.4 Selective etching

The emitter/base mesas were isolated by selectively etching the n^+-GaAs emitter contact layer. The alloyed metal emitter/base contacts act as self-aligned masks during etching. Since etching depletes the free carriers for some distance underneath the etched region, it is important to determine the optimum etch depth in

order to prevent depletion of carriers in the base contact layer. Although a thin n^+- AlAs layer is included in the device structure as an etch stop, we found that the samples etched down to this point suffered from severe depletion of carriers in the base region. Consequently the device chips were etched for a range of etch depths from 180nm to 220nm in steps of 15nm in order to get a working device. Fig. 5.6 shows the set-up used for the etching.

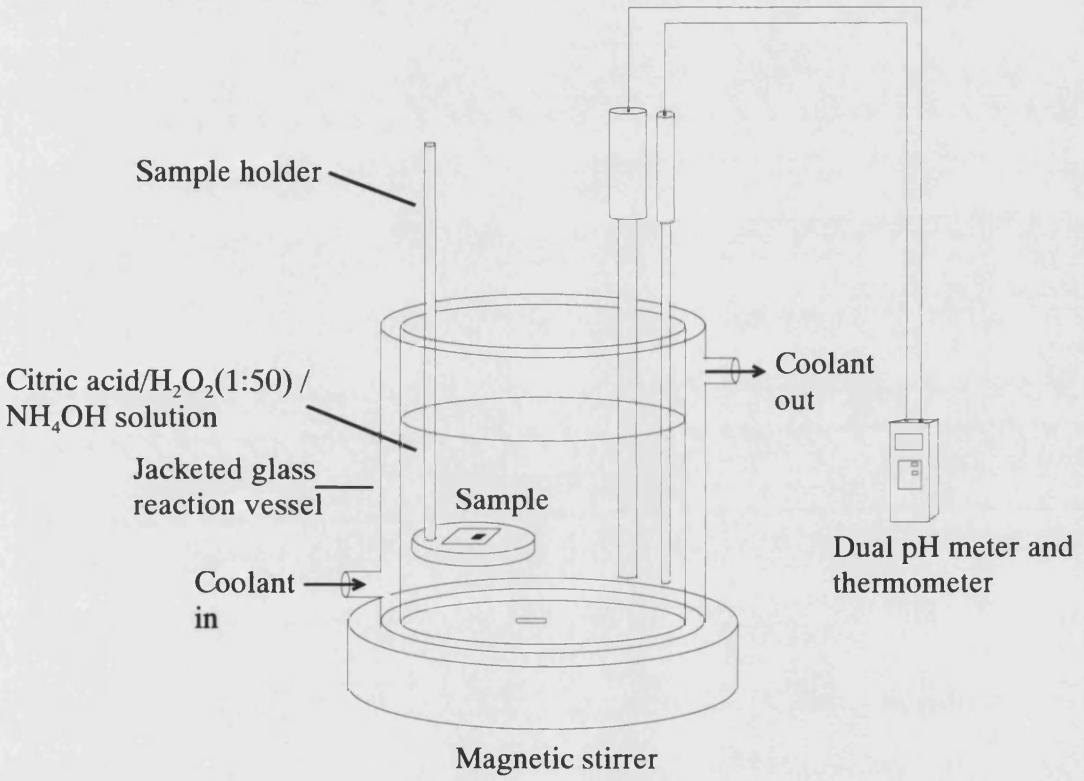

Fig. 5.6 Set-up used for the selective GaAs etchant. A flow-cooler (not shown in the Figure) was used to maintain the temperature of the etchant to a constant value.

A solution of citric acid/NH_4OH/H_2O_2 (1:50) (Kitano *et al.* 1997) was used to selectively etch GaAs preferentially over $Al_xGa_{1-x}As$. The solution was prepared by dissolving citric acid crystals in distilled water to give a 1wt% concentration of citric acid solution followed by the addition of NH_4OH to adjust its pH to 6.5±0.1 and H_2O_2 (30%) to give a volume ratio of 50. The etching was performed in a glass

reaction vessel whose temperature was controlled at 10°C using a flow cooler. The temperature and the pH of the solutions were monitored during etching using a dual thermometer and pH meter. The solutions were agitated using a magnetic flea stirrer. The sample was fixed onto a circular teflon disk allowing free flow of etchant over the sample surface. The etch rate of the solution was determined using GaAs test chips prior to etching the actual device chips. Fig. 5.7 shows a typical calibration curve.

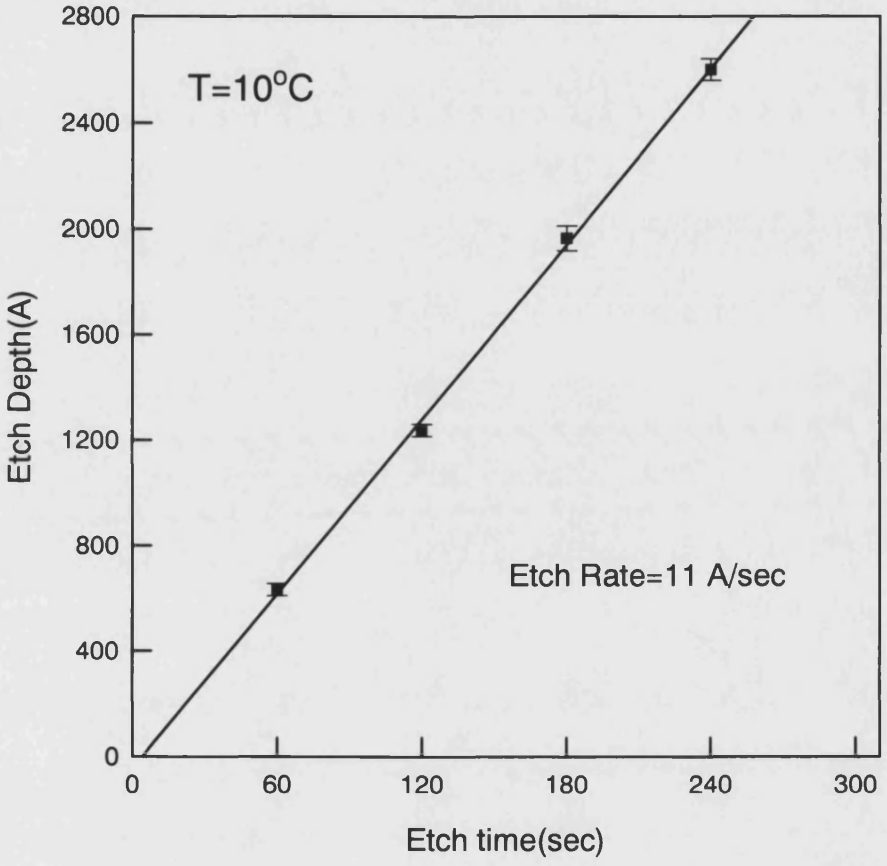

Fig. 5.7 Etch rate calibration graph on GaAs test chips.

5.6.5 Device isolation etching

The individual transistors were defined by etching to a depth beyond the collector barrier to restrict the flow of current within the base layer of the transistor structure. Each transistor structure was masked with hard baked photoresist and a

solution of H_2SO_4 (conc.)/H_2O_2 (30%)/H_2O (1:8:160) (Williams 1984) used as an etchant to isolate the individual transistor structures.

5.6.6 Dielectric deposition and Second level metalisation

The Ohmic contacts were covered in a thick layer of photoresist. A 500nm Si_3N_4 dielectric layer was then sputtered over the whole chip and the Ohmic contact pads were exposed by lift-off. Large area Cr/Au (15nm/200nm) fingers were then evaporated onto them through another contact mask to facilitate wire bonding.

5.6.7 Packaging the chips

The completed chip was mounted onto Cr/Au (30nm/200nm) coated alumina chip carriers using highly conductive two component silver epoxy, which also provided electrical contact to the common collector. The epoxy was cured at 80°C for 90 minutes to make it conducting and to bond the chip onto the carrier. The contact pads of the transistors were connected to the chip carrier with 12.5μm gold wires using an ultrasonic wire bonder. Copper leads were then Indium soldered to the chip carrier bonding pads for making measurements.

5.6.8 Process flow diagram

This section gives a diagrammatic overview of all the processing steps used to realise the transistor.

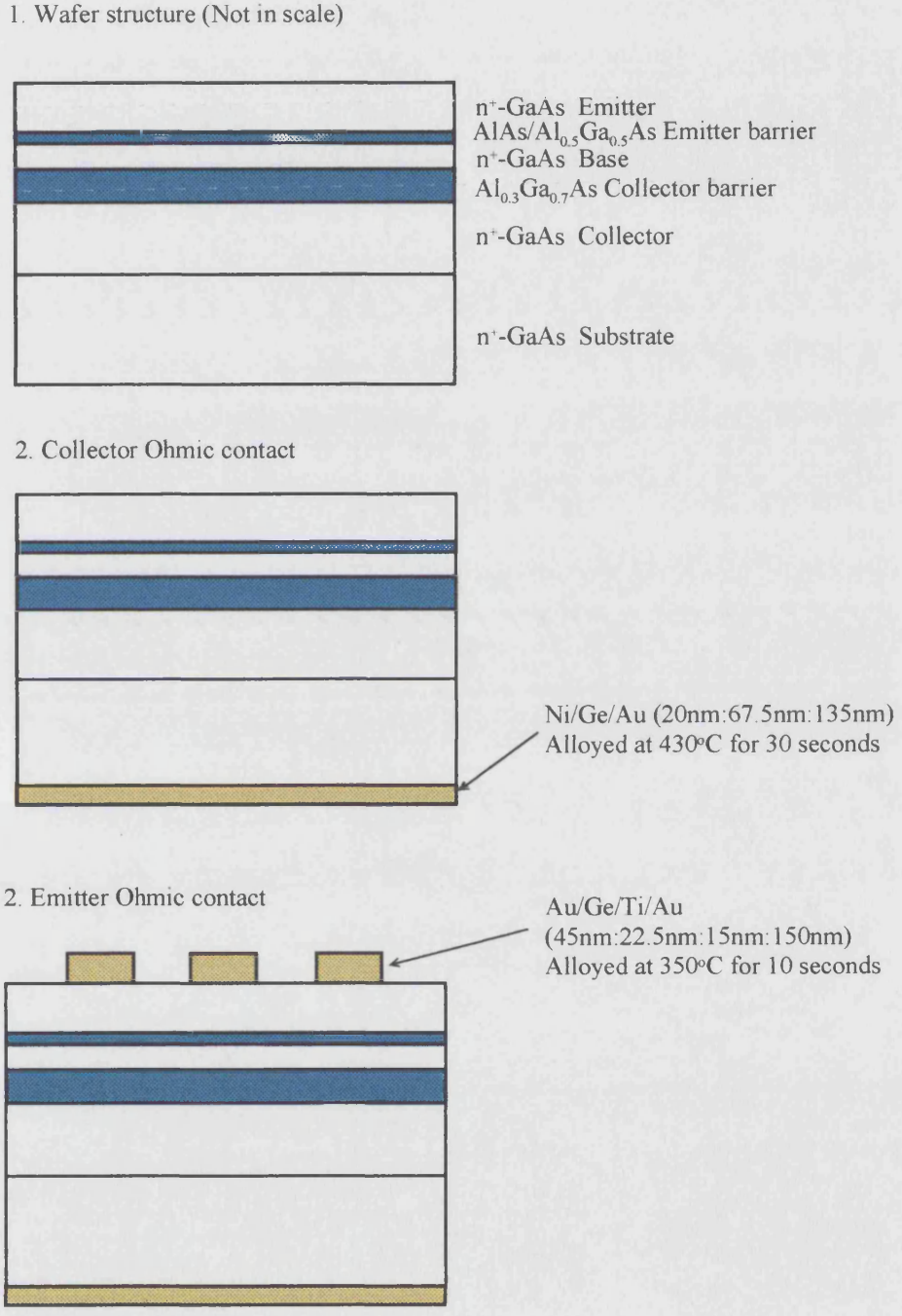

Fig. 5.8a Device Fabrication

4. Selective etching- isolation of base and emitter contacts

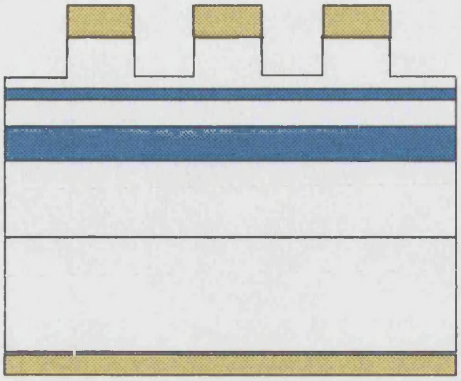

5. Device isolation etch

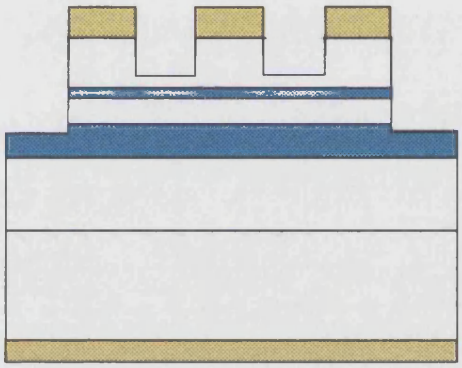

6. Dielectric deposition

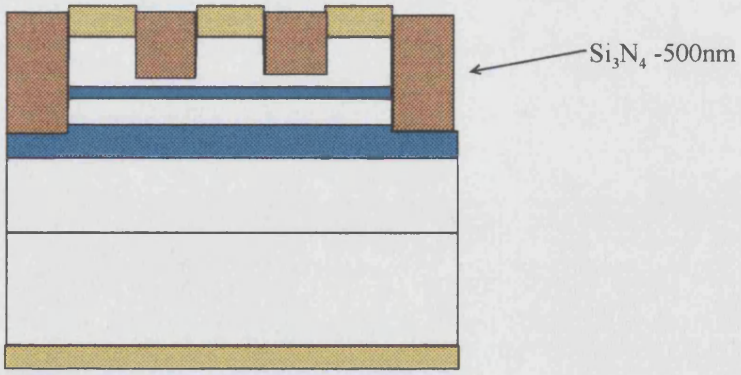

Fig. 5.8b Device Fabrication

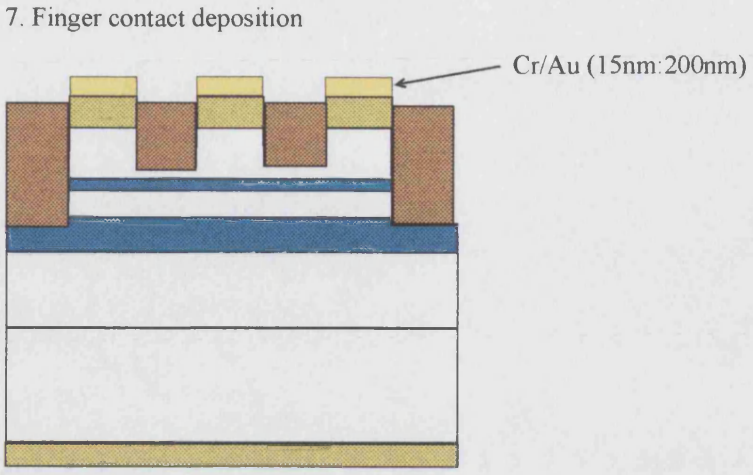

Fig. 5.8c Device fabrication

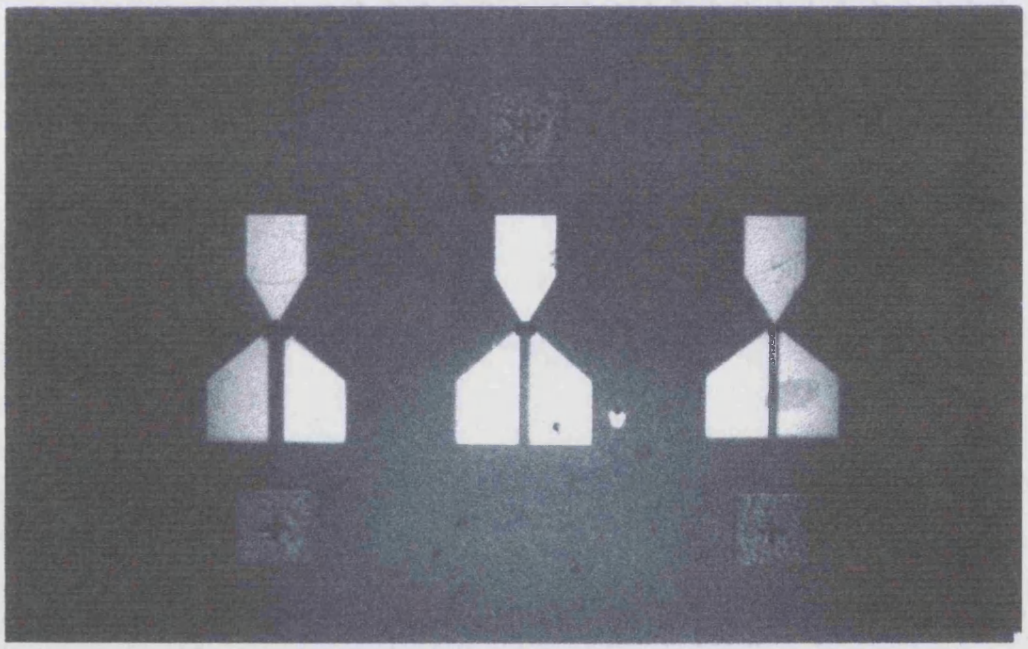

Fig. 5.9 Photograph of a fabricated chip containing three transistors

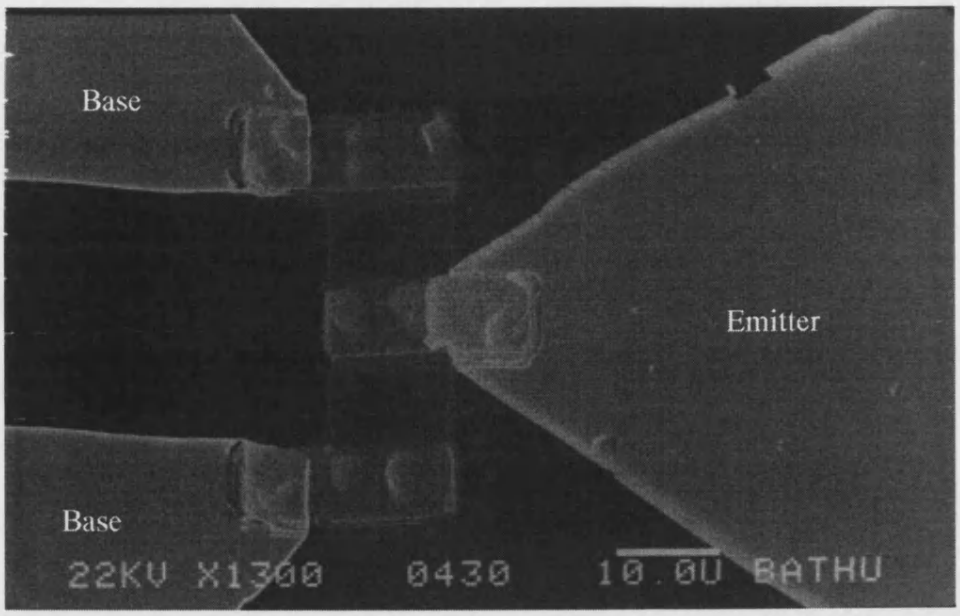

Fig. 5.10 Scanning electron micrograph of the fabricated device.

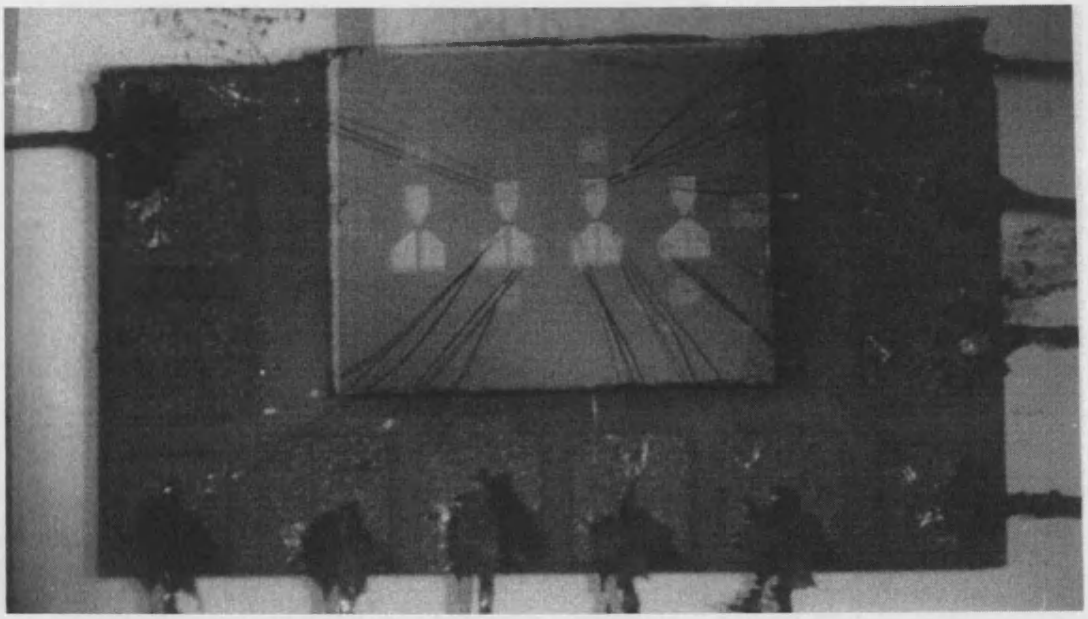

Fig. 5.11 Photograph of a fully packaged chip containing four transistors

5.7 Characterisation Experiments

The transistor can be schematically represented by the conduction band profile as shown in Fig. 5.12. The emitter and collector contacts have negligible resistance. However the fact that the base region was contacted through an emitter barrier introduces a series resistance to the base contacts which is represented by R_B in Fig. 5.12.

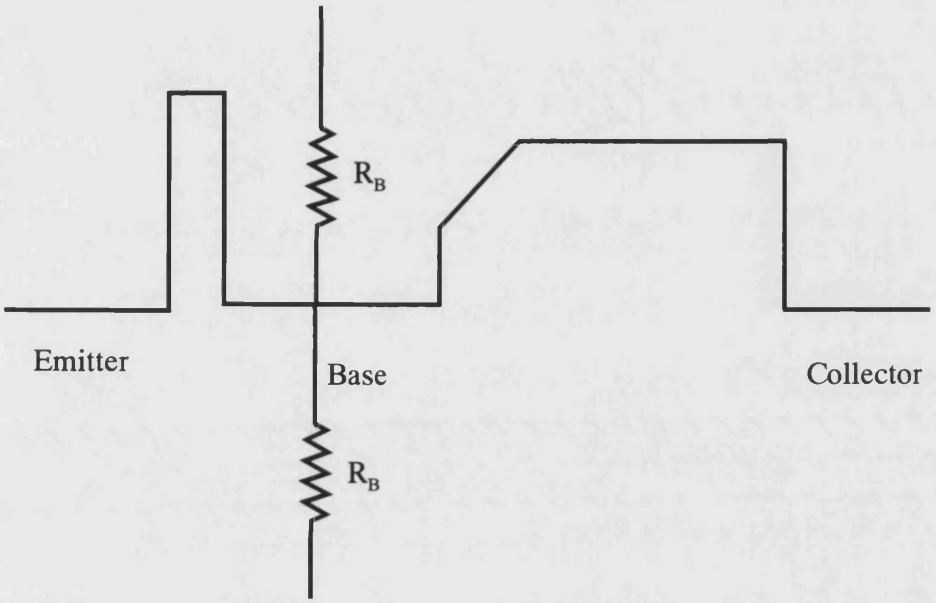

Fig. 5.12 A schematic representation of the tunnelling hot electron transistor.

5.7.1 Measurement system

This section describes the measurement set-up and circuits employed to perform current-voltage and conductance-voltage measurements. A schematic diagram of the measurement set-up is shown in the Fig. 5.13. The sample in this diagram represents a transistor structure connected between two of its three terminals (Emitter, Base and Collector).

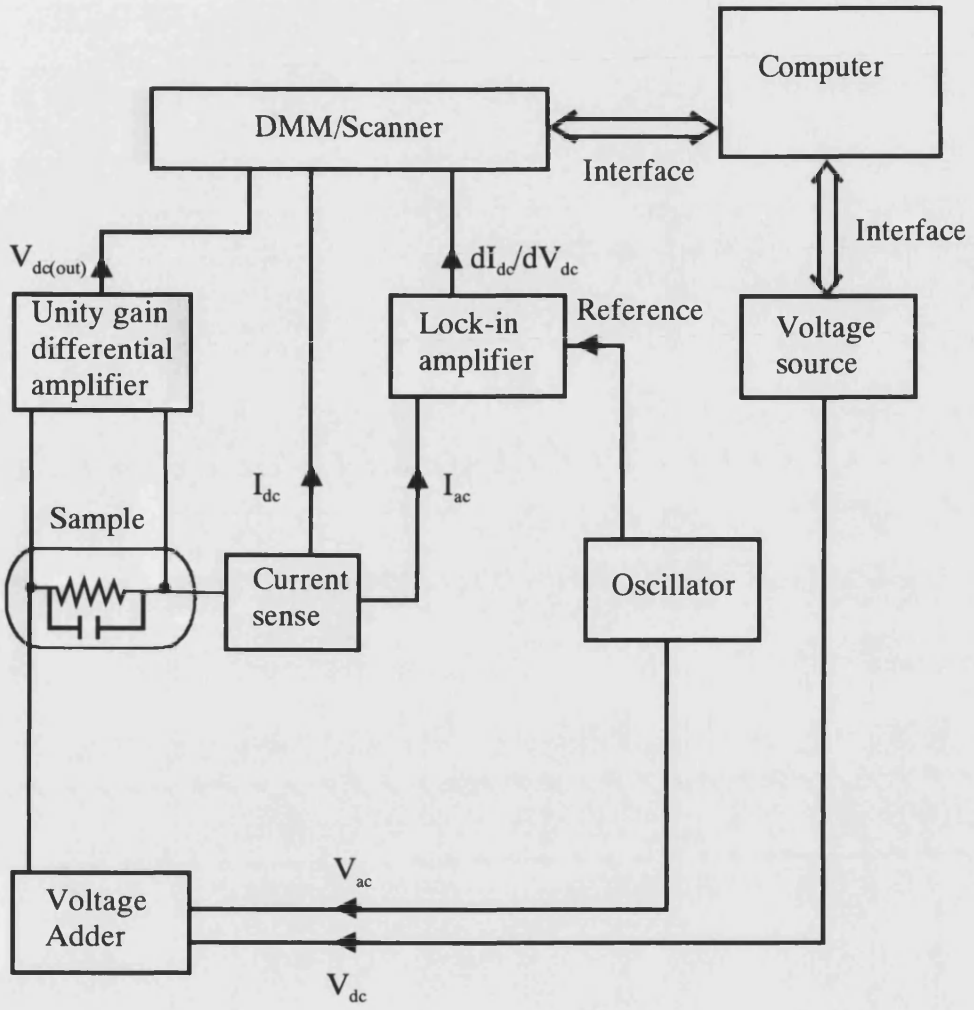

Fig. 5.13 Experimental set-up for current-voltage and conductance-voltage measurements.

In order to perform first (dI/dV) and second derivative (d^2I/dV^2) measurements an ac modulation voltage is added to the dc voltage using a voltage adder circuit (Fig. 5.14) and their sum is applied across the terminals. The dc bias is supplied using a programmable voltage source and the ac signal using an ultra-low distortion oscillator. For the conductance measurements a 1mV rms ac signal of frequency 365 Hz was added to the dc bias, while for second derivative measurements the rms value of ac signal was increased to 10mV.

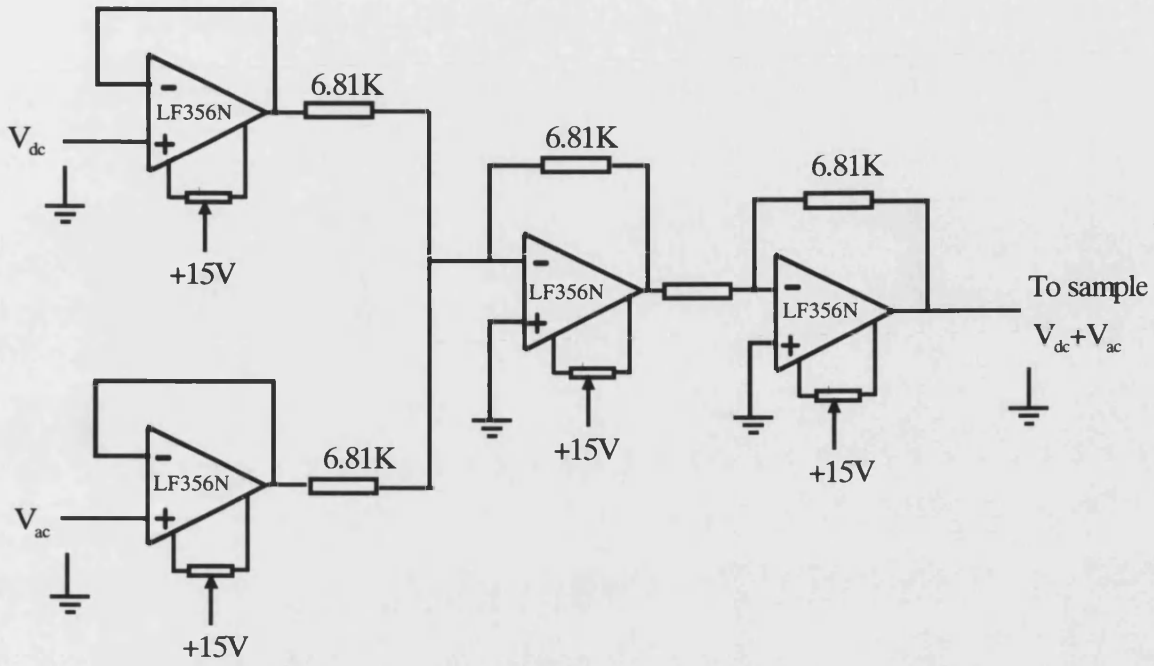

Fig. 5.14 Circuit diagram for the voltage adder.

The dc voltage across the sample is measured using a unity gain differential amplifier (Fig. 5.15) whose output is fed into a Keithly DMM/Scanner. The dc and ac components of current flowing through the device were separated using a current sense circuit (Fig. 5.16) whose dc output is fed into the DMM/Scanner and ac output into a lock-in amplifier. The analogue output of the lock-in is proportional to (dI/dV) and is fed into a second channel of the DMM/Scanner. The current and conductance are measured as a function of a sweep bias and recorded by a computer.

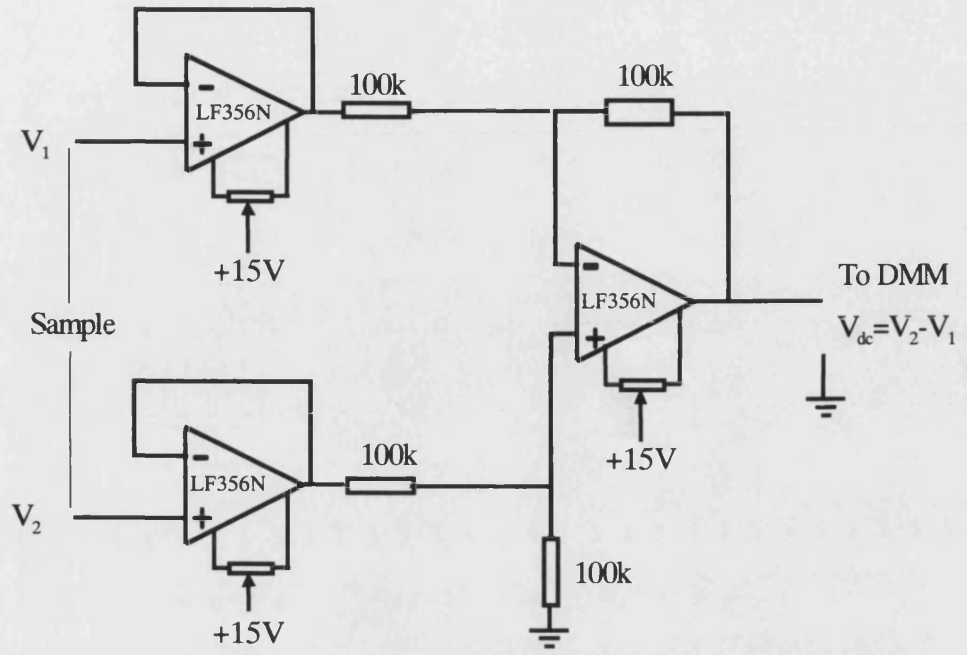

Fig. 5.15 Circuit diagram for the unity gain differential amplifier.

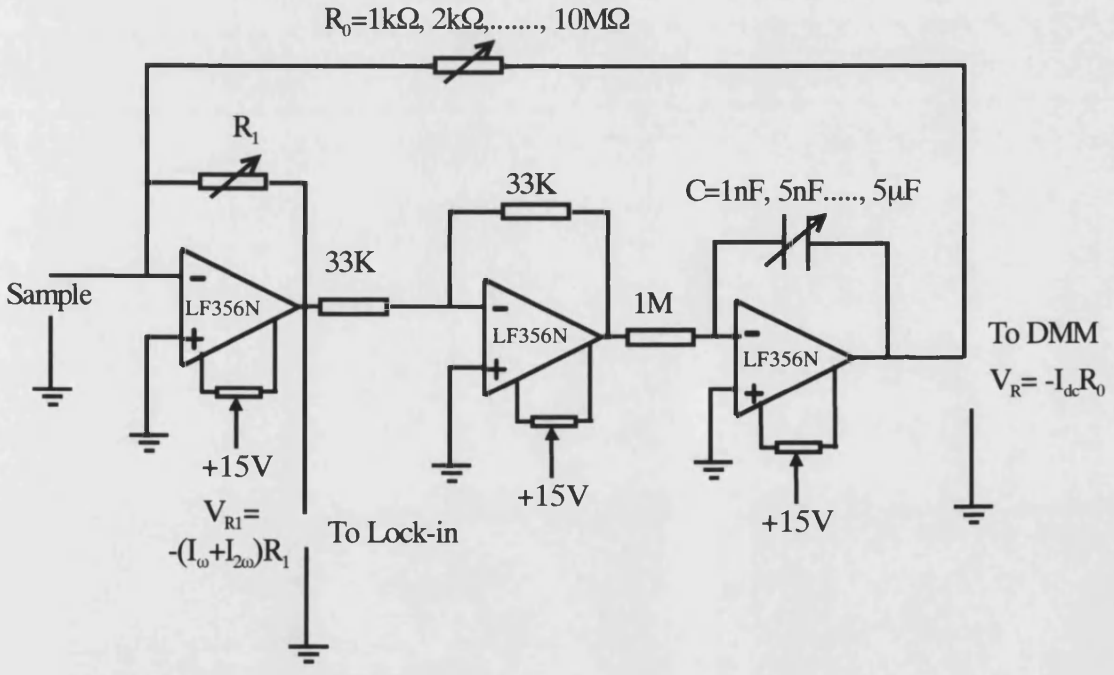

Fig. 5.16 Circuit diagram of the current sense module.

5.7.2 Collector current-voltage and transconductance-voltage measurements

Typical current–voltage and transconductance-voltage characteristics of transistors are measured in both common-base (Fig. 5.17a) and common-emitter (Fig. 5.17b) configurations.

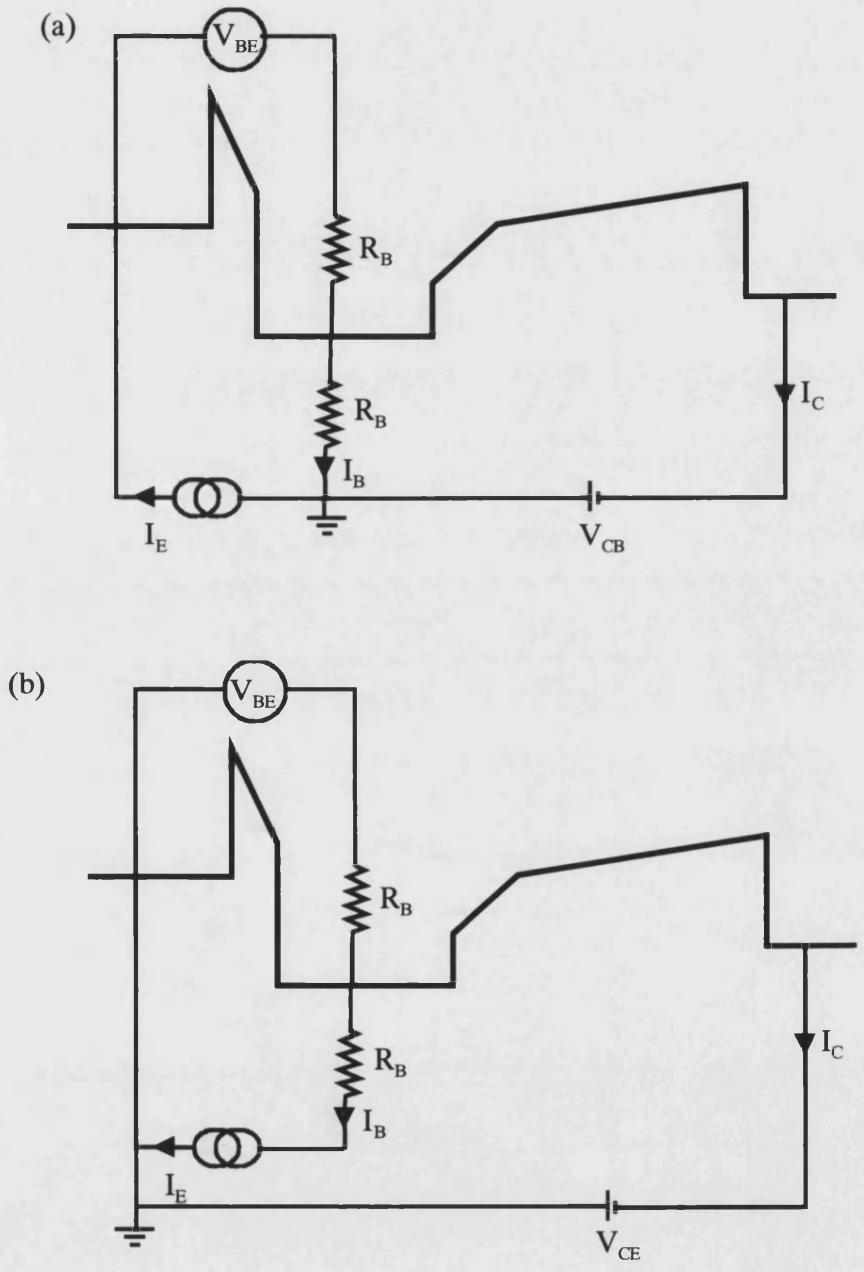

Fig. 5.17 Schematic of (a) common-base and (b) common-emitter measurement configurations. For clarity the details of measurement circuits and ac voltages have not been indicated in the diagram.

The emitter-base bias current is supplied using a programmable current source and the actual voltage drop across the barrier is monitored using a sensitive digital nano-voltmeter in a three-point geometry making use of the second base contact. Using the measurement system described in the previous section collector current and transconductance (dI_C/dV_{CB} or dI_C/dV_{CE}) measurements are recorded as a function of collector bias (V_{CB} or V_{CE}).

The three-point measurement technique is used to eliminate the influence of a series base resistance on the current-voltage and transconductance-voltage data measured in the common-base configuration. The voltage drop across the series base resistance was measured as a function of collector-base bias using the second base contact (Fig. 5.18) and subsequently subtracted from the corresponding two-point common-base data (Appendix C).

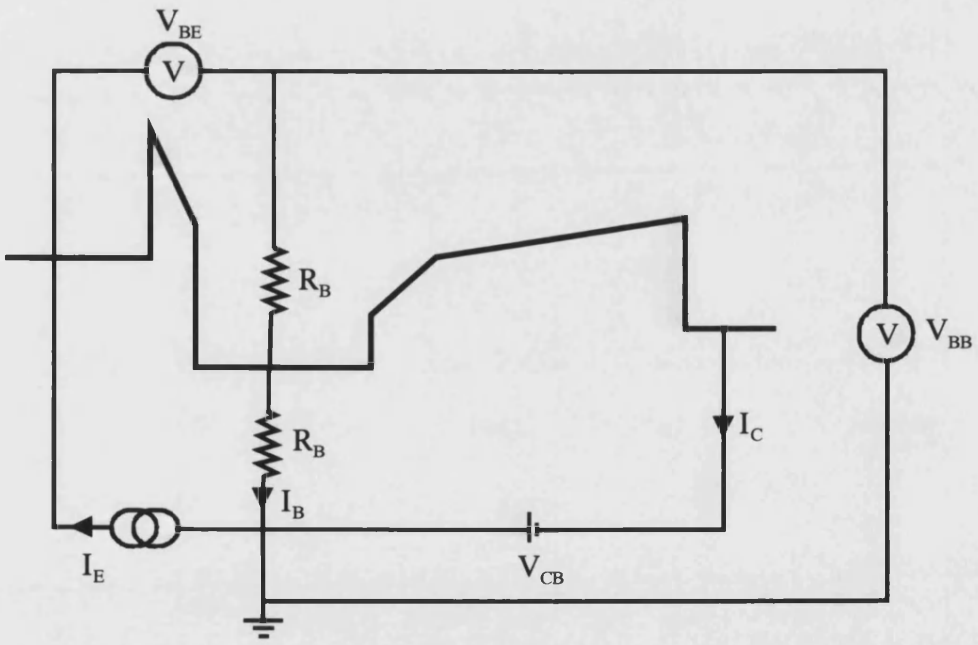

Fig. 5.18 Schematic of three-point measurement method used for eliminating base contact resistances.

5.7.3 Emitter current and emitter barrier conductance measurements

Current passing through emitter barrier and its total conductance as a function of emitter-base bias voltage are measured leaving the collector contact to float (Fig. 5.19). The emitter current is driven through the first base contact and the true voltage between emitter and base contact was measured at the second base contact.

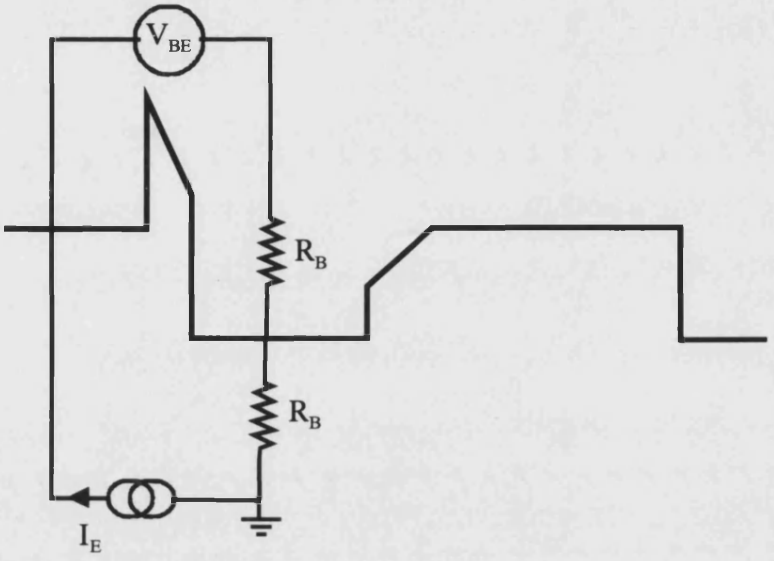

Fig. 5.19 Three-point emitter current-voltage and conductance-voltage measurement configuration.

The circuit used to the measure emitter barrier current-voltage and conductance-voltage is shown in Fig 5.20.

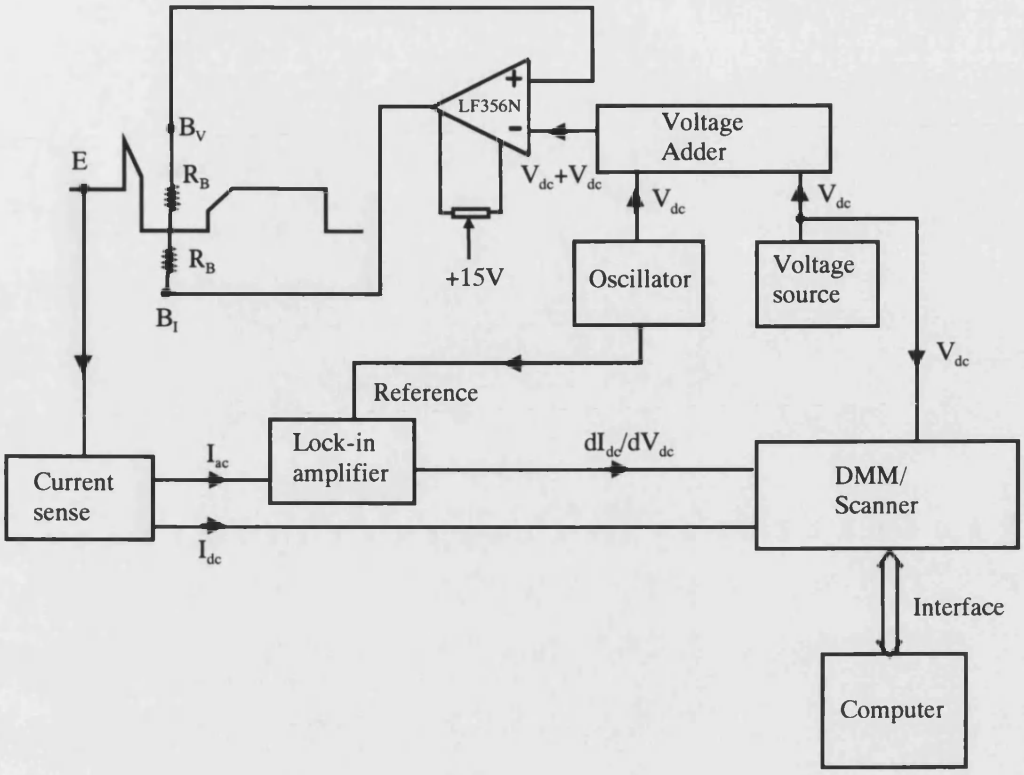

Fig. 5.20 Block diagram of three-point emitter current-voltage and total conductance-voltage measurement set-up.

5.8 Ambient pressure measurements

Samples were mounted on the cold head of a Cryophysics closed cycle refrigeration system using "GE" varnish that provides a good thermal contact between the cold head and the sample. To obtain thermal isolation between the cold head and its surroundings the cryostat was pumped down to 2×10^{-4} mbar. The temperature was measured by a Lakeshore DRC 91CA temperature controller using a silicon diode as a sensor.

5.9 Hydrostatic pressure measurement

Hydrostatic pressure was applied using a Unipress self-clamping pressure cell with a 1:1 mixture of petroleum ether and transformer oil as the pressure transmitting medium. A manganin wire gauge calibrated against an InSb sensor was used to monitor the pressure (Othamann 1995). The pressure at temperature T was determined to be given by the following equation (Bundy 1961).

$$p(T) = \frac{R(p,T) - R(0,T)}{R(0,300).k_0(T)} \qquad (5.9.1)$$

where $R(p,T)$ is the resistance of the manganin gauge at temperature T and pressure p, $R(0,T)$ is the resistance at temperature T and atmospheric pressure, $R(0,300)$ is the resistance at room temperature and atmospheric pressure, and $k_0(T)$ is the pressure coefficient of the manganin gauge at temperature T.

In order to minimise hysteretic effects in the manganin gauge it was heat treated at 140°C for 48 hours and quenched in liquid nitrogen for two hours. The heat-treated manganin gauge was then pressure cycled three times before use. Four-wire measurements of resistance were performed to eliminate the resistance of the leads. We used a pressure coefficient of $(2.45 \pm 0.02) \times 10^{-3}\text{kbar}^{-1}$ at 300K and $(1.98 \pm 0.02) \times 10^{-3}\text{kbar}^{-1}$ at 77K (Othamann 1995).

Hydrostatic pressure was applied at room temperature by compressing the liquid with a hydraulic press. The cell was then slowly cooled down to 77K or 4.2K in a conventional glass cryostat to avoid non-hydrostatic strain and additional stress in the cell (Ermets 1996). The pressure in the cell decreases when it is cooled down (Thompson 1984) due to the contraction of the pressure transmitting liquid. Fig. 5.19 shows a plot of pressure at 77K versus room temperature pressure.

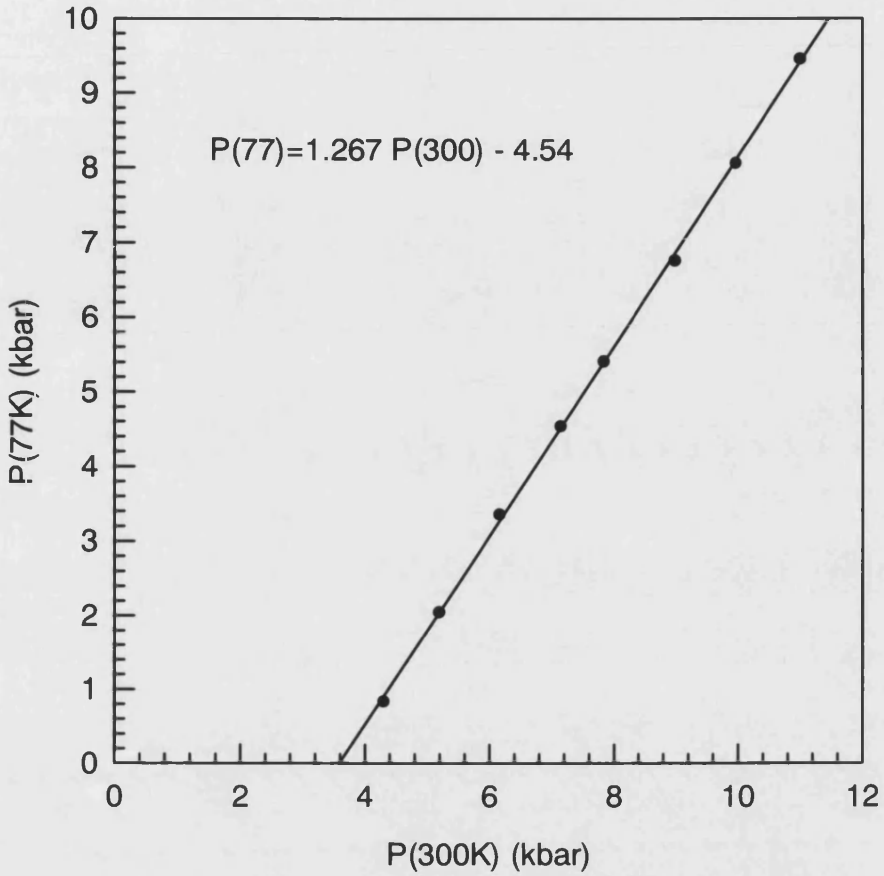

Fig. 5.21 Pressure at 77K as a function of the corresponding room temperature pressure.

The pressure at 77K can be written as $P_{77} \cong 1.267P_{300} - 4.54$, where P_{77} is the pressure at 77K measured in kbar, and P_{300} is the pressure at room temperature measured in kbar.

In the hydrostatic pressure cell samples were again mounted on a holder using "GE" varnish. The "GE" varnish was allowed to dry for several days in order to prevent it from softening when in contact with the pressure transmitting fluids. The temperature inside the pressure cell was monitored using a copper-constantan thermocouple. Fig. 5.18 shows a detailed sketch of the pressure cell.

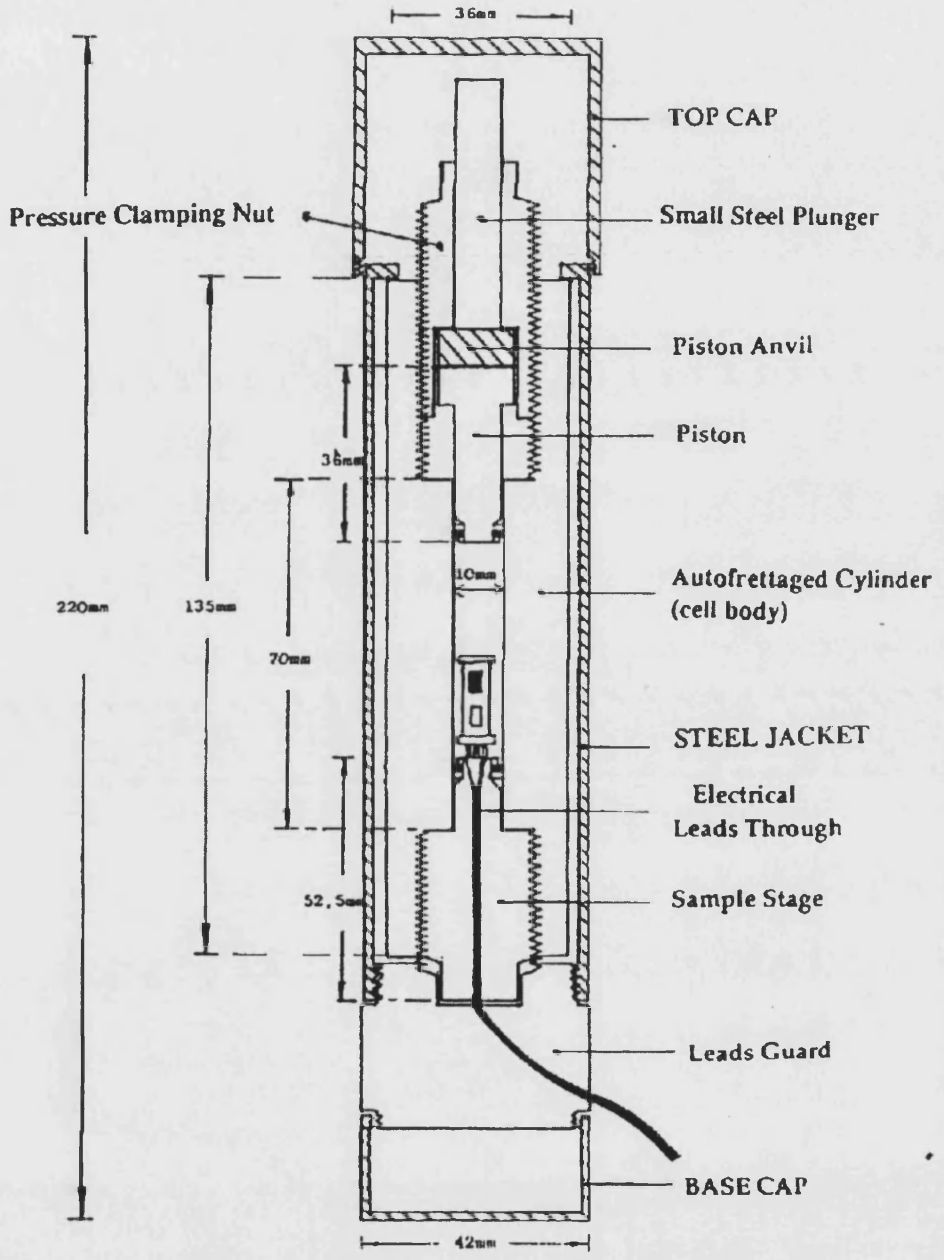

Fig. 5.22 Schematic diagram of Unipress self-clamping hydrostatic pressure cell.

Chapter 6

Modelling of the Tunnelling Hot Electron Transistor

6.1 Introduction

In this chapter a model of a tunnelling hot electron transistor structure will be presented. To simplify an otherwise complicated problem the effects of band bending at the interfaces are ignored in the simple model to calculate current-voltage characteristics of the transistor. The numerical simulations were performed in a Unix environment using NAG library routines.

The detailed calculations of in plane voltage drop in the base region which may induce inhomogeneous distribution of tunnelling current, band bending at interfaces and a leverage rule for the collector barrier of the transistor are also described. Since the X-point subbands of the AlAs emitter barrier are expected to play a major role in transport through the barrier region, we have also calculated the energies of X-point subbands for the biased structure. The in plane voltage drop, band bending and X-point subbands calculations were performed with the 'Mathcad' software package (Appendix B).

6.2 Transmission coefficient

The transmission probability for the emitter barrier or collector barrier can be evaluated using equation (3.3.37) derived in section 3.3 of chapter 3.

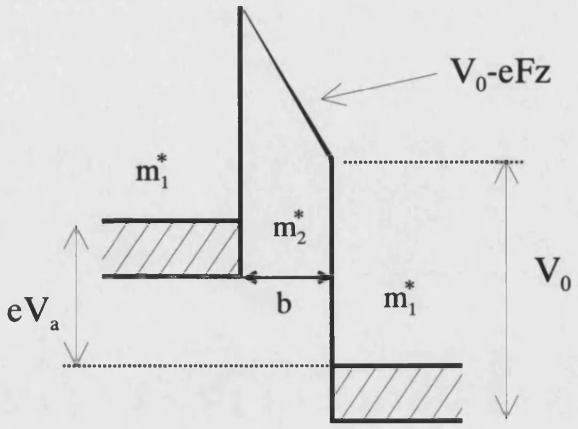

Fig. 6.1 A schematic of a single barrier structure under an applied bias of V_a (V). The barrier width is b, barrier height V_0 (eV) and the effective mass of the electrons in the electrodes and the barrier regions are taken to be m_1^* and m_2^* respectively.

For the biased emitter barrier (Fig. 6.1) the transmission probability is given by,

$$t_1 = \frac{4k_2/k_1}{\left(u_{11} + \frac{k_1}{k_2}u_{22}\right)^2 + \left(\frac{1}{k_2}u_{21} - k_1 u_{12}\right)^2} \tag{6.2.1}$$

where

$$k_1 = \sqrt{\frac{2m_1^* E}{\hbar^2}} \tag{6.2.2}$$

$$k_2 = \sqrt{\frac{2m_1^*(E + eV_a)}{\hbar^2}} \tag{6.2.3}$$

and u_{ij}'s are the elements of matrix U.

The matrix U can be shown to be,

$$U = \begin{pmatrix} Ai(z=0) & Bi(z=0) \\ \lambda_1 \frac{m_1^*}{m_2^*} Ai'(z=0) & \lambda_1 \frac{m_1^*}{m_2^*} Bi'(z=0) \end{pmatrix} \times \begin{pmatrix} Ai(z=b) & Bi(z=b) \\ \lambda_2 \frac{m_1^*}{m_2^*} Ai'(z=b) & \lambda_2 \frac{m_1^*}{m_2^*} Bi'(z=b) \end{pmatrix}^{-1} \quad (6.2.4)$$

The argument of the Airy function is given by,

$$\rho = \left(\frac{2m_2^* eF}{\hbar^2}\right)^{1/3} \left\{\frac{V_0 - E}{eF} - z\right\} \quad (6.2.5)$$

The result of the numerical simulation for the emitter barrier transmission coefficient as a function of energy of the incident electron is shown below.

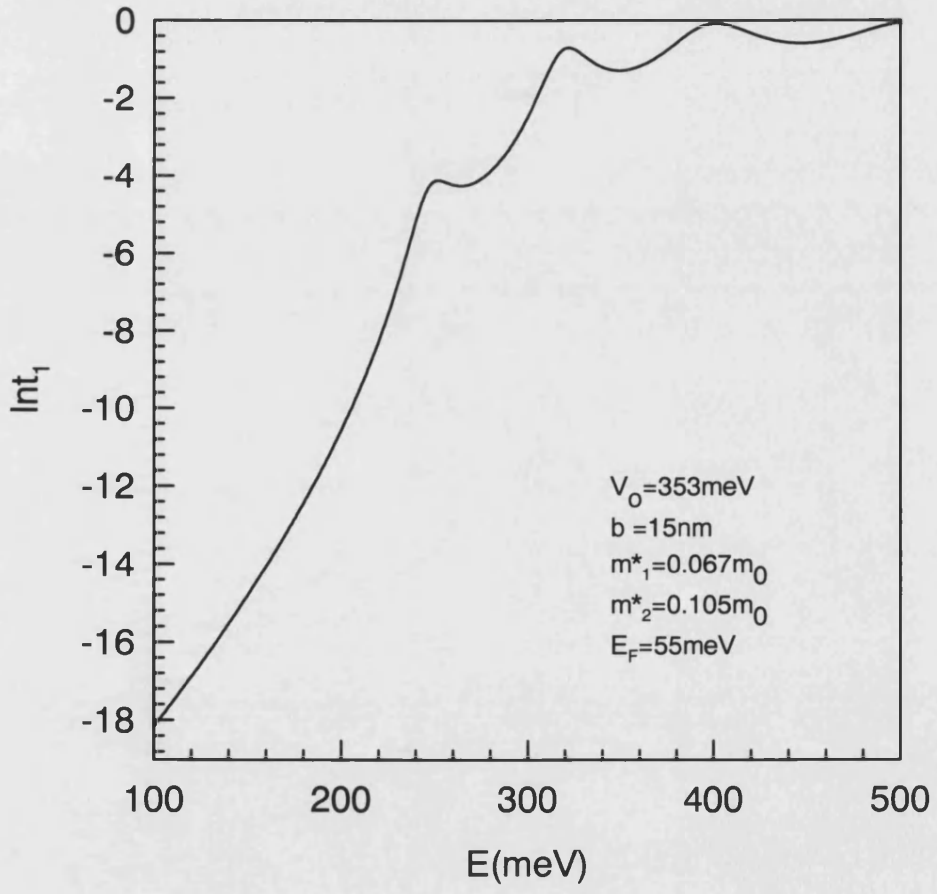

Fig. 6.2 Tunnelling probability through an $Al_{0.5}Ga_{0.5}As$ emitter barrier under an applied bias of 200mV.

Now we consider the collector barrier,

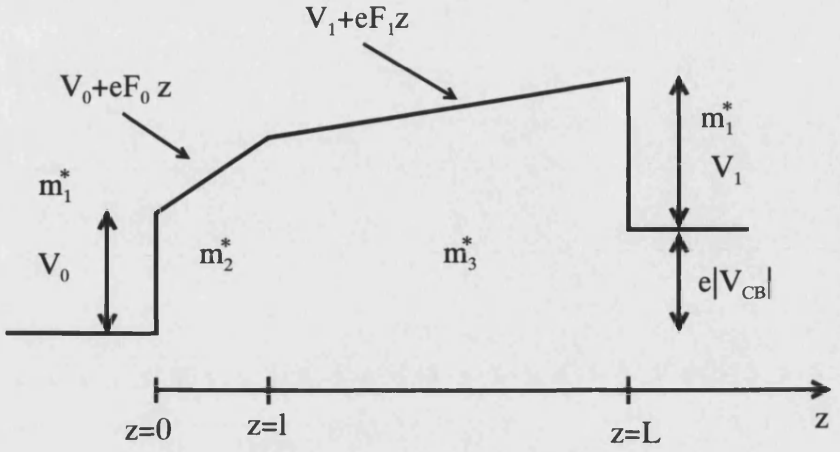

Fig. 6.3 A sketch of graded collector barrier under reverse bias.

Ignoring the band bending at the interfaces the potential energy in the flat and graded regions of the collector barrier can be written as,

$$V(z) = 0 \quad z < 0 \tag{6.2.6}$$

$$= V_0 \pm eF_0 z \quad 0 \le z \le l \tag{6.2.7}$$

$$= V_1 \pm eF_1 z \quad l \le z \le L \tag{6.2.8}$$

$$= e|V_{CB}| \quad z \ge L \tag{6.2.9}$$

where $eF_1 = \dfrac{e|V_{CB}|}{L}$ (6.2.10)

$$eF_0 = \frac{e|V_{CB}|}{L} \pm \frac{V_1 - V_0}{l} \tag{6.2.11}$$

the + (-) sign refers to reverse (forward) biased collector barrier.

The transmission probability is given by,

$$t_2 = \frac{4k_2/k_1}{\left(u_{11} + \frac{k_1}{k_2}u_{22}\right)^2 + \left(\frac{1}{k_2}u_{21} - k_1 u_{12}\right)^2} \tag{6.2.12}$$

where

$$k_1 = \sqrt{\frac{2m_1^* E}{\hbar^2}} \tag{6.2.13}$$

$$k_2 = \sqrt{\frac{2m_1^*(E \pm e|V_{CB}|)}{\hbar^2}} \tag{6.2.14}$$

the + (-) sign refers to forward (reverse) biased collector barrier.

It can be easily shown that for the collector barrier the matrix U can be written as,

$$U = \begin{pmatrix} Ai(z=0) & Bi(z=0) \\ \lambda_1 \frac{m_1^*}{m_2^*} Ai'(z=0) & \lambda_1 \frac{m_1^*}{m_2^*} Bi'(z=0) \end{pmatrix} \times \begin{pmatrix} Ai(z=l) & Bi(z=l) \\ \lambda_1 Ai'(z=l) & \lambda_1 Bi'(z=l) \end{pmatrix}^{-1}$$

$$\times \begin{pmatrix} Ai(z=0) & Bi(z=0) \\ \lambda_2 \frac{m_2^*}{m_3^*} Ai'(z=0) & \lambda_2 \frac{m_2^*}{m_3^*} Bi'(z=0) \end{pmatrix} \times \begin{pmatrix} Ai(z=L-l) & Bi(z=L-l) \\ \lambda_2 \frac{m_1^*}{m_3^*} Ai'(z=L-l) & \lambda_2 \frac{m_1^*}{m_3^*} Bi'(z=L-l) \end{pmatrix}^{-1} \tag{6.2.15}$$

where $\lambda_1 = \pm\left(\frac{2m_2^* eF_0}{\hbar^2}\right)^{1/3}$ (6.2.16)

$$\lambda_2 = \pm\left(\frac{2m_3^* eF_1}{\hbar^2}\right)^{1/3} \tag{6.2.17}$$

the + (-) sign refers to a reverse (forward) biased collector barrier.

The argument of Airy functions is given by

$$\rho = \left(\frac{2m_2^* eF}{\hbar^2}\right)^{1/3} \left\{\frac{V_0 - E}{eF_0} \pm z\right\} \qquad 0 \le z \le l \qquad (6.2.18)$$

$$\left(\frac{2m_2^* eF}{\hbar^2}\right)^{1/3} \left\{\frac{V_1 \pm eF_1 l - E}{eF_1} \pm z\right\} \qquad l \le z \le L \qquad (6.2.19)$$

where the + (-) sign refers to a reverse (forward) biased collector barrier.

Note that the position variable z is mapped back to zero at the interfaces for simplicity. The collector transmission coefficient as a function of collector-base bias voltage can be computed by substituting the appropriate u_{ij}'s into the equation. The results of the simulations are given below.

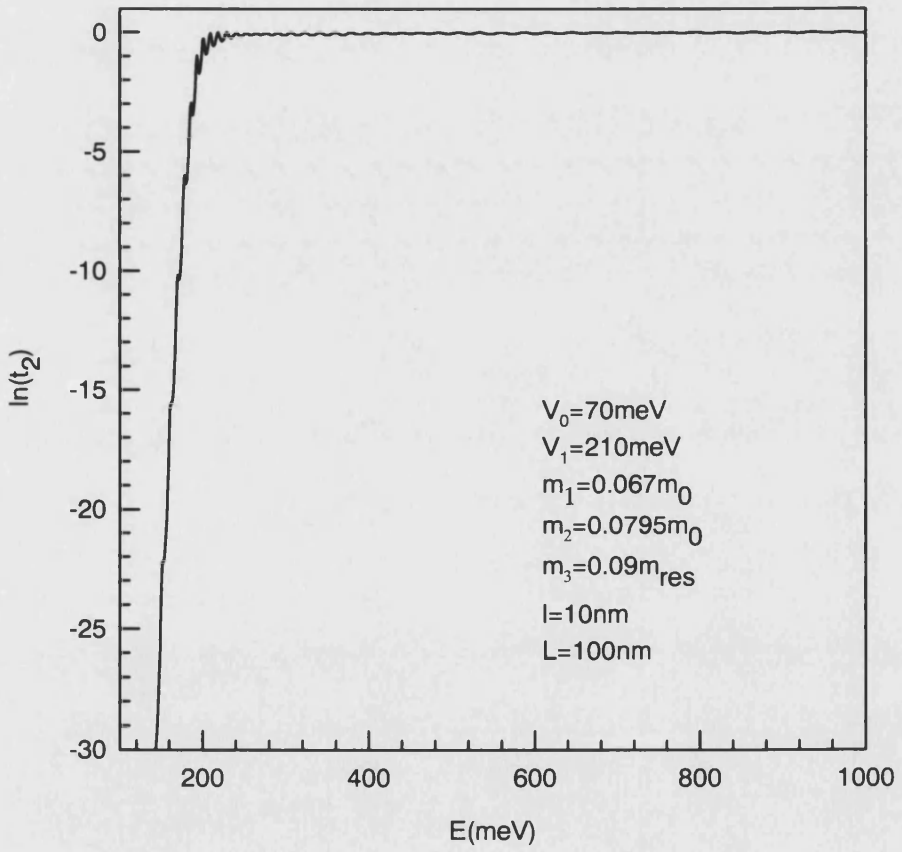

Fig. 6.4 Transmission probability through a graded collector barrier as in Fig. 6.3 under a forward bias of 100mV.

6.3 Tunnelling current

The current through the emitter barrier can be easily calculated using the equation (3.2.15) derived in chapter 3.

$$J = \int dE_z N(E_z) D(E_z, V) \tag{6.3.1}$$

$$\text{where } N(E_z) = \frac{m^* e k_B T}{2\pi^2 \hbar^3} \ln\left\{\frac{1+\exp[(E_F - E_z)/k_B T]}{1+\exp[(E_F - E_z - eV)/k_B T]}\right\} \tag{6.3.2}$$

In practice the experiments are carried out at low temperature, so we can assume the temperature to be 0K. The expression for the current density at 0K can be written as (Tsu and Esaki 1973),

$$J = \frac{m^* e}{2\pi^2 \hbar^3}\left[eV\int_0^{E_F - eV} dE_z D(E_z, V) + \int_{E_F - eV}^{E_F} dE_z (E_F - E_z) D(E_z, V)\right] \qquad eV_{BE} \le E_F \tag{6.3.3}$$

$$J = \frac{m^* e}{2\pi^2 \hbar^3}\int_0^{E_F} dE_z (E_F - E_z) D(E_z, V_{BE}) \qquad eV_{BE} \ge E_F \tag{6.3.4}$$

The results of the simulation for the $Al_{0.5}Ga_{0.5}As$ barrier is shown in Fig. 6.5.

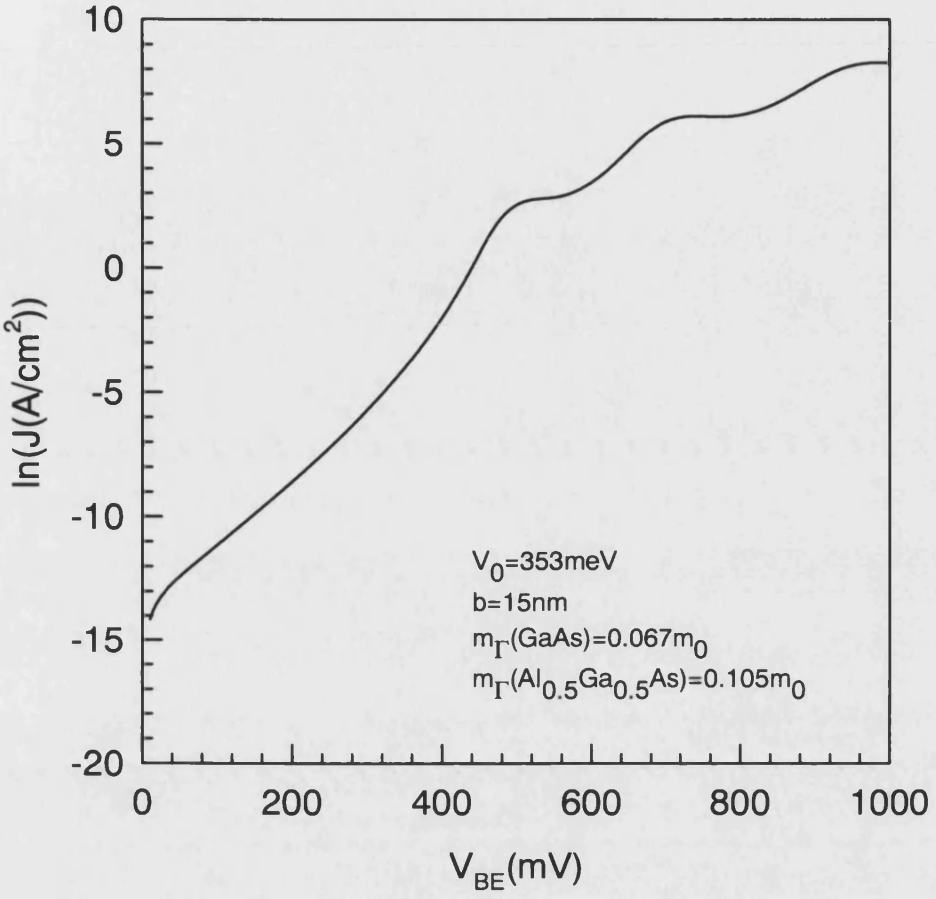

Fig. 6.5 Tunnelling current density through an $Al_{0.5}Ga_{0.5}As$ emitter barrier as a function of applied bias.

6.4 Collector current

The common-base current-voltage characteristics have been calculated by mapping the emitter current distribution onto the collector barrier assuming that the quantum phase information is lost across the base layer.

$$I_E(V_{BE}) = \frac{Ame}{2\pi^2\hbar^3}\int_0^{E_F} dE_z(E_F - E_z)D_E(E_z, V_{BE}) \qquad (6.4.1)$$

where A is the area of the device.

Using the above relationship current flowing close to energy E_z can be written as,

$$\bar{I}_E(V_{BE}) = k(V_{BE})(E_F - E_z)D_E(E_z, V_{BE}) \qquad (6.4.2)$$

The constant $k(V_{BE})$ can be evaluated using the following identity.

$$\int_0^{E_F} \bar{I}_E(V_{BE})dE_z = I_E(V_{BE}) \qquad (6.4.3)$$

To calculate the collector current $\bar{I}_E(V_{BE})$ is mapped onto the collector barrier transmission coefficient and integrated from 0 to E_F.

$$I_C(V_{BE}, V_{CB}) = \int_0^{E_F} k(V_{BE})(E_F - E_z)D(E_z, V_{BE})D_C(E_z + eV_{BE}, V_{CB})dE_z \qquad (6.4.4)$$

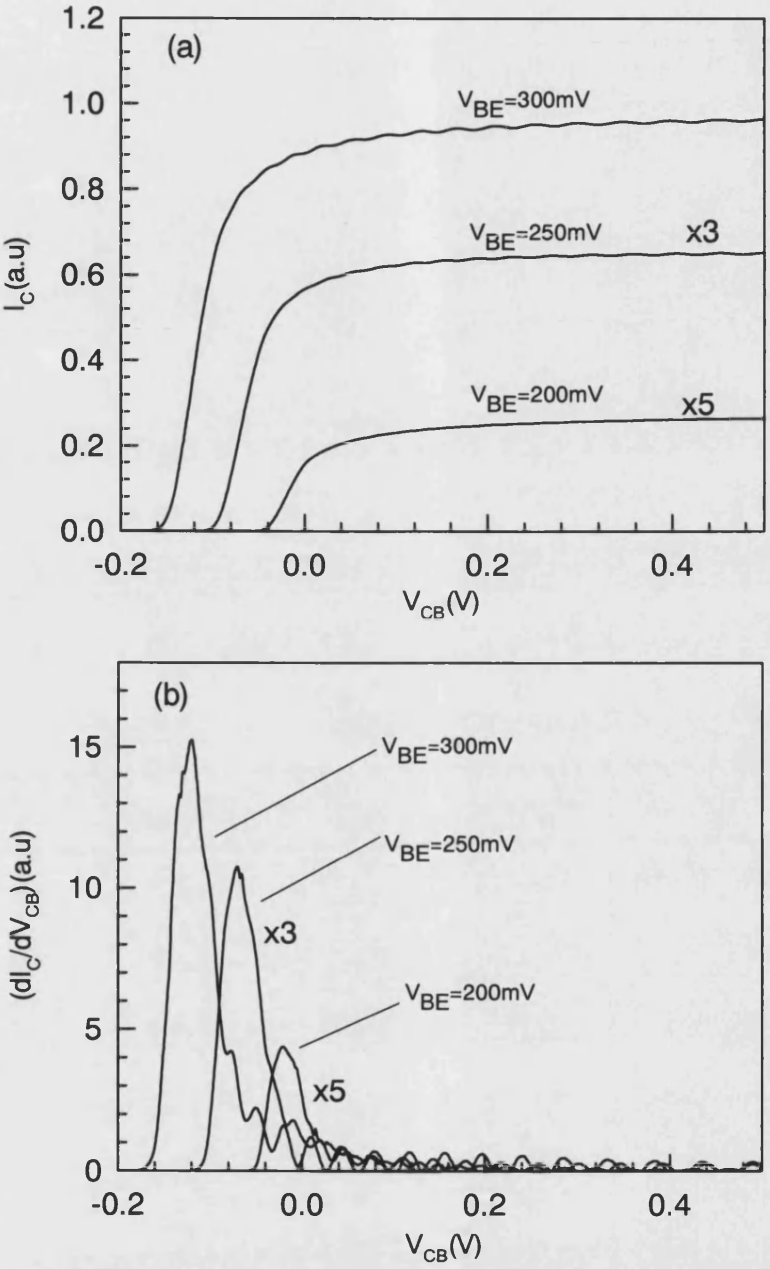

Fig. 6.6 (a) Plot of calculated collector current as a function of collector-base bias and (b) derivative of collector current with respect to collector-base voltage.

6.5 Effect of band bending at the interfaces

Application of a negative bias to the emitter electrode effectively draws negative charge to the interface causing the conduction band to bend downwards. In response to this an equal amount of positive charge accumulates at the interface on the base side. The positive charge at the interface arises from depletion of electrons near the interface leaving behind uncompensated ionised donors. The total applied voltage is the sum of the voltage drops across the accumulation region, depletion region and the barrier.

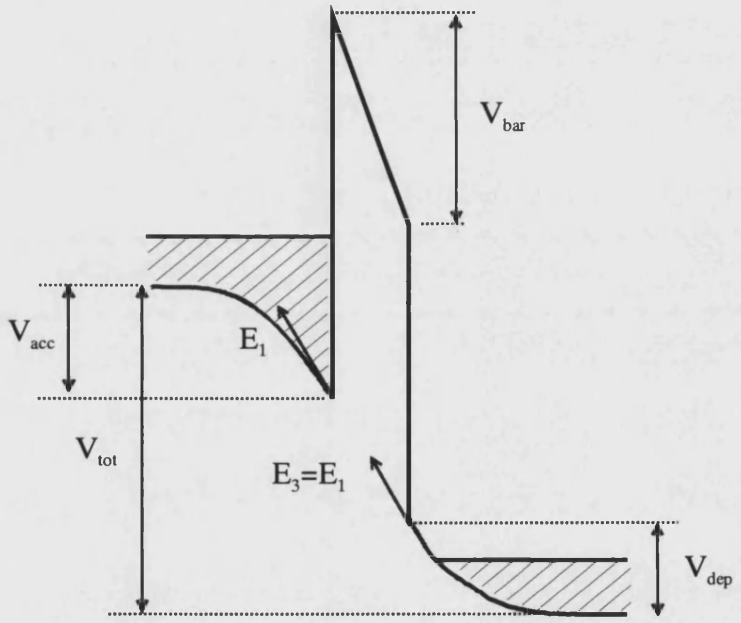

Fig. 6.7 A single barrier structure under an applied bias with band bending at the interfaces included.

We calculate the voltage drop across the accumulation and depletion regions using the classical Poisson equation and neglecting quantum effects (Bonnefoi *et al.* 1987).

Assuming a linear relationship between the electric displacement vector D(r) and the static electric field E, Poisson's equation in one dimension becomes,

$$\frac{dE}{dz} = \frac{\rho(z)}{\varepsilon} \tag{6.5.1}$$

where E is the static electric field, ε is the dielectric constant of the material and $\rho(z)$ is the charge density.

In terms of the conduction band edge energy Poisson's equation can be expressed as,

$$\frac{d^2\phi}{dz^2} = -\frac{dE}{dz} = -\frac{\rho(z)}{\varepsilon} \tag{6.5.2}$$

For a degenerately doped n-type semiconductor the charge density can be expressed as,

$$\rho(z) = -e(n(\phi) - N_D) \tag{6.5.3}$$

where n is the electron density in the conduction band and N_D is the density of ionised donors.

Assuming the temperature to be 0 K, the electron density for a given filling of a 3D band of a degenerately doped n-type semiconductor is given by,

$$n = \frac{1}{3\pi^2}\left(\frac{2m^*}{\hbar^2}\right)^{3/2}(E_F + e\phi)^{3/2}, \quad E_F \geq -e\phi \tag{6.5.4}$$

where m^* is the density-of-states effective mass for electrons in the conduction band, and $-e\phi$ is the energy of the conduction band edge.

Charge neutrality at $\phi = 0$ requires,

$$N_D = \frac{1}{3\pi^2}\left(\frac{2m^*}{\hbar^2}\right)^{3/2} E_F{}^{3/2} \tag{6.5.5}$$

Substituting n and N_D into 6.5.2, we obtain,

$$\frac{d^2\phi}{dz^2} = \frac{e}{3\pi^2\varepsilon_1}\left(\frac{2m^*}{\hbar^2}\right)^{3/2}\left[(E_F + e\phi)^{3/2} - E_F^{3/2}\right] \qquad (6.5.6)$$

multiplying both sides of the equation (6.5.6) by $\frac{d\phi}{dz}$ we get,

$$\left(\frac{d\phi}{dz}\right)\times\left(\frac{d^2\phi}{dz^2}\right) = \frac{e}{3\pi^2\varepsilon_1}\left(\frac{2m^*}{\hbar^2}\right)^{3/2}\left[(E_F + e\phi)^{3/2} - E_F^{3/2}\right]\times\left(\frac{d\phi}{dz}\right) \qquad (6.5.7)$$

Writing the left side of this equation in terms of the electric field $E = -\frac{d\phi}{dz}$,

$$\frac{d}{dz}\left(\frac{1}{2}(-E)^2\right) = \frac{1}{3\pi^2\varepsilon_1}\left(\frac{2m^*}{\hbar^2}\right)^{3/2}\frac{d}{dz}\left[\frac{2}{5}(E_F + e\phi)^{5/2} - E_F^{3/2}e\phi\right] \qquad (6.5.8)$$

First we consider the accumulation region (Fig. 6.7)

Integrating the equation 6.5.8 from the bulk towards the interface

$$\int_o^{E_1} d\left(\frac{1}{2}(-E)^2\right) = \frac{1}{3\pi^2\varepsilon_1}\left(\frac{2m^*}{\hbar^2}\right)^{3/2}\int_0^{V_{acc}} d\left[\frac{2}{5}(E_F + e\phi)^{5/2} - E_F^{3/2}e\phi\right] \qquad (6.5.9)$$

$$E_1^2 = \frac{2}{3\pi^2\varepsilon_1}\left(\frac{2m^*}{\hbar^2}\right)^{3/2}\left[\frac{2}{5}(E_F + eV_{acc})^{5/2} - E_F^{3/2}eV_{acc} - \frac{2}{5}E_F^{5/2}\right] \qquad (6.5.10)$$

This gives a simple relationship between the electric field at the interface (E_1) and the voltage drop across the accumulation region (V_{acc}).

Assuming there is no charge localised at the interface we can write,

$$\varepsilon_1 E_1 = \varepsilon_2 E_2 \qquad (6.5.11)$$

where E_2 is the electric field in the barrier region and ε_1 and ε_2 are the dielectric constant of the electrodes and barrier region respectively.

From this the voltage drop across the barrier can be written as,

$$V_{barr} = E_2 \times b = \frac{\varepsilon_1}{\varepsilon_2} E_1 \times b \qquad (6.5.12)$$

where b is the width of the barrier.

The voltage drop across the depletion region can be related to E_1 by integrating the equation 6.5.8 assuming $E_3 = E_1$ where E_3 is the electric field at the interface (Fig.6.7).

If $eV_{dep} < E_F$ the integral becomes,

$$\int_o^{-E_1} d\left(\frac{1}{2}(-E)^2\right) = \frac{1}{3\pi^2\varepsilon_1}\left(\frac{2m^*}{\hbar^2}\right)^{3/2} \int_0^{-V_{dep}} d\left[\frac{2}{5}(E_F + e\phi)^{5/2} - E_F^{3/2} e\phi\right] \qquad (6.5.13)$$

$$E_1^2 = \frac{2}{3\pi^2\varepsilon_1}\left(\frac{2m^*}{\hbar^2}\right)^{3/2}\left[\frac{2}{5}(E_F - eV_{dep})^{5/2} + E_F^{3/2} eV_{dep} - \frac{2}{5}E_F^{5/2}\right] \qquad (6.5.14)$$

If $eV_{dep} > E_F$ the solution to the Poisson equation has two parts. This situation is illustrated in Fig. 6.8.

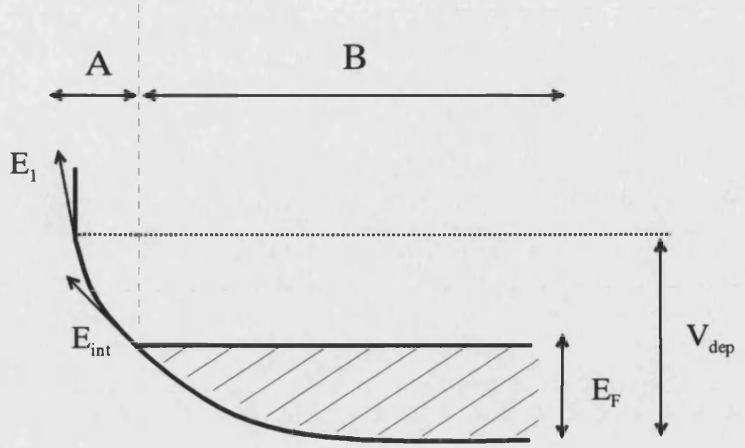

Fig. 6.8 A sketch of energy-band diagram illustrating band bending due to the depletion of carriers. In the region A (B) carriers are fully (partially) depleted.

Since carriers are fully depleted in region A the Poisson's equation becomes,

$$\frac{d^2\phi}{dz^2} = -\frac{eN_D}{\varepsilon_1} \qquad (6.5.15)$$

Multiplying both sides of this equation by $\frac{d\phi}{dz}$ and integrating towards the interface we get,

$$E_1^2 - E_{\text{int}}^2 = -\frac{2n_D}{\varepsilon_1}(-eV_{dep} + E_F) \qquad (6.5.16)$$

where E_{int} is the electric field at the interface between fully depleted (region A) and partially depleted (region B) region.

Integrating equation 6.5.8 we obtain a simple relation for E_{int} in terms of the Fermi Energy E_F and the other bulk parameters.

$$\int_{o}^{-E_{int}} d\left(\frac{1}{2}(-E)^2\right) = \frac{1}{3\pi^2\varepsilon_1}\left(\frac{2m^*}{\hbar^2}\right)^{3/2} \int_{0}^{-E_F/e} d\left[\frac{2}{5}(E_F + e\phi)^{5/2} - E_F^{3/2} e\phi\right]$$

(6.5.17)

$$E_{int}^2 = \frac{2}{5\pi^2\varepsilon_1}\left(\frac{2m^*}{\hbar^2}\right)^{3/2} E_F^{5/2} \qquad (6.5.18)$$

Substituting equation (6.5.18) into (6.5.16) we obtain a simple relationship between V_{dep} and E_1.

$$V_{dep} = \frac{\varepsilon_1}{2en_D}\left[E_1^2 - \frac{2}{5\pi^2\varepsilon_1}\left(\frac{2m}{\hbar^2}\right)^{3/2} E_F^{5/2}\right] + \frac{E_F}{e} \qquad (6.5.19)$$

By evaluating these equations the voltage drops across the three regions can be calculated. The calculation was performed using 'Mathcad' and the results are plotted in the following graphs.

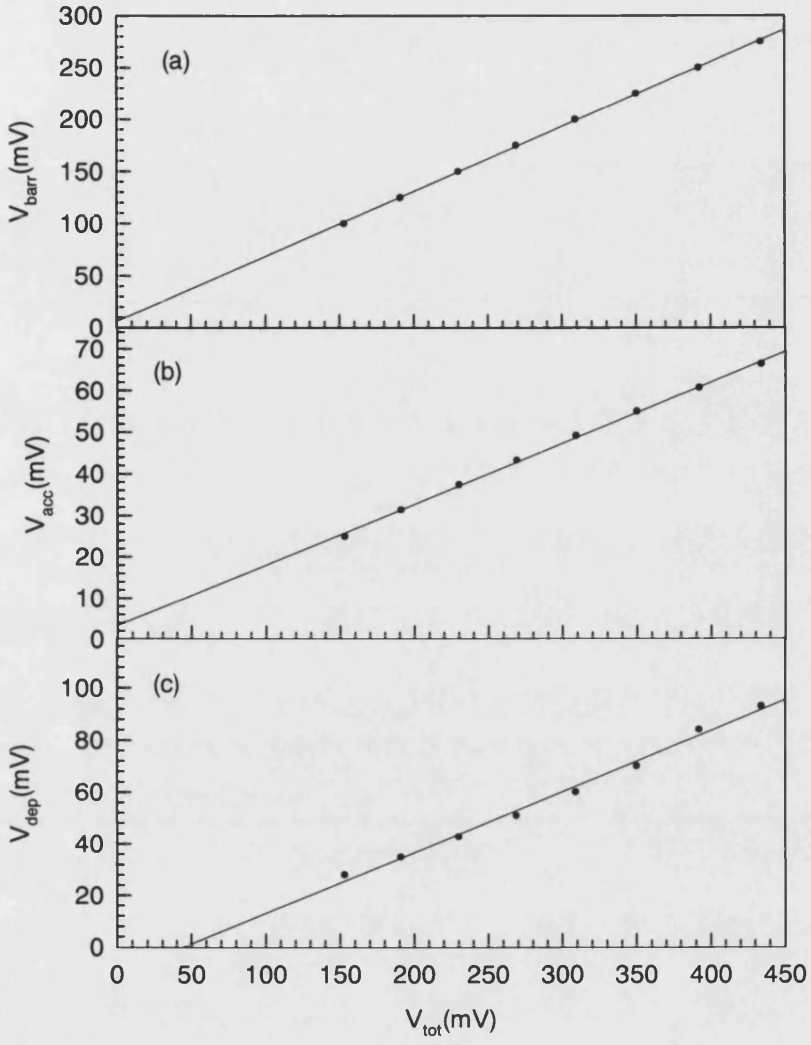

Fig. 6.9 Calculated voltage drop across (a) the barrier (b) the accumulation region and (c) the depletion region plotted as a function of total voltage.

From Fig. 6.9a we estimate that about 62% of the total applied voltage is dropped across the barrier.

6.6 Leverage rule for the collector barrier

Consider a graded collector barrier under forward bias (Fig. 6.10).

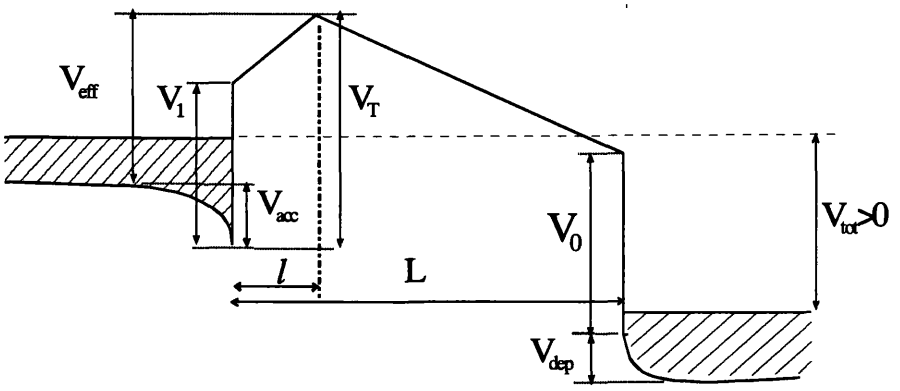

Fig. 6.10 A sketch of graded collector barrier under forward bias.

For the forward biased collector barrier the potential energy of the maximum point of the potential can be written as,

$$V_T = V_0 - V_{barr}\frac{l}{L} \qquad (6.6.1)$$

where V_{barr} is the voltage drop across the collector barrier region.

Taking into account the band bending at the interfaces,

$$V_{barr} = V_{tot} \times f_{barr} \qquad (6.6.2)$$

where f_{barr} is the fraction of applied voltage (V_{tot}) that drops across the collector barrier.

$$V_T = V_0 - V_{tot} \times f_{barr}\frac{l}{L} \qquad (6.6.3)$$

The voltage drop across the accumulation region introduces a small reduction in V_T and the effective barrier height becomes,

$$V_{eff} = V_T - V_{acc} \tag{6.6.4}$$

where V_{acc} is the voltage drop across the accumulation region and can be written as,

$$V_{acc} = V_{tot} \times f_{acc} \tag{6.6.5}$$

where f_{acc} is the fraction of applied voltage that drops across the accumulation region.

The effective barrier height then becomes,

$$V_{eff} = V_0 - V_{tot} \times f_{barr} \frac{l}{L} - V_{tot} \times f_{acc} \tag{6.6.6}$$

$$= V_0 - V_{tot}\left(\frac{l}{L} f_{barr} - f_{acc}\right) \tag{6.6.7}$$

We have solved Poisson's equation to find the voltage drop across the accumulation region and across the barrier. For our 100nm collector barrier we calculate $f_{barr} = 0.926$ and $f_{acc} = 0.035$.

Upon substituting these values in the equation 6.6.7 the effective barrier height becomes,

$$V_{eff} = V_0 - \frac{V_{tot}}{7.7} \tag{6.6.8}$$

Simlarly for the forward biased collector barrier the effective barrier height can be shown to be

$$V_{eff} = V_2 + \frac{|V_{tot}|}{1.04} \tag{6.6.9}$$

6.7 Calculation of in-plane voltage drop in base

Due to currents flowing in the base layer and the associated voltage drop the injected current density does not flow uniformly across the emitter contact. It is important to choose a sufficiently narrow emitter mesa to suppress this effect.

Consider currents in and under the emitter mesa (width w and length l) of a THETA device (Fig. 6.11). Let $J(x)$ be the tunnelling current density in the emitter barrier at x, and $j(x)$ and $j(x+\delta x)$ are the in-plane current density flowing in the base under the emitter mesa at x and $x+\delta x$ respectively. Our aim is to find the voltage drop $V_{B1}-V_{B2}$, where V_{B1} is the measured three-point voltage drop between the base and emitter. If too large this in-plane voltage drop will introduce some artefacts in the experimentally measured current-voltage characteristics of the transistor.

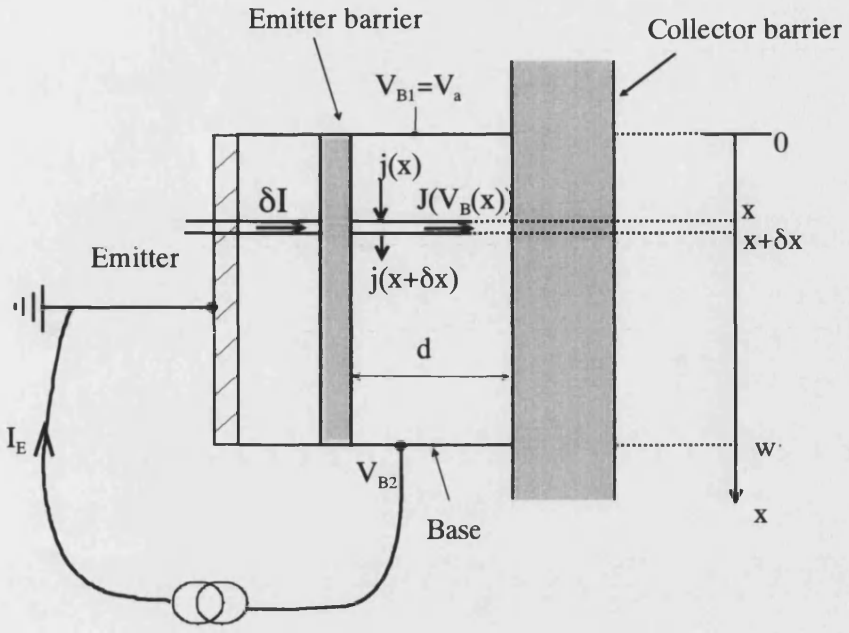

Fig. 6.11 A schematic of current flow into the emitter contact and in-plane current flow in the base region under the emitter mesa.

From conservation of current we have

$$\delta I = l \times \delta x \times J(V_B(x)) \qquad (6.7.1)$$

where $J(V_B(x))$ is the tunnelling current density in the base at x and $V_B(x)$ is the voltage in the base at x.

Current continuity at x gives

$$d \times l \times \left[j(x+\delta x) - j(x) \right] = l \times \delta x \times J(V_B(x)) \qquad (6.7.2)$$

where d is the base layer width and . $j(x)$ is the base current density at x.

This gives following first order differential equation

$$\frac{dj(x)}{dx} = \frac{J(V_B(x))}{d} \qquad (6.7.3)$$

The voltage drop between x and $x+\delta x$ in the base is given by

$$\delta(V_B(x)) = (j(x) \times d \times l) \times \frac{\rho \delta x}{d \times l} \tag{6.7.4}$$

where ρ is the base resistivity.

$$\frac{dV_B(x)}{dx} = j(x)\rho \tag{6.7.5}$$

Substituting this into equation (6.7.3) we get

$$\frac{d^2V_B(x)}{dx^2} = \frac{\rho}{d} J(V_B(x)) \tag{6.7.6}$$

The current density flowing through the barrier can be calculated using the equations 6.3.3 and 6.3.4 given in this chapter.

$$J(V_B(x)) = \frac{me}{2\pi^2\hbar^3}\left[eV\int_0^{E_F-eV} dE_z D(E_z,V_B(x)) + \int_{E_F-eV}^{E_F} dE_z (E_F - E_z) D(E_z,V_B(x))\right]$$

$$eV_B(x) \le E_F \tag{6.7.7}$$

$$J = \frac{me}{2\pi^2\hbar^3}\int_0^{E_F} dE_z (E_F - E_z) D(E_z,V_B) \qquad eV_B(x) \ge E_F \tag{6.7.8}$$

In this simple calculation we use the WKB formula for the transmission coefficient of electrons through a potential barrier of height V_0 (Mendez 1987) under a bias of V_a.

For $eV_B < V_0$ the WKB formula leads to an expression for transmission coefficient

$$D(E_z,V_B(x)) \sim \exp\left[-\frac{4}{3}\left(\frac{2m}{\hbar^2}\right)^{1/2} \frac{b}{eV_B(x)} \left\{(V_0 - V_B(x) - E_z)^{3/2} - (V_0 - E)^{3/2}\right\}\right]$$

(6.7.8)

whereas for $eV_B > V_0$

$$D(E_z,V_B(x)) \sim \exp\left[-\frac{4}{3}\left(\frac{2m}{\hbar^2}\right)^{1/2} \frac{b}{eV_B(x)} (V_0 - E)^{3/2}\right] \tag{6.7.9}$$

For the case $eV_B > V_0 > E_F$ equation 6.7.6 becomes

$$\frac{d^2V_B(x)}{dx^2} = \frac{\rho}{d}\frac{m^*e}{2\pi^2\hbar^3}\int_0^{E_F} dE_z(E_F - E_z)\exp\left[-\frac{4}{3}\left(\frac{2m}{\hbar^2}\right)^{1/2}\frac{b}{eV_B(x)}(V_0 - E)^{3/2}\right] \tag{6.7.10}$$

Integrating this from $x = 0$ to $x = w$ we calculate the in-plane voltage drop in the base under the emitter mesa (15μm×45μm) of an $Al_{0.5}Ga_{0.5}As$ emitter barrier transistor and the emitter current for a measured three-point voltage drop of 0.35V across the barrier using the "Mathcad" software package (Appendix B). The result is plotted in Fig. 6.12.

Fig. 6.12 clearly demonstrates that the in-plane voltage drop in the base under the emitter mesa is negligibly small for a mesa size 15μm×45μm. Fig. 6.13 shows the emitter current density as a function of distance. To calculate the total emitter current we integrate the current density flowing across the contact. For an applied bias of 0.35V across the emitter barrier we get an emitter current of about 0.44μA.

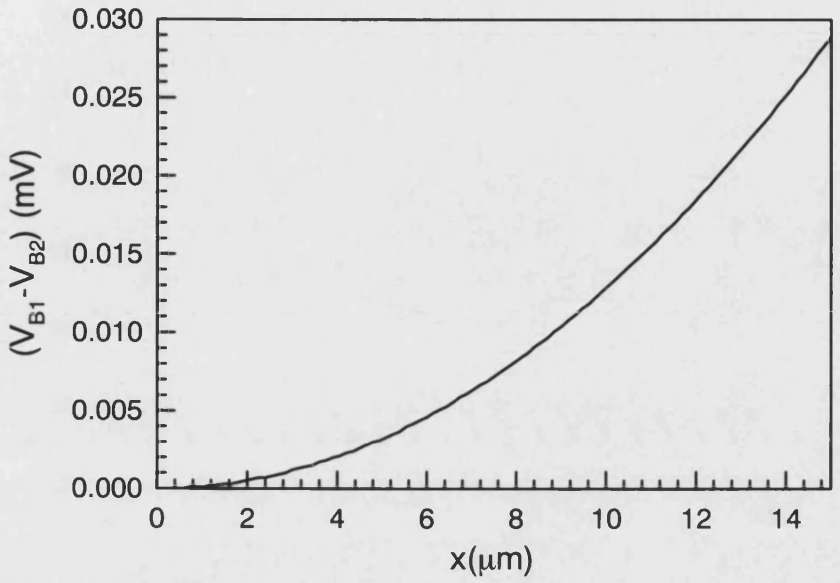

Fig. 6.12A typical plot of the voltage drop along the base at different positions.

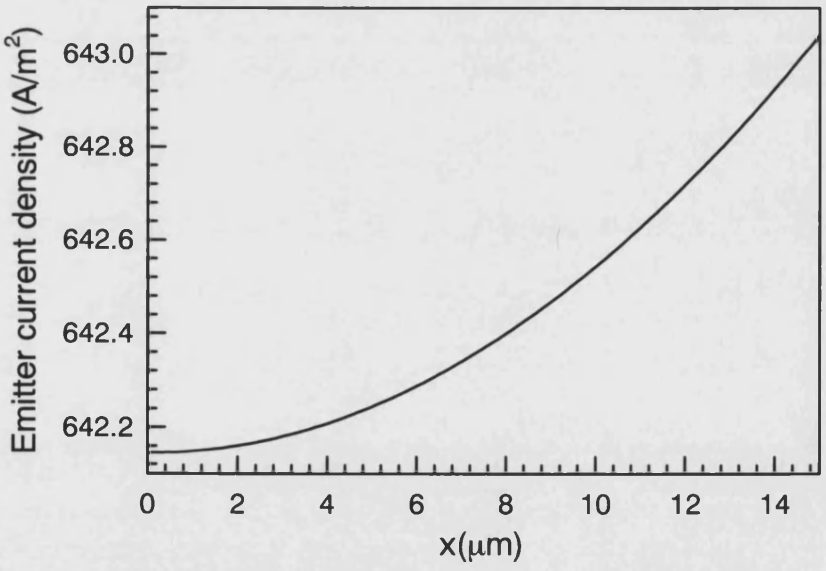

Fig. 6.13 A typical plot of the emitter current density flowing into the base at different positions.

6.8 Subbands in a finite trapezoidal quantum well

Consider a finite tilted quantum well of depth V_0 and width b. Let the voltage across the quantum well be V_a.

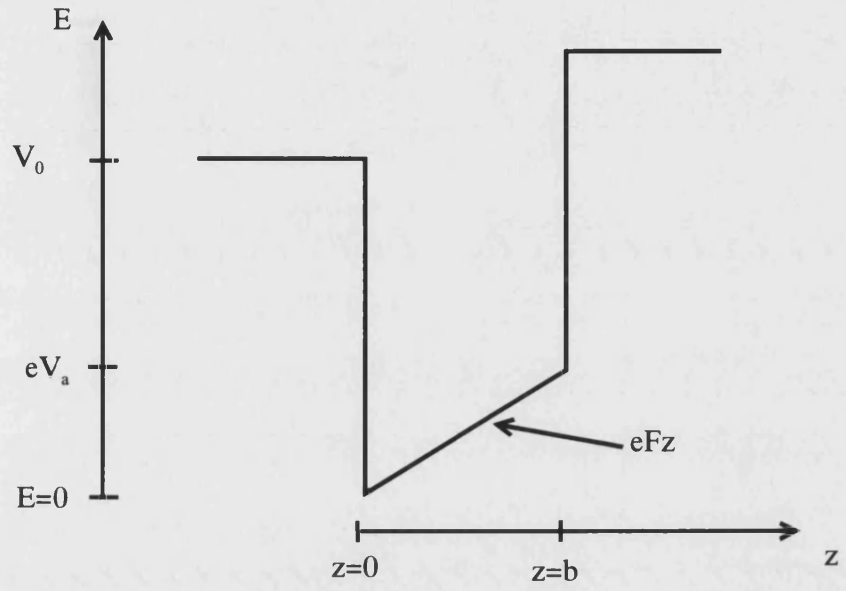

6.14 Schematic representation of a finite quantum well under an applied bias.

The solutions of the Schrödinger equation in the three regions can be written as,

$$\psi_1(z) = A_1 e^{k_1 z} \quad z \le 0 \qquad (6.7.1)$$

where $k_1 = \sqrt{\frac{2m_0^*(V_0 - E)}{\hbar^2}}$ (6.7.2)

and m_0^* is the effective mass outside the well.

and A_1 is an arbitrary constant.

$$\psi_2(z) = C_1 Ai(\rho) + C_2 Bi(\rho) \quad 0 \le z \le b \qquad (6.7.3)$$

where $Ai(\rho)$ and $Bi(\rho)$ are Airy functions of first and second kind respectively.

The argument of the Airy function is given by,

$$\rho = \left(\frac{2m_1^* eF}{\hbar^2}\right)^{1/3}\left(z - \frac{E}{eF}\right) \tag{6.7.4}$$

where m_1^* is the effective mass in the well and $F\left(=\frac{V_a}{b}\right)$ is the electric field across the well.

$$\psi_3(z) = A_3 e^{-k_2 z} \quad z > b \tag{6.7.5}$$

where $k_2 = \sqrt{\frac{2m_0^*(V_0 + V_a - E)}{\hbar^2}}$. (6.7.6)

Imposing the appropriate boundary conditions i.e. ψ and $\frac{1}{m^*}\frac{d\psi}{dz}$ are continuous across the boundaries we get the four simultaneous equations which in matrix form can be written as,

$$\begin{pmatrix} S_1(E) & S_2(E) \\ S_3(E) & S_4(E) \end{pmatrix}\begin{pmatrix} C_1 \\ C_2 \end{pmatrix} = 0 \tag{6.7.7}$$

where $S_1(E) = k_1 Ai(z=0) - \frac{m_0}{m_1}\left(\frac{2m_1 eF}{\hbar^2}\right)^{1/3} Ai'(z=0)$ (6.7.8)

$$S_2(E) = k_1 Bi(z=0) - \frac{m_0}{m_1}\left(\frac{2m_1 eF}{\hbar^2}\right)^{1/3} Bi'(z=0) \tag{6.7.9}$$

$$S_3(E) = k_2 Ai(z=b) + \frac{m_0}{m_1}\left(\frac{2m_1 eF}{\hbar^2}\right)^{1/3} Ai'(z=b) \tag{6.7.10}$$

$$S_4(E) = k_2 Bi(z=b) + \frac{m_0}{m_1}\left(\frac{2m_1 eF}{\hbar^2}\right)^{1/3} Bi'(z=b) \tag{6.7.11}$$

For non-trivial solutions of these simultaneous equations we have,

$$S_1(E).S_4(E) - S_2(E).S_3(E) = 0 \qquad (6.7.12)$$

This can be solved numerically (see Appendix B) and the energies of the subbands within the well can be calculated using accepted values for the band offsets (Γ(GaAs)- Γ(AlAs)=1eV, and X(GaAs)-X(AlAs)=0.35eV) and effective masses ($m_{\Gamma}(GaAs) = 0.067m_0$, $m_{X_l}(AlAs) = 1.1m_0$, $m_{X_t}(AlAs) = 0.2m_0$). The results are tabulated below.

	E(meV) $V_{BE} = 100mV$	E(meV) $V_{BE} = 150mV$	E(meV) $V_{BE} = 200mV$	E(meV) $V_{BE} = 250mV$	E(meV) $V_{BE} = 300mV$
$X_t^1 (X_l^1)$	35(20)	46(26)	56(32)	65(37)	74(42)
$X_t^2 (X_l^2)$	68(36)	84(47)	101(56)	116(65)	131(73)
$X_t^3 (X_l^3)$	108(47)	126(62)	143(75)	161(88)	179(99)
$X_t^4 (X_l^4)$	167(60)	184(78)	202(94)	219(108)	237(122)
$X_t^5 (X_l^5)$	242(72)	258(91)	275(109)	292(126)	310(143)

Chapter 7

Experimental Results

7.1 Introduction

Experimental results and a detailed analysis are presented for two types of tunnelling hot electron transistor structure that are identical except the emitter barrier is composed of $Al_{0.5}Ga_{0.5}As$ (NU1223) in the first case and AlAs (NU1224) in the second. The MBE layer sequence of the device structures was described in chapter 5. Fig 7.1 shows the conduction band profile of the emitter barrier of both transistors at ambient pressure under an applied bias of 300mV. The calculated positions of the X-point subbands for the AlAs emitter barrier device (NU1224) are also shown. Details of the calculation of the X-point subbands were given in chapter 3. The contact regions (emitter, base and collector) are n^+-doped at a carrier concentration of $1\times10^{18}cm^{-3}$ giving rise to Fermi level 55meV above the conduction band edge. Upon biasing between the emitter and base contacts electrons accumulate near the emitter/barrier interface and deplete on the base side causing band bending. Since the current density flowing through the barriers is very sensitive to their shape voltage drops across accumulation, barrier and depletion regions were calculated using a classical solution of the Poisson equation (described in chapter 6).

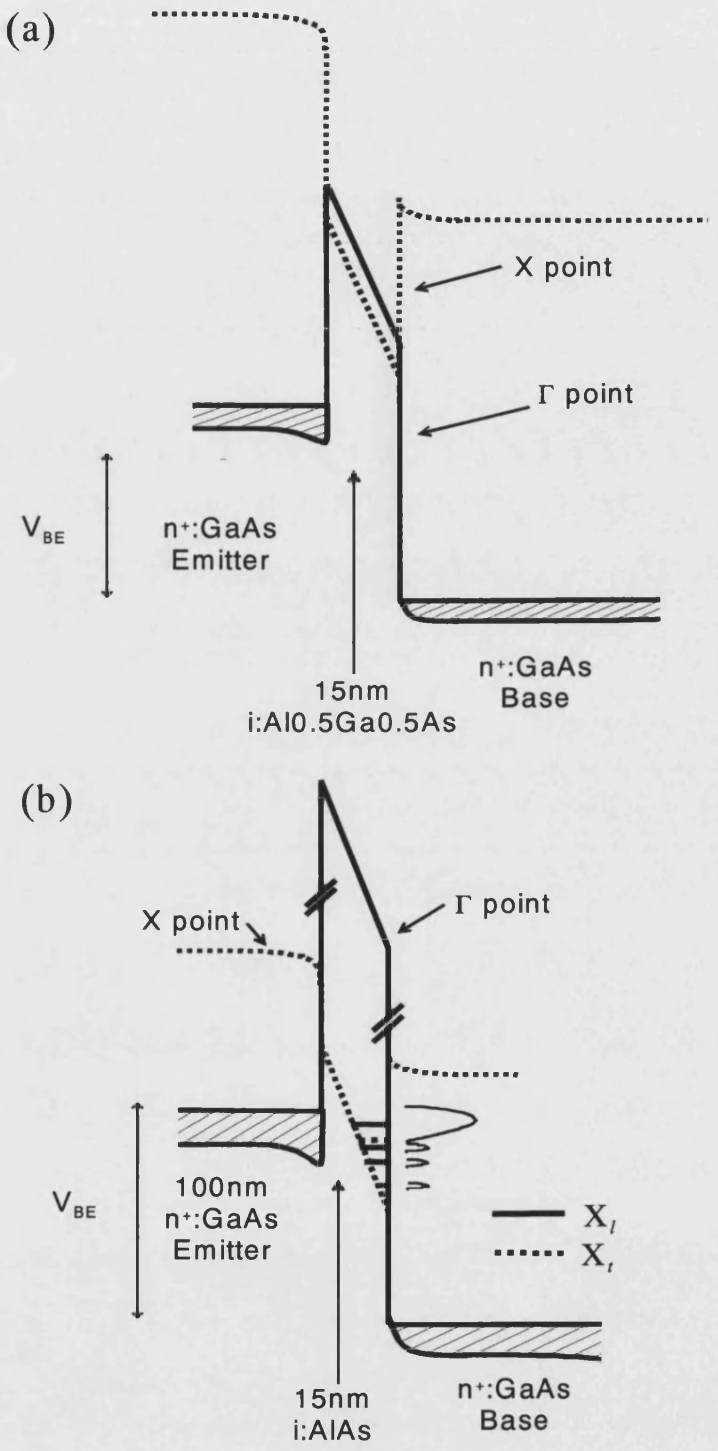

Fig. 7.1 Schematic conduction band profiles of a (a) 15nm $Al_{0.5}Ga_{0.5}As$ and (b) 15nm AlAs emitter barrier in the transistors under an applied bias at ambient pressure. The solid (dotted) line represents the Γ-point (X-point) conduction band minima.

7.2 Ambient pressure measurements

Measurements at ambient pressure were performed in a cryo-cooler down to 8K. A detailed description of the characterisation techniques and ambient pressure measurements was given in chapter 5. In this section data obtained from 15nm AlAs emitter barrier devices having emitter/base mesa sizes of 30μm×10μm (NU1224/A) and 45μm×15μm (NU1224/B), and from 15nm $Al_{0.5}Ga_{0.5}As$ emitter barrier devices of mesa size 45μm×15μm (NU1223/B) will be presented.

7.2.1 Samples NU1224/A and NU1224/B -AlAs emitter barrier

At low temperature carriers predominantly tunnel through the emitter barrier quantum mechanically while the collector barrier is so thick that the tunnelling component is unimportant (Fig 7.2a). However, an applied bias tilts the collector barrier and carriers incident just below the barrier height can now tunnel through the tip of distorted collector barrier via Fowler-Nordheim tunnelling (Fig 7.2b). If the energy of the incident electrons exceeds the barrier height they can pass the collector barrier with little attenuation (Fig. 7.2c).

Two terminal current-voltage (I-V) and conductance-voltage (dI/dV-V) measurements between collector and emitter/base contacts were performed in order to confirm the tunnelling nature of the emitter barrier and the blocking action of the collector barrier. Fig. 7.3 shows two terminal I-V and dI/dV-V measurements at 8K between collector and emitter electrodes. At low bias voltages the current flowing through the device is negligibly small and under strong forward bias the current rises rapidly as the electrons acquire enough energy to surmount the collector barrier.

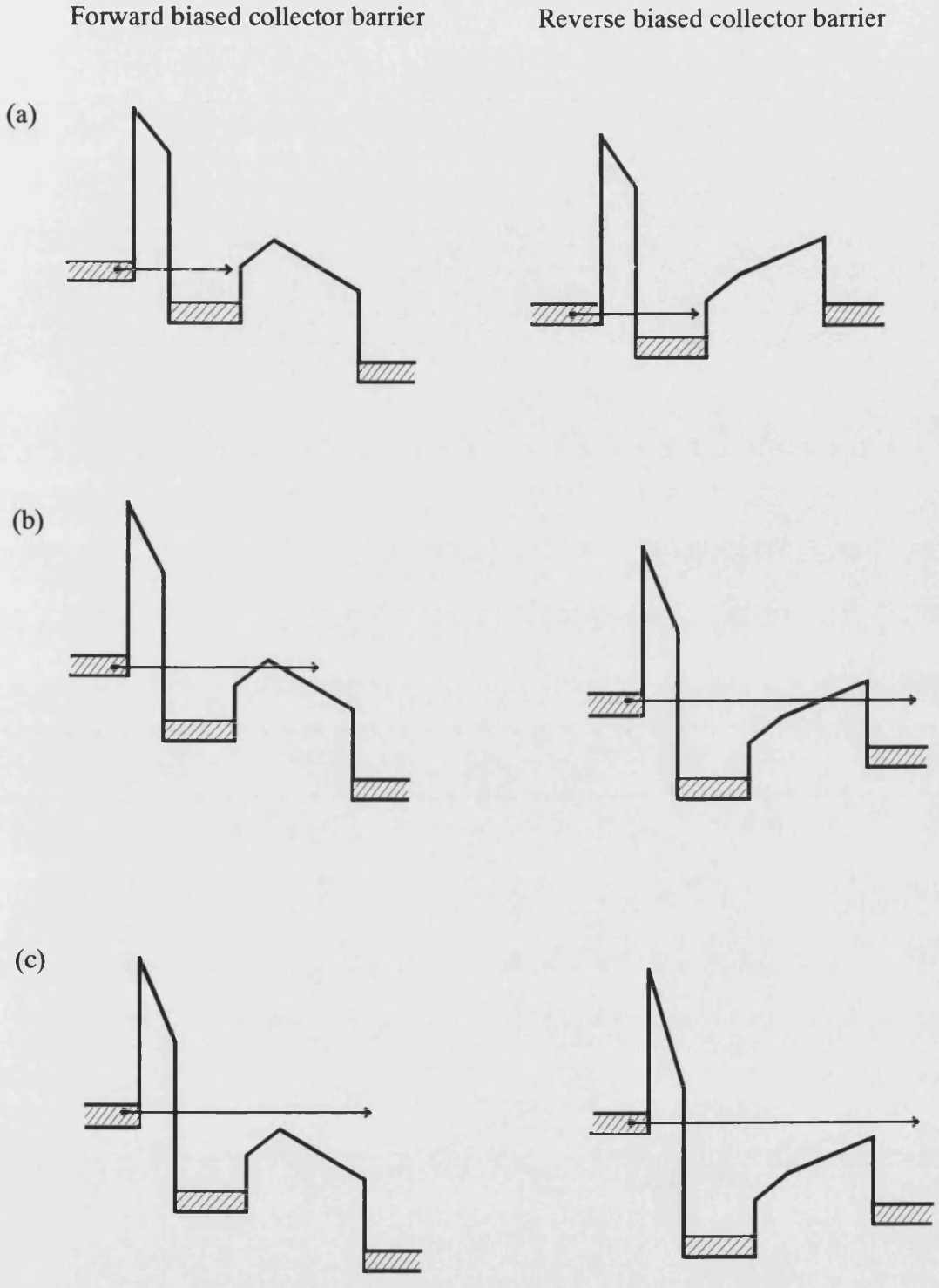

Fig. 7.2 Schematic illustration of the high pass filter action of the collector barrier when a bias voltage is applied between base and collector.

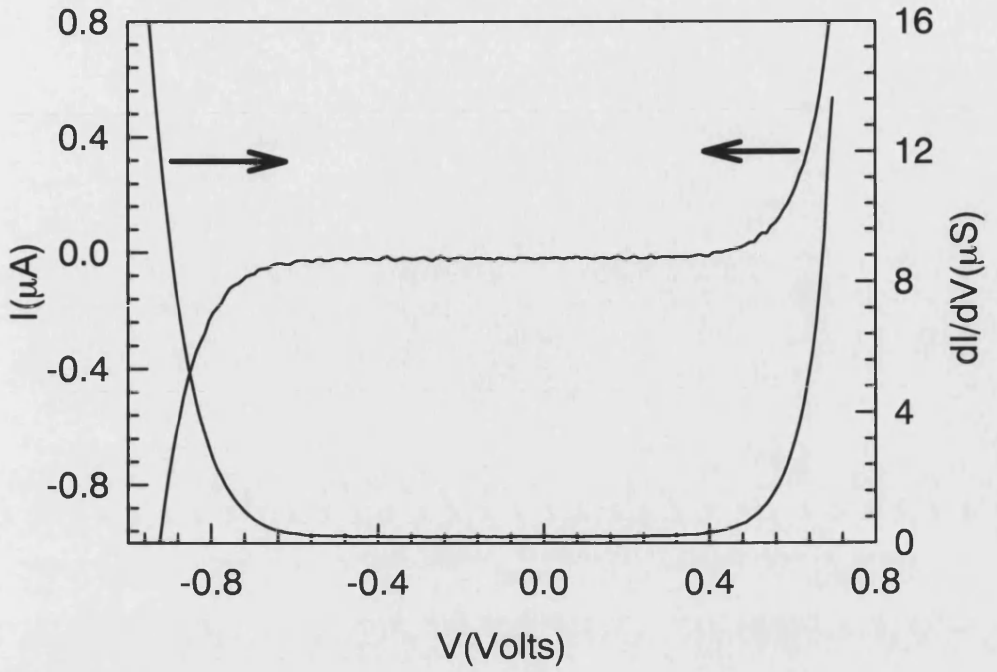

Fig. 7.3 Two-terminal current-voltage and conductance-voltage characteristics measured between collector and emitter at 8K and ambient pressure.

Two terminal current and conductance measurements between emitter and base are shown in Fig. 7.4. The shape of Figure demonstrates the tunnelling nature of the emitter barrier and confirms that the upper Ohmic contacts do not short the collector barrier through the narrow base layer.

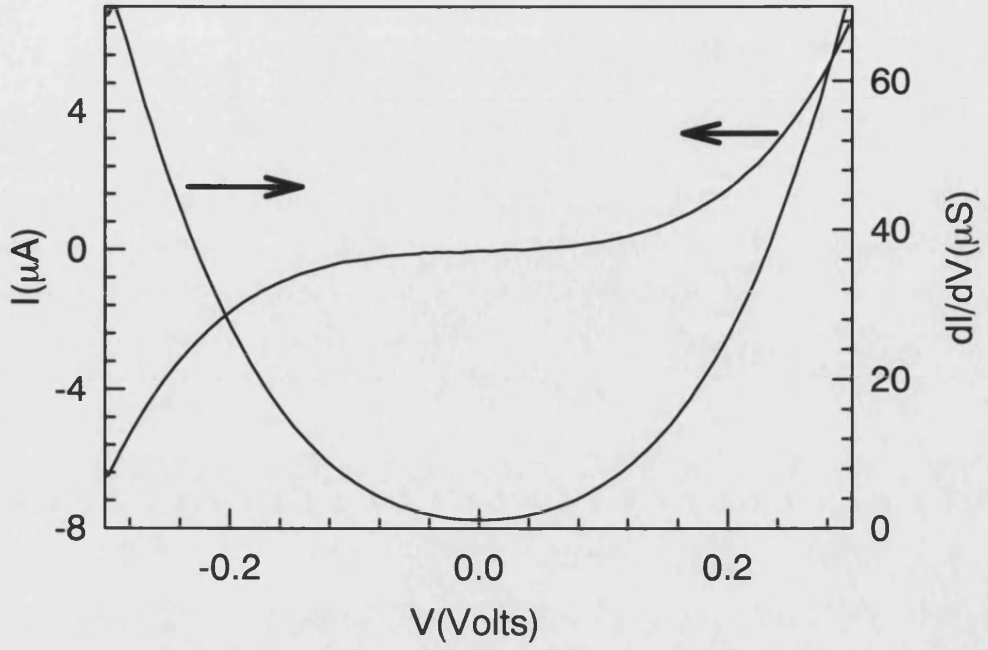

Fig. 7.4 Two-terminal current-voltage and conductance-voltage characteristics measured between emitter and base at 8K and ambient pressure.

Fig. 7.4, however, contains a contribution due to the base series resistance, which can be eliminated by performing measurements in a three-point geometry employing separate base contacts (described in section of chapter 5). In Fig. 7.5 three-point current-voltage and conductance-voltage characteristics of the emitter barrier are shown. These data were collected while leaving the collector contact floating. The exponential dependence of current on the applied bias confirms that electron tunnelling through the barrier is the dominant transport mechanism.

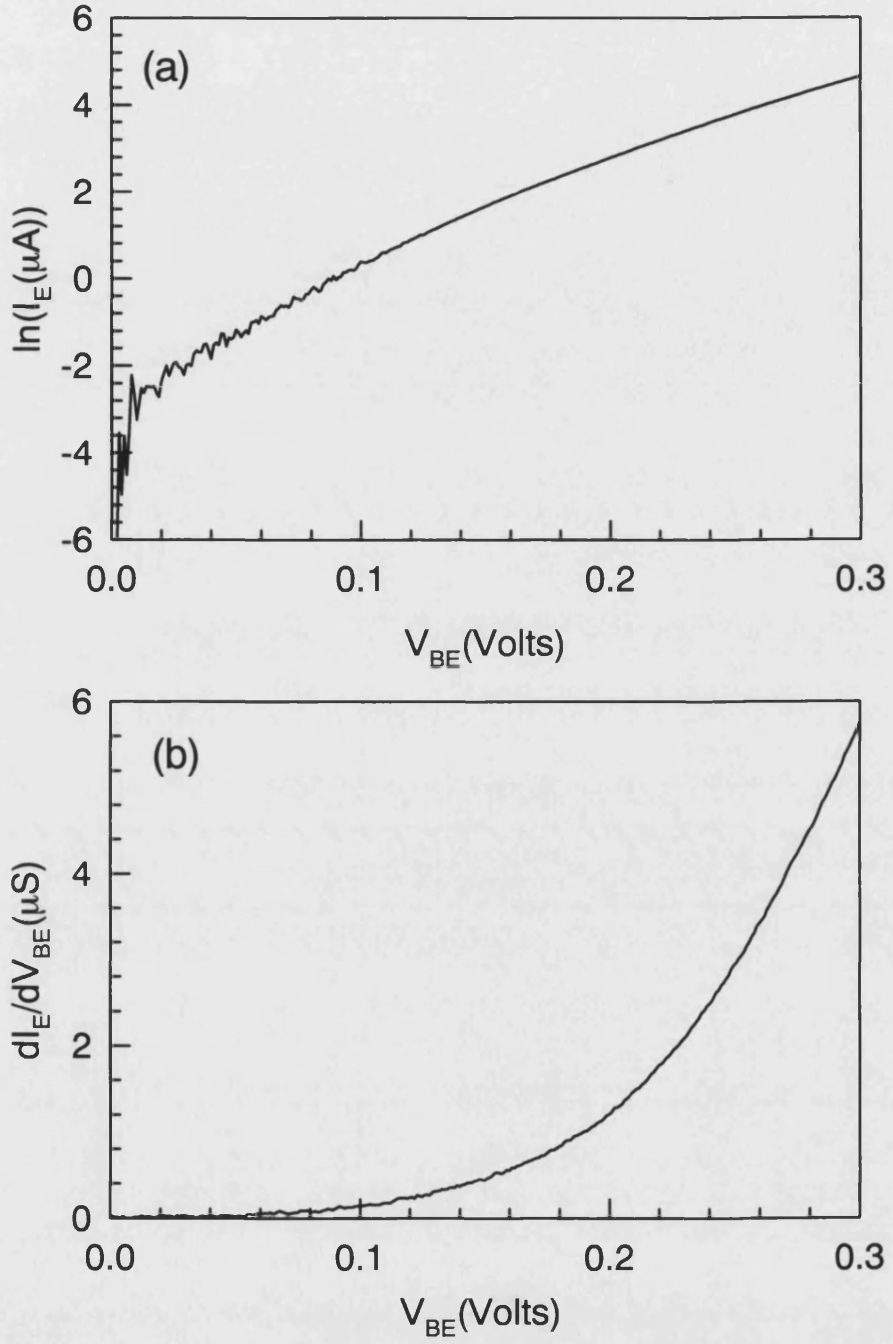

Fig 7.5 Three-point (a) log(current)-voltage and (b) conductance-voltage characteristics of the emitter barrier at 8K measured with the collector contact floating.

These three-point I-V and dI/dV-V measurements are equivalent to the two terminal I-V and dI/dV measurements of single barrier diodes reported by Landheer *et al.* (1989), Beresford *et al.* (1989) and Carbonneau *et al.* (1993). X-point related resonances have been observed in their I-V measurements of single AlAs barriers of thickness 4.1nm, 5.2nm (Landheer *et al.* 1989, Carbonneau *et al.* 1993.) and 4nm (Beresford *et al.* 1989). Similar resonance features have been reported recently by Finley *et al.* (1998) in single AlAs barriers of thickness 4.5nm and 6.5nm with 2D emitter electrodes. Our ambient pressure measurements do not reveal any resonances either in I-V or dI/dV-V curves. This may be due to the fact that the energy separation between successive X-point subbands in our AlAs barriers is much smaller than the emitter Fermi band (55meV) making it difficult to resolve resonances.

Common-emitter current-voltage and transconductance-voltage characteristics for various injection currents at 8K are shown in Fig. 7.6 and Fig. 7.7. The injection voltages (or energies) were monitored using the second base contacts in the three-point measurement configuration. The advantage of the common-emitter configuration is that the series resistance at the base contacts does not influence the collector bias voltage. However, in this configuration it is not possible to vary the emitter and collector barrier biases independently. Even though the current-voltage characteristics (Fig. 7.6a) are featureless and monotonic the transconductance data (Fig. 7.6b) display tiny peaks together with a large background that increases rapidly towards higher collector-base bias voltages. In Fig. 7.7 common-emitter current-voltage and transconductance-voltage characteristics are plotted on an expanded scale. We clearly see the ballistic peak and several smaller peaks that are indicated by arrows in Fig. 7.7b which stand out from the large background.

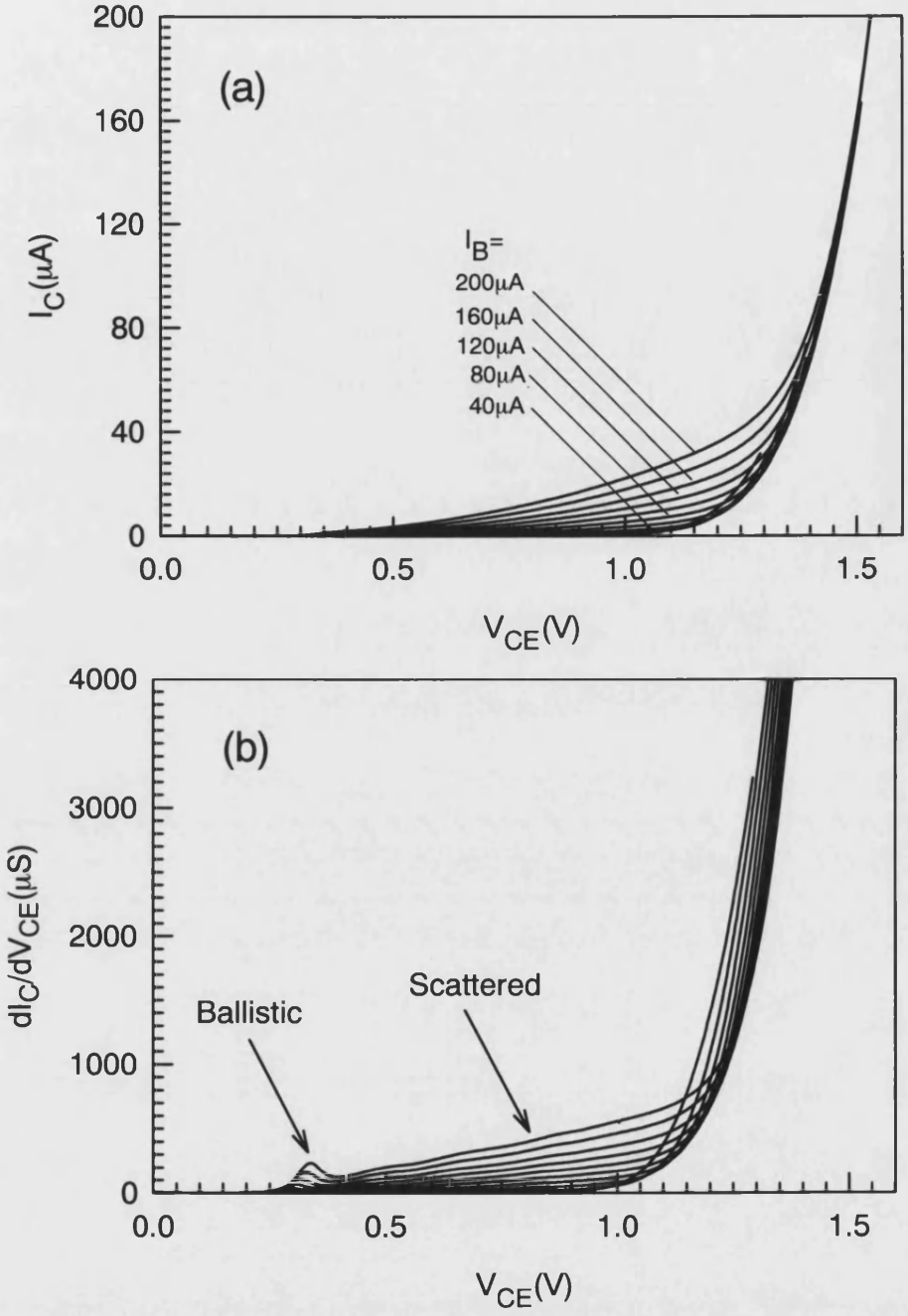

Fig. 7.6 Common-emitter (a) current-voltage and (b) transconductance-voltage characteristics of transistor (NU1224/A) for injection currents from 20μA to 200μA in 20μA intervals measured at ambient pressure and 8K.

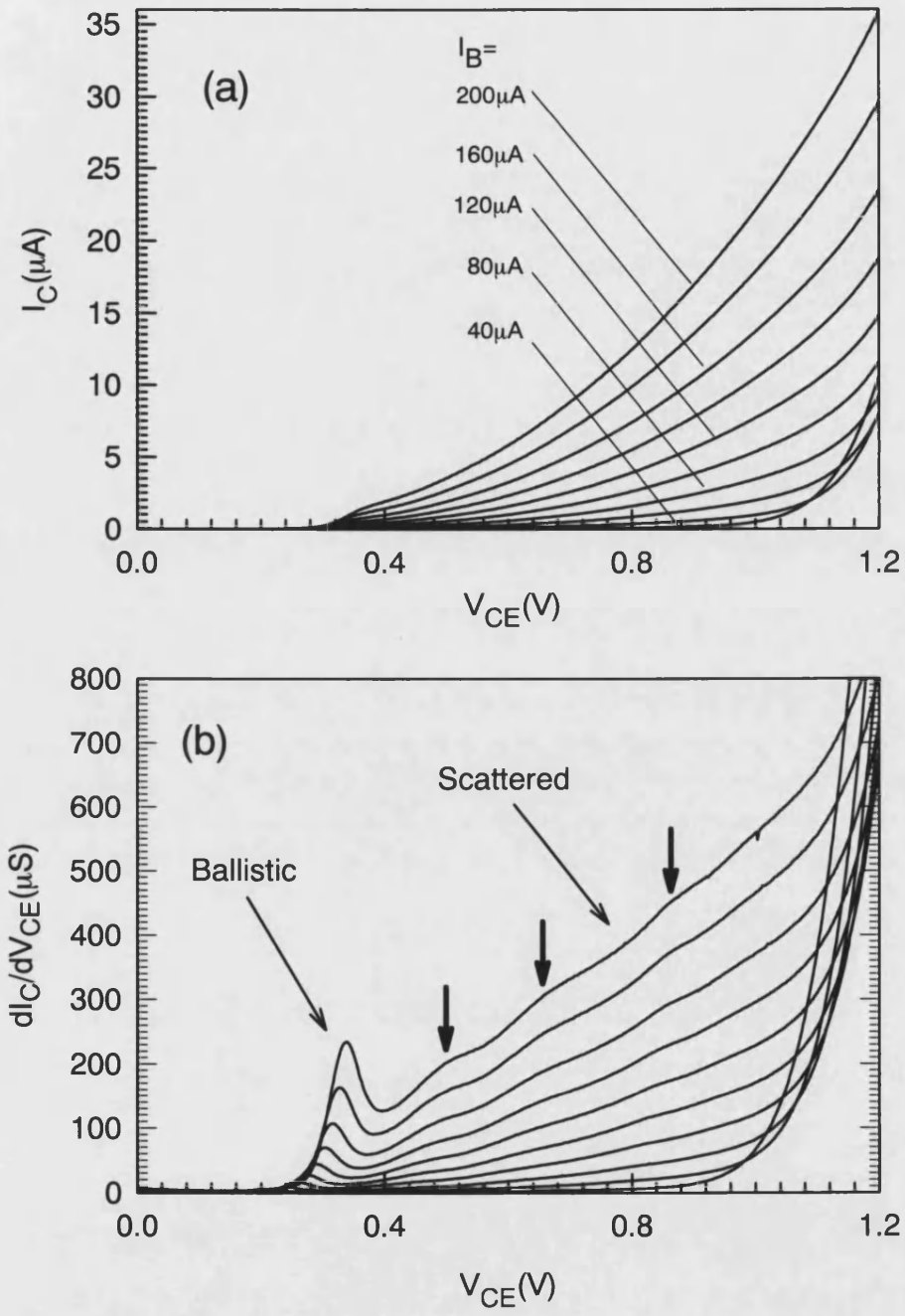

Fig. 7.7 Expanded scale plot of common-emitter (a) current-voltage and (b) transconductance-voltage characteristics of transistor (NU1224/A) for injection currents from 20μA to 200μA in 20μA intervals measured at ambient pressure and 8K.

Fig. 7.8 and Fig. 7.9 show common-base I_C-V_{CB} and dI_C/dV_{CB}-V_{CB} characteristics at 8K. These data were obtained in the two-point common-base mode and contain a contribution due to the series resistances at the base contacts. The transconductance spectra exhibit similar ballistic peaks at the onset as also observed in common-emitter mode as well as a large structured background contribution and a pronounced relaxed electron peak at high biases. The latter large peaks represent collection of thermalised electrons from the base layer. The tiny peaks at the onset appear to be collected at unrealistically large energies due to the contribution of the base resistance in the circuitry. The same fact causes these peaks to move rapidly towards higher collection energies (more negative) as the injection current is increased. On subtracting the base series resistance contribution from the collector-base bias the peaks are found to occur at almost the same collection energy (Heiblum *et al.* 1985b).

Three-point measurements (described in chapter 5) were performed and the effect of the series resistance was subtracted from the two-point data using the algorithm given in Appendix C. Corrected current and transconductance data are shown in Fig. 7.10.

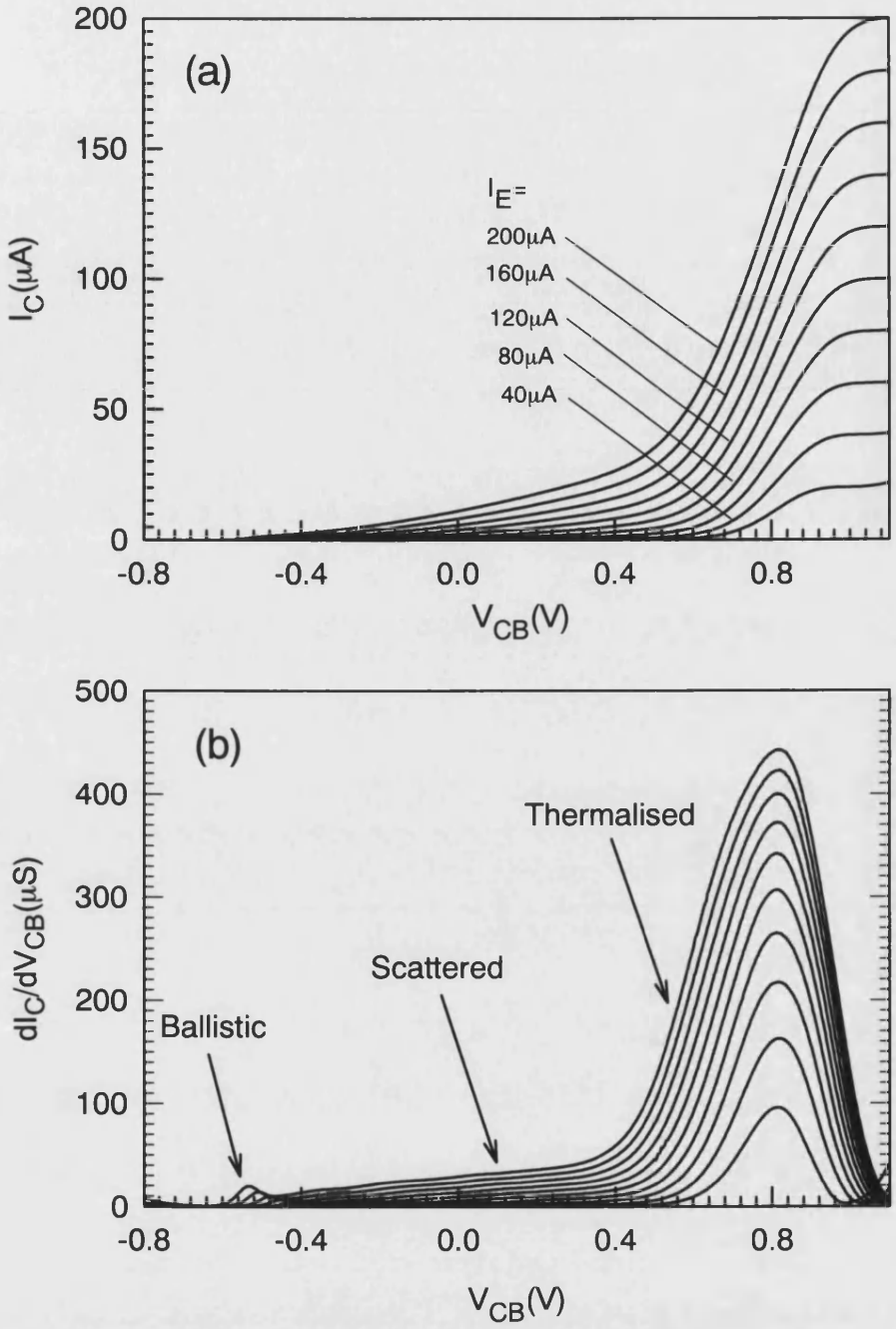

Fig. 7.8 Two-point common-base (a) current-voltage and (b) transconductance-voltage characteristics of transistor (NU1224/A) for injection currents from 20μA to 200μA in 20μA intervals measured at ambient pressure and 8K.

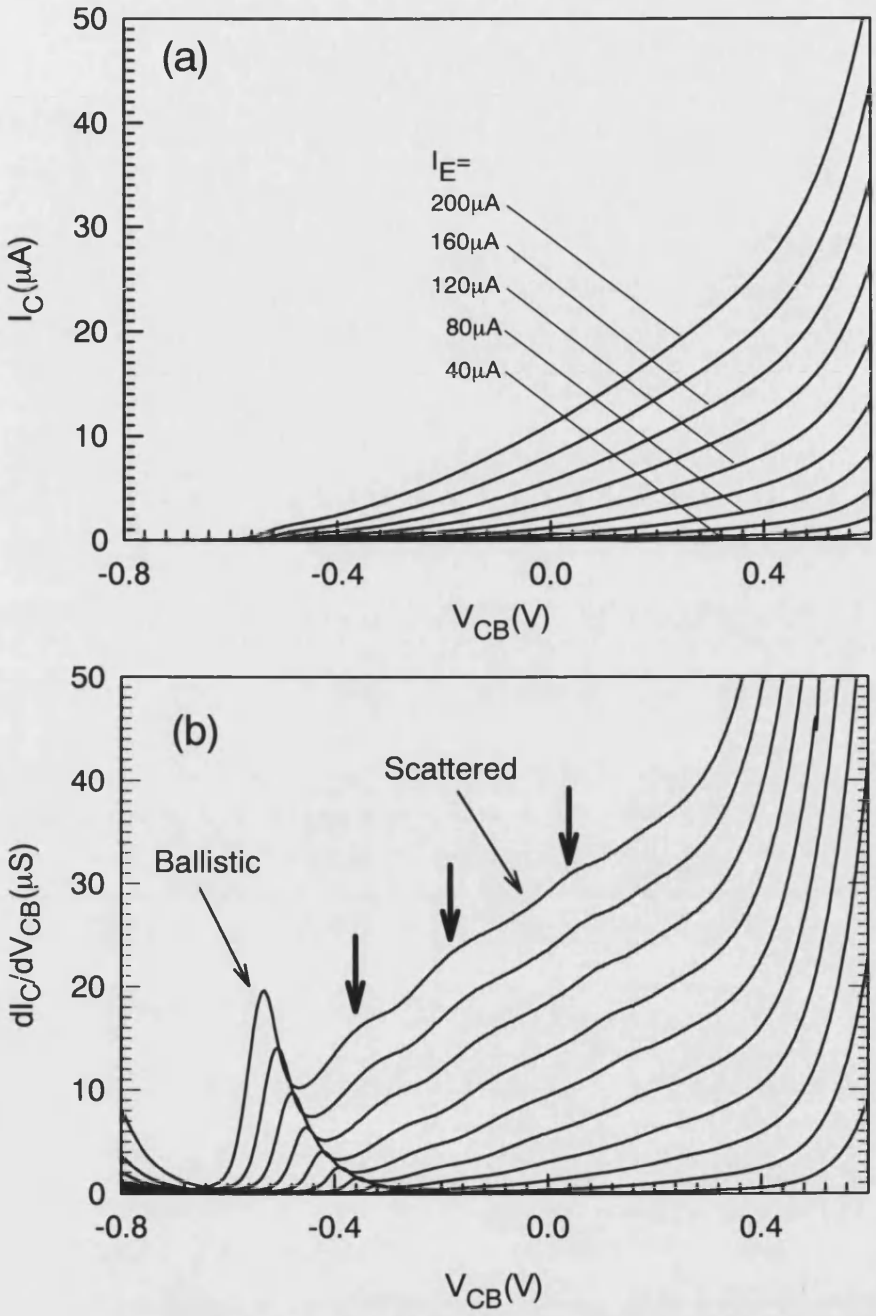

Fig. 7.9 Expanded scale plot of two-point common-base (a) current-voltage and (b) transconductance-voltage characteristics of transistor (NU1224/A) for injection currents from 20μA to 200μA in 20μA intervals measured at ambient pressure and 8K.

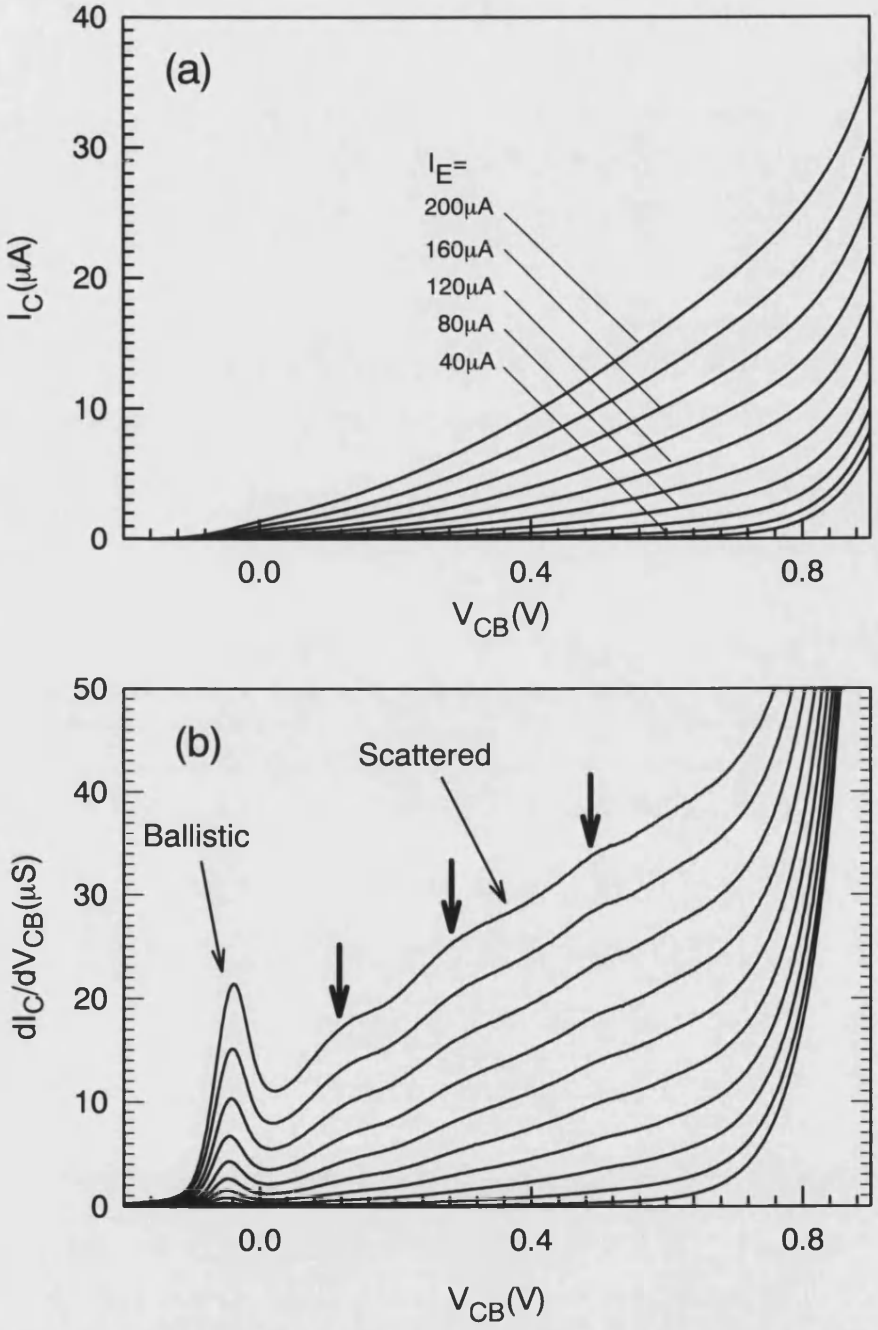

Fig. 7.10 Three-point common-base (a) current-voltage and (b) transconductance-voltage characteristics of transistor (NU1224/A) for injection currents from 20μA to 200μA in 20μA intervals measured at ambient pressure and 8K.

The peak positions in the scattered spectrum have been more clearly identified by performing second derivative measurements. Fig. 7.11 shows a typical three-point common-base transconductance measurement and its derivative.

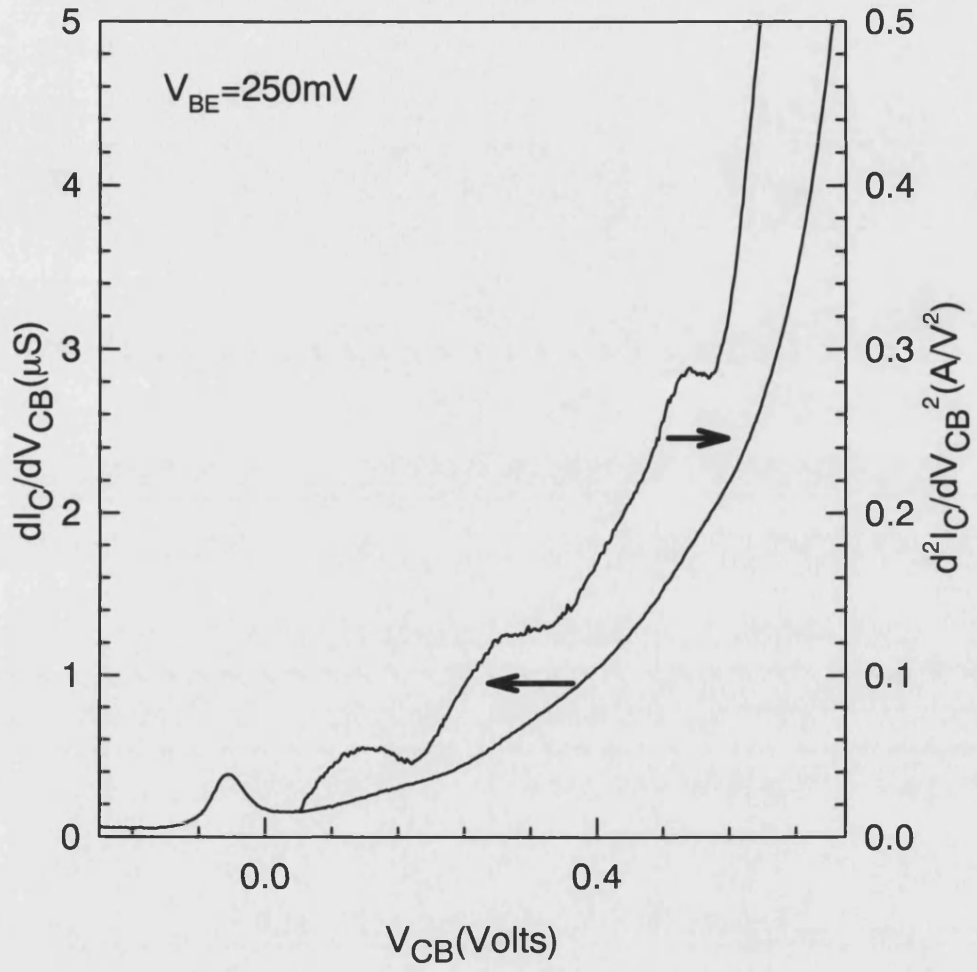

Fig. 7.11 Three-point common-base transconductance and its derivative for an injection voltage of 250mV.

Similar characteristics have been observed in the device with the 45μm×15μm emitter/base mesa. Three-point log(current)-voltage and conductance-voltage plots of this emitter barrier are shown in Fig. 7.12. We note that in this device higher current densities flow through the emitter barrier for a given value of emitter-base bias voltage due to the larger area of the emitter and base contact pads.

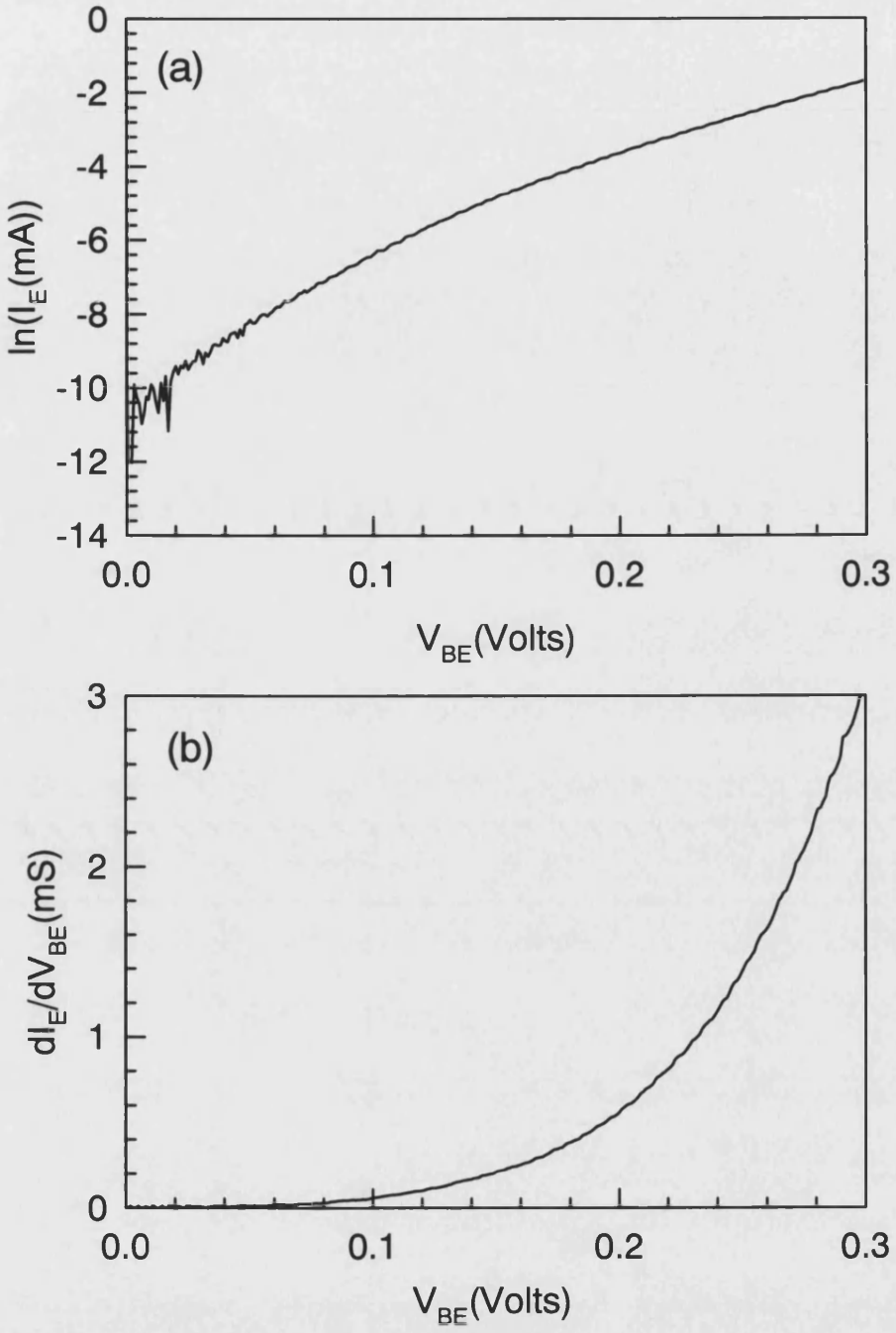

Fig. 7.12 Three-point (a) log(current)-voltage and (b) conductance-voltage characteristics for the AlAs emitter barrier of transistor NU1224/B measured at 8K with the collector contact floating.

Common-emitter and three-point common-base current-voltage and transconductance-voltage characteristics are shown in Fig. 7.13 and 7.14 respectively. The positions of the tiny "ballistic" transconductance peaks, and the peaks in the background of the scattered electrons are in close agreement with those of sample NU1224/A.

The onsets of the collector current in the current-voltage characteristics measured in common-emitter (Fig. 7.7a and Fig. 7.13a) and common-base (Fig. 10a and Fig. 7.14a) mode appear as a well-defined peak in the respective transconductance spectrum. The position of these peaks in the three-point common-base mode transconductance spectrum (Fig. 7.10b and Fig. 14b) and the fact that the half width of the peak remains approximately constant for all values of injection current (or energy) indicate that they arise due to the collection of quasiballistic electrons. In both devices it has been estimated that about 1% of the injected electrons are collected within these peaks. The large scattered background in the transconductance plot indicates that the majority of the injected electrons lose substantial energy before collection. These energy losses may occur in different regions of the device structure.

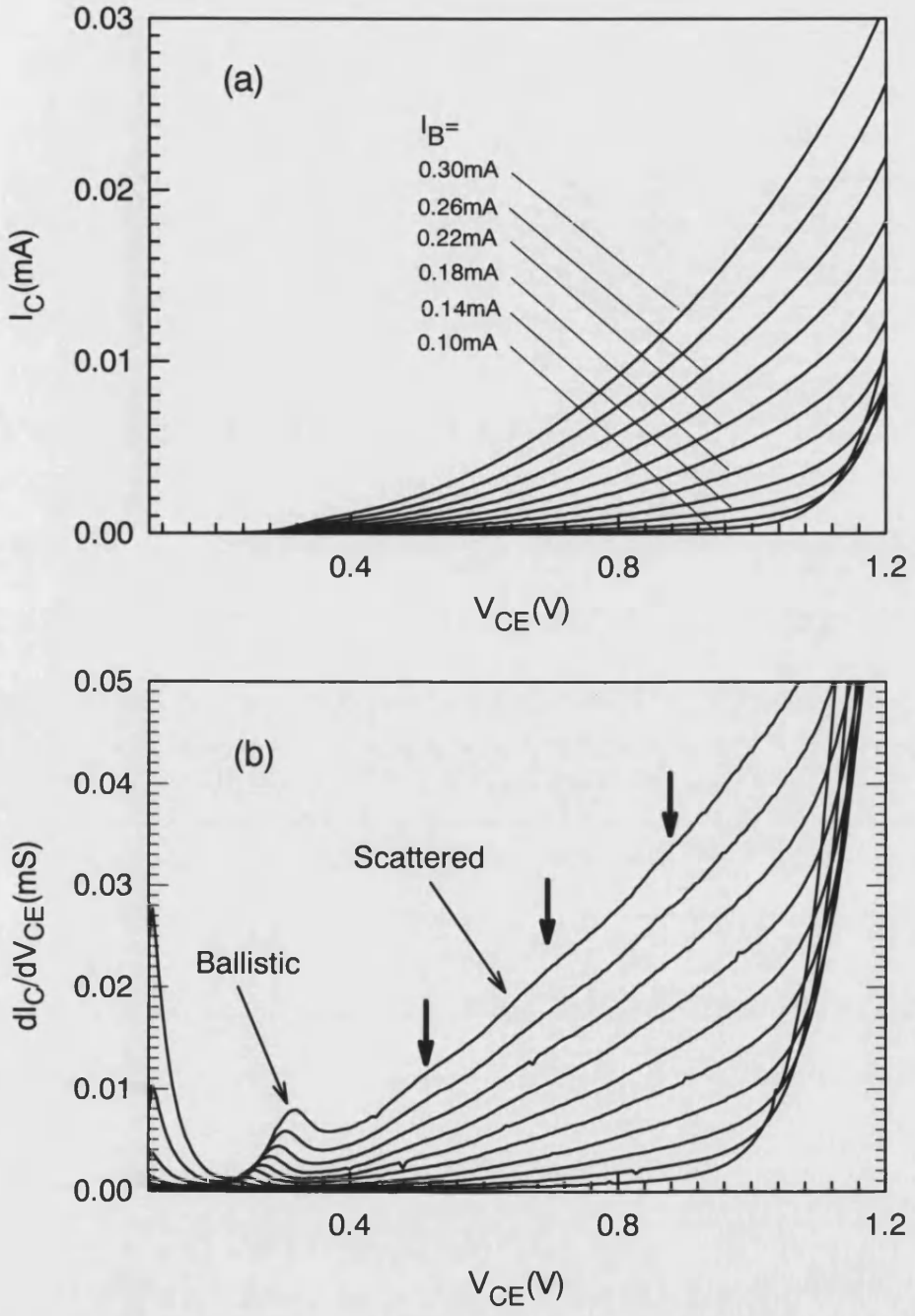

Fig. 7.13 Common-emitter (a) current-voltage and (b) transconductance-voltage characteristics of transistor (NU1224/B) for injection currents from 0.1mA to 0.3mA in 0.02mA intervals measured at ambient pressure and 8K.

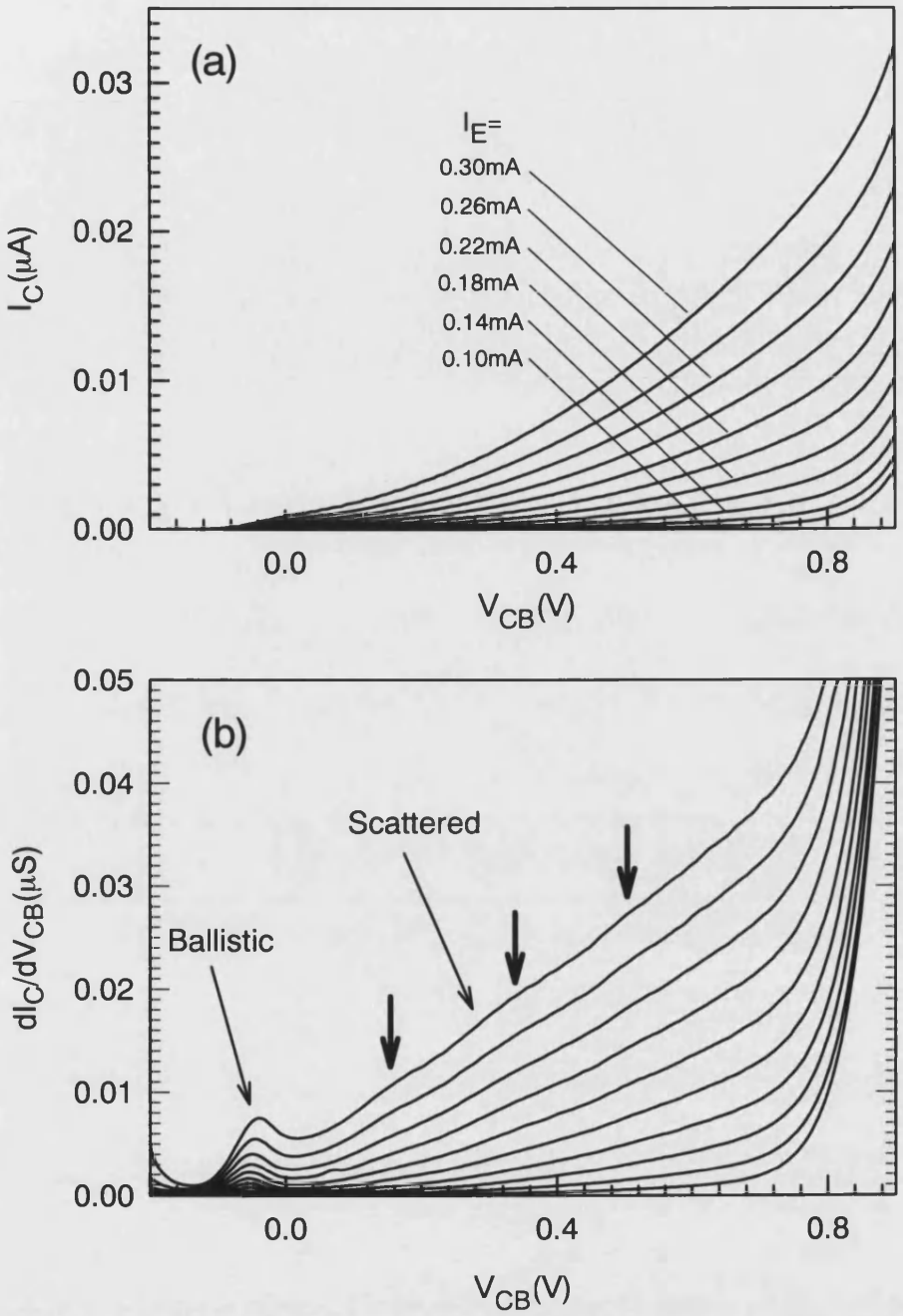

Fig. 7.14 Three-point common-base (a) current-voltage and (b) transconductance-voltage characteristics of transistor (NU1224/B) for injection currents from 0.1mA to 0.3mA in 0.02mA intervals measured at ambient pressure and 8K.

One possible explanation for the peaks in the scattered spectrum is that they represent Longitudinal Optical (LO) phonon replicas of the injected distribution. Using specially designed transistor structures energy loss via LO phonon scattering in the base region was established by Heiblum *et al.* (1989) and Lam *et al.* (1995). However using an $Al_{0.3}Ga_{0.7}As$ emitter barrier and a collector barrier which is similar to the one incorporated in our transistor structure no evidence for LO phonon scattering in the base region was found (Heiblum *et al.* 1985a and Bending *et al.* 1989a).

In order to be more specific about the origin of the peaks in the scattered electron distribution, their widths and positions in the three-point common-base transconductance spectra (Fig. 7.10b) have been analysed using the calculated lever rule for the collector barrier (described in chapter 6). Fig. 7.15 shows the correctly scaled spectrum at an injection energy of 300meV. On the vertical axis the relative change of collector barrier height for a given collector-base bias is shown. The separation between the quasiballistic peak and the peaks in the scattered background are also shown in the Figure.

The peaks in the scattered spectrum are found to be too narrow to be consistent with phonon replicas of the main quasiballistic peak. In addition the energy separations do not correspond to any known phonon energies.

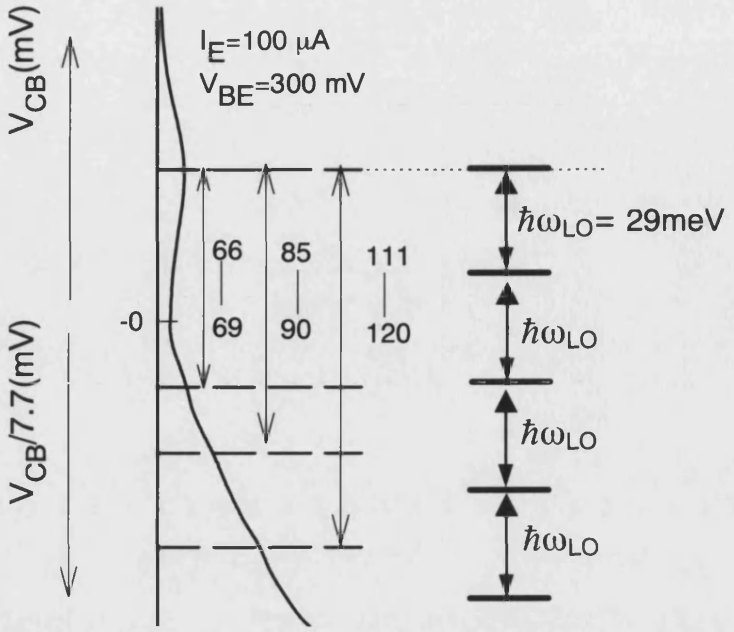

Fig. 7.15 Three-point common-base transconductance data for an injection energy of 300meV plotted using the calculated lever rule for the collector barrier. LO phonon energy replicas are also shown in this Figure for comparison assuming zone boundary LO phonon.

Even though Heiblum *et al.* (1987) demonstrated a quantisation effect in the thin base layer it is undetectable in the transconductance measurements (Heiblum *et al.* 1985a and Bending *et al.* 1989a). In addition the transfer of injected electrons into higher valleys in the base region (Heiblum *et al.* (1986) only becomes significant at a high hydrostatic pressures. All these observations suggest that the origin of large structured background in the transconductance spectrum must be related to the transport processes within the indirect AlAs barriers themselves. In order to confirm this speculation a transistor with a nominally direct $Al_{0.5}Ga_{0.5}As$ emitter barrier (NU1223) was designed and fabricated. Data collected from this transistor (NU1223) are given in the next section.

7.2.2 Sample NU1223/B – $Al_{0.5}Ga_{0.5}As$ emitter barrier

In Fig 7.16 two terminal emitter-collector current-voltage and conductance-voltage measurements of the $Al_{0.5}Ga_{0.5}As$ emitter barrier transistor are plotted. As observed for the AlAs emitter barrier transistor (NU1224/A) these plots clearly demonstrate the blocking action of the collector barrier.

Fig. 7.17 shows two-terminal measurements between the emitter and base. The plots demonstrate that the $Al_{0.5}Ga_{0.5}As$ emitter barrier behaves like a very high impedance tunnel barrier making it impossible to perform three-point measurements with available operational amplifiers.

Fig 7.18 shows common-emitter current-voltage and transconductance-voltage characteristics of the $Al_{0.5}Ga_{0.5}As$ emitter barrier transistor. In Fig 7.19 two-point common-base current-voltage and transconductance-voltage characteristics of the $Al_{0.5}Ga_{0.5}As$ emitter barrier transistor (NU1223/B) are shown for various injection currents measured at 8K and ambient pressure.

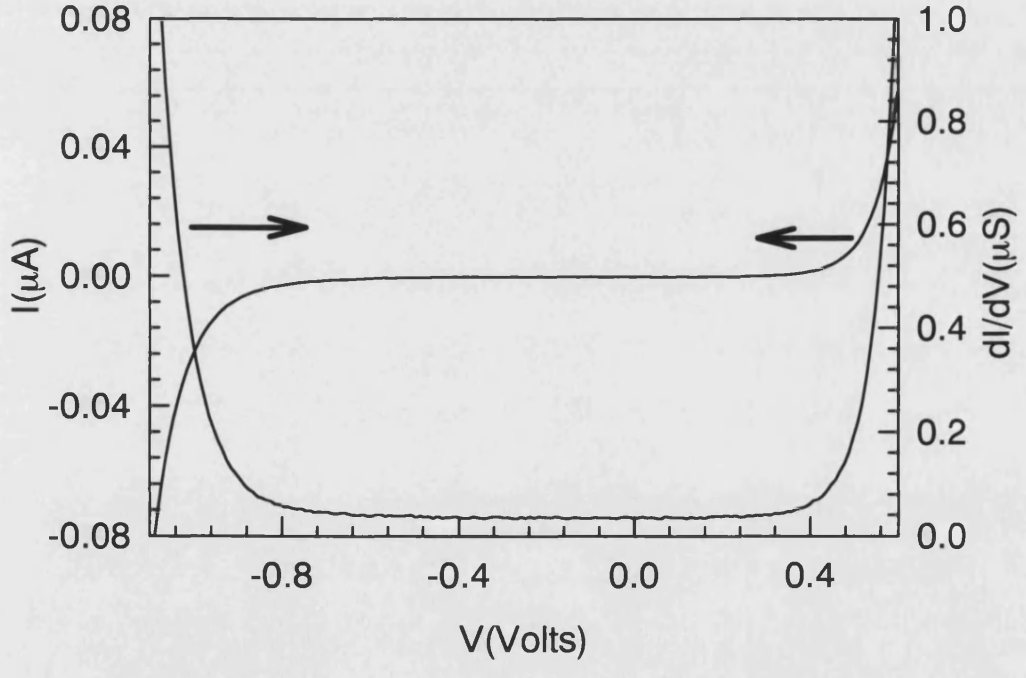

Fig. 7.16 Two-terminal current-voltage and conductance-voltage characteristics measured between collector and emitter at 8K and ambient pressure.

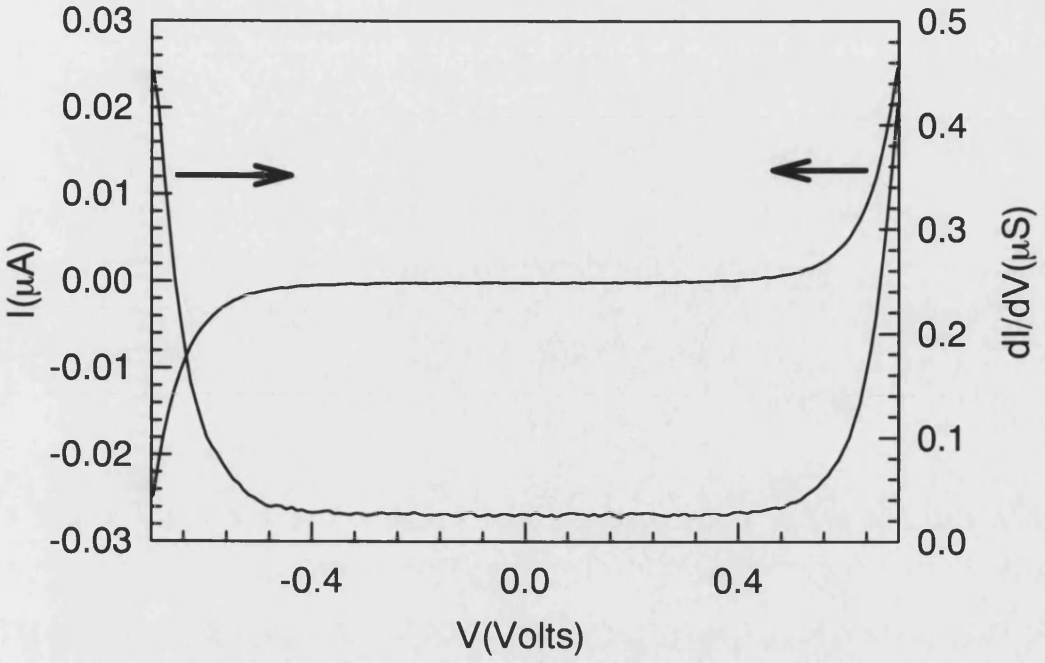

Fig. 7.17 Two-terminal current-voltage and conductance-voltage characteristics measured between emitter and base and at 8K and ambient pressure.

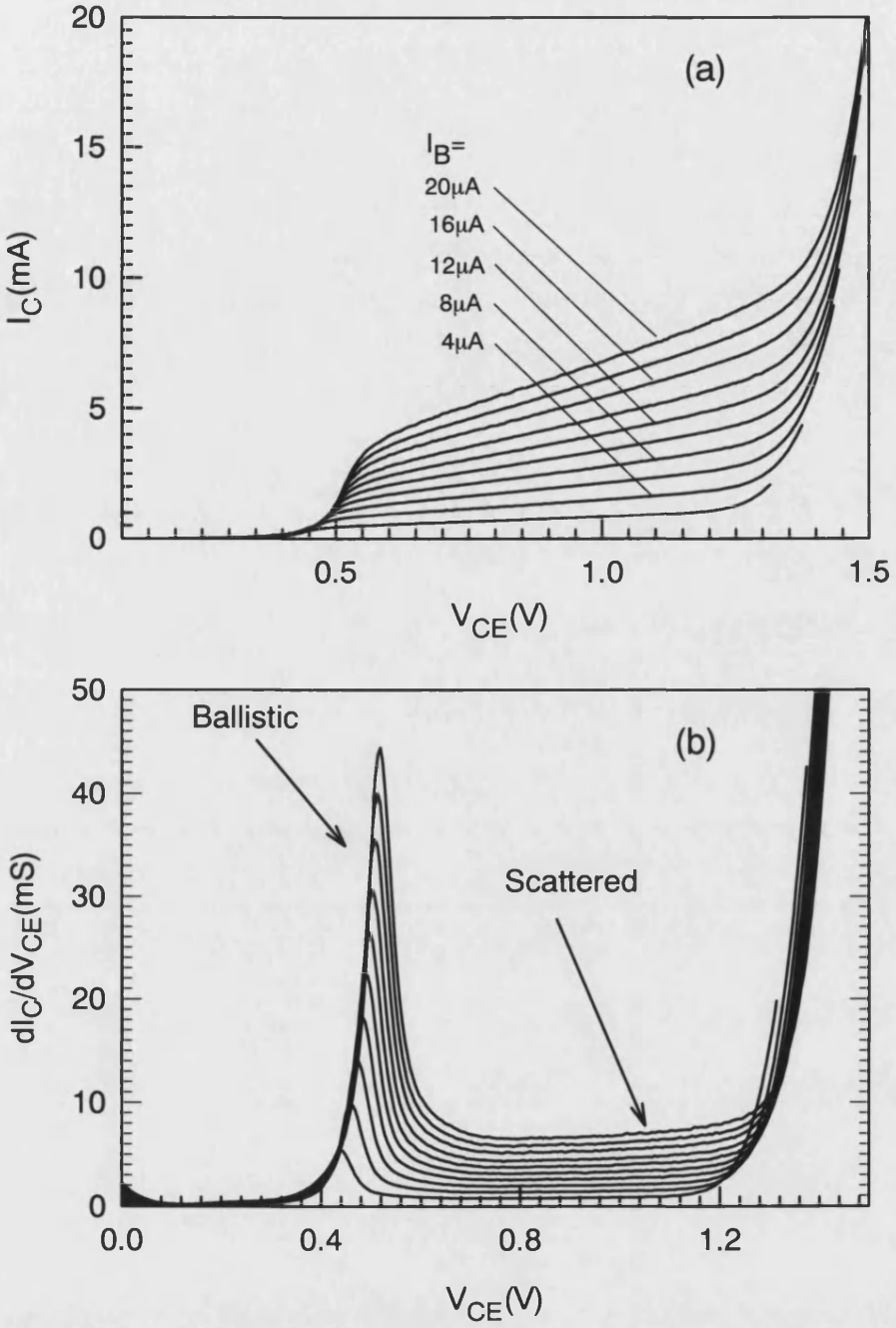

Fig. 7.18 Common-emitter (a) current-voltage and (b) transconductance-voltage characteristics of the $Al_{0.5}Ga_{0.5}As$ emitter barrier transistor (NU1223/B) for injection currents from 2μA to 20μA in 2μA intervals measured at ambient pressure and 8K.

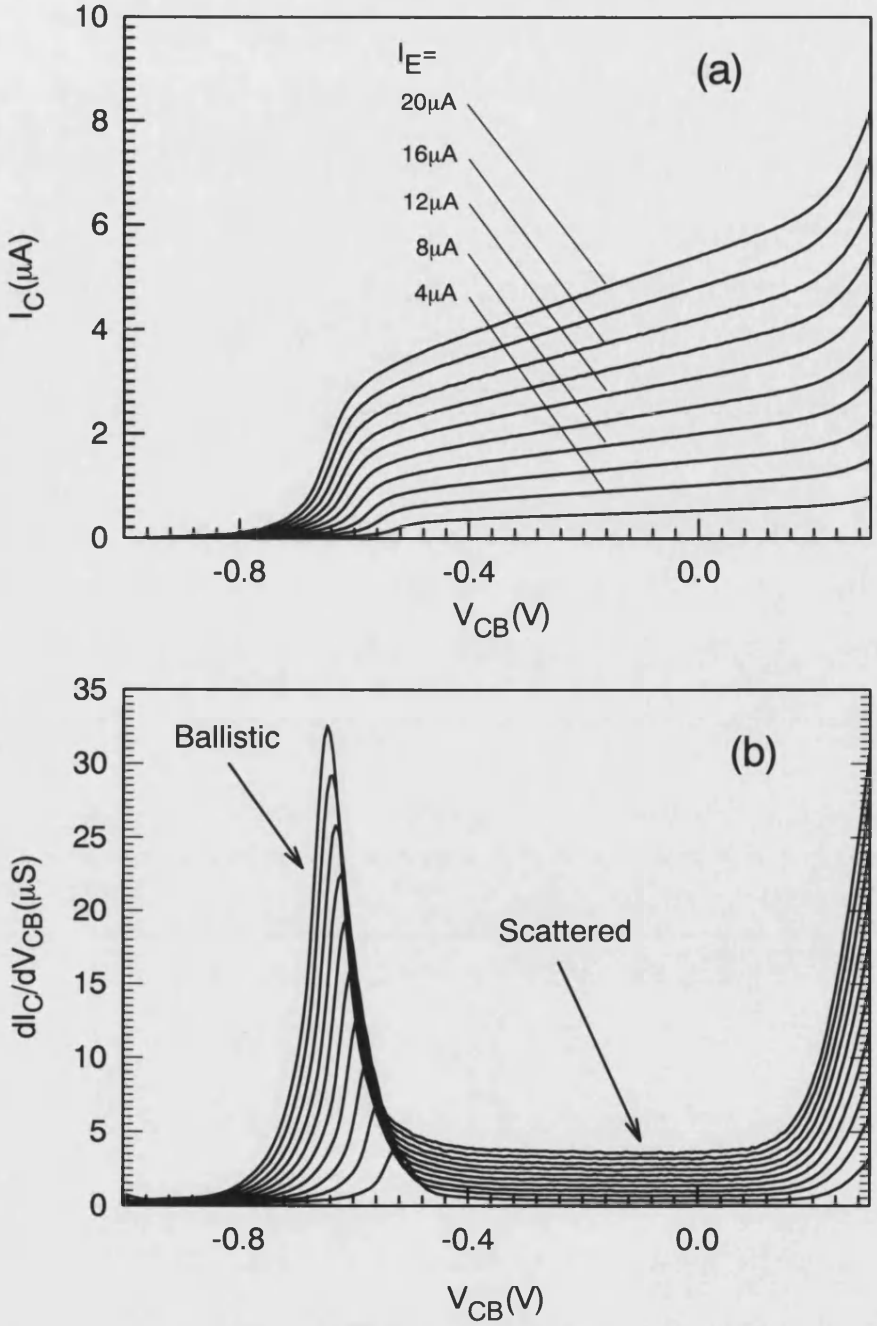

Fig. 7.19 Two-point common-base (a) current-voltage and (b) transconductance-voltage characteristics of the $Al_{0.5}Ga_{0.5}As$ emitter barrier transistor (NU1223/B) for injection currents from 2μA to 20μA in 2μA intervals measured at ambient pressure and 8K.

The ballistic peaks are much larger in this transistor, and represent collection of about 30% of injected electrons with energies close to their injection energy. This is in broad agreement with the ballistic fraction of 50% observed in the transistor

with an $Al_{0.3}Ga_{0.7}As$ emitter barrier and 30nm (Heiblum *et al.* 1985a) and 50nm (Bending *et al.* 1989a) base transit region.

In Fig. 7.20 the calculated common-base transconductance spectrum corresponding to an injection energy of 300meV is shown (see section 6.4). The general shape of the modelled transconductance spectrum further confirms that the large peak in the experimentally observed transconductance spectrum is due to the collection of quasiballistic electrons. Since we neglect the scattering of electrons in our calculations, all electrons are collected within the large ballistic peak. However, in a real device electrons lose energy in the base and collector barrier and hence only a fraction (30% in our devices) of the injected electrons traverse the narrow base region ballistically.

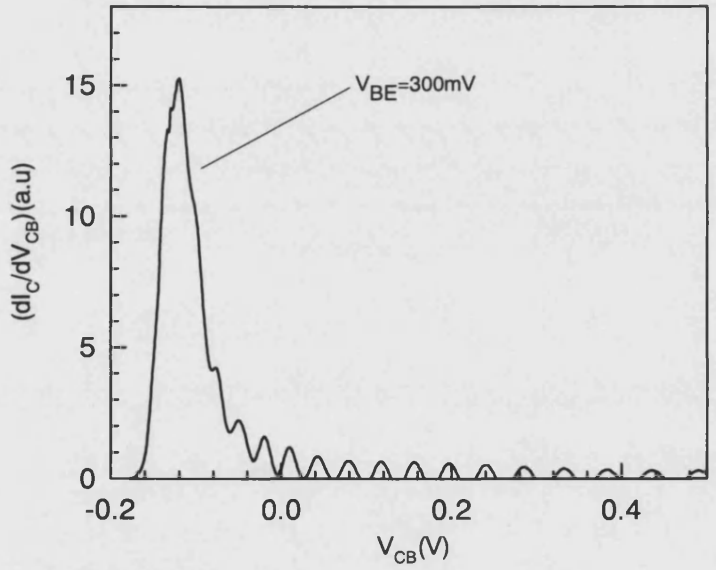

Fig. 7.20 Modelled common-base transconductance-voltage characteristics of the $Al_{0.5}Ga_{0.5}As$ emitter barrier transistor for V_{BE}=300meV.

In contrast to the AlAs emitter barrier transistor we do not see a large background of scattered electrons in the sample with an $Al_{0.5}Ga_{0.5}As$ barrier (Fig. 7.18 and Fig. 7.19) indicating that its origin lies in the transport processes through the indirect AlAs barrier.

7.3 Thermal Activation Measurements – Samples NU1224/A, NU1224/B and NU1223/B

Fig. 7.21 show three-point $\ln(I/T^2)$ versus 1/T Richardson plot for the AlAs emitter barriers of transistors NU1224/A (Fig. 7.21a) and NU1224/B (Fig. 7.21b). The current flowing through the emitter barrier at is set manually to give a voltage drop of 3mV (measured in three-point geometry) between emitter and base contacts.

We use equation 3.4.4 (the 3D Richardson law which is derived in chapter 3) to calculate the barrier height.

$$I = A^* T^2 \exp\left(-\frac{V_0 - E_F}{k_B T}\right) \tag{7.3.1}$$

$$\ln\left(\frac{I}{T^2}\right) = -\frac{V_0 - E_F}{k_B T} + Const. \tag{7.3.2}$$

The shape of Fig. 7.21a and Fig. 7.21b clearly demonstrates that tunnelling is the dominant process at temperatures up to 100K and the Richardson's law is invalid in this regime. Above 100K thermally assisted tunnelling should become important and at sufficiently high temperature the transport is dominated by thermal activation and the data can be fit to a straight line (Fig. 7.21a and Fig. 7.21b). Substituting the gradient into equation (7.3.2) we obtain barrier heights of 74meV and 78meV for NU1224/A and NU1224/B respectively which is well below the values (~130meV) reported in the literature for the Γ(GaAs)/X(AlAs) offset (for example Mendez and Chang 1990, Finley *et al.* 1998) indicating that tunnelling significantly contributes even at high temperatures. Hase *et al.* (1986) observed a similar situation in the measurement of the temperature dependence of current flowing through $Al_xGa_{1-x}As$ barriers with an AlAs mole fraction (x) of 0.32, 0.38 and 0.48. By comparing the experimentally measured current and calculated current taking the tunnelling contribution into account they reported values for the height of which was about 35meV larger than the barrier height obtained from thermal activation measurements using the Richardson law.

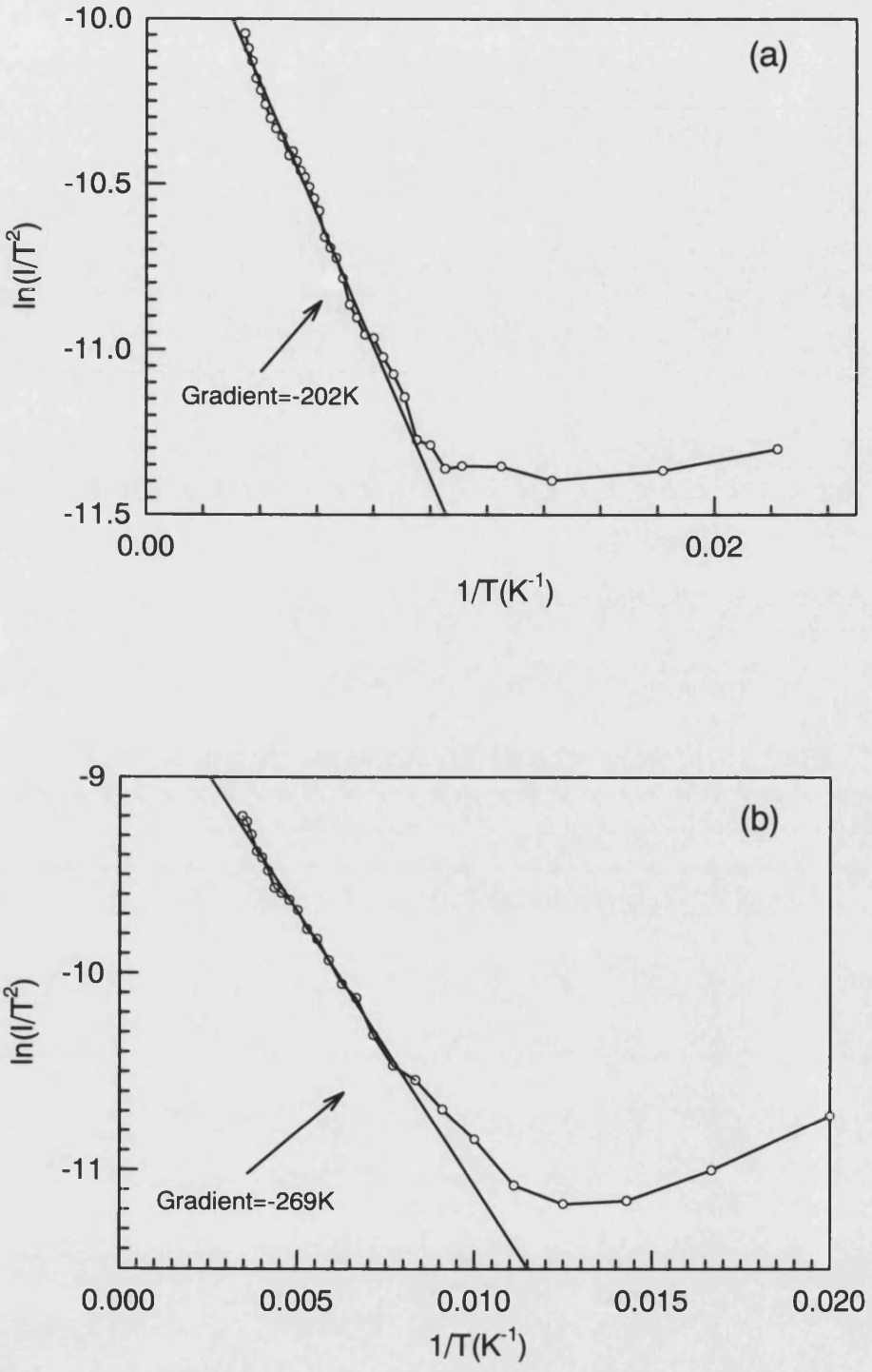

Fig. 7.21 $\ln(I/T^2)$ versus 1/T plot for device (a) NU1224/A and (b) NU1224/B (V_{BE}=3mV) at ambient pressure.

Fig. 7.22 show three-point $\ln(I/T^2)$ versus 1/T Richardson plot for the emitter barrier of the $Al_{0.5}Ga_{0.5}As$ transistor. As observed for the AlAs emitter barrier the shape of the plot displays tunnelling and thermionic regimes. By fitting a straight line to the high temperature data we obtain a barrier height about 310meV which is lower than the value reported in literature (Mendez *et al.* 1986).

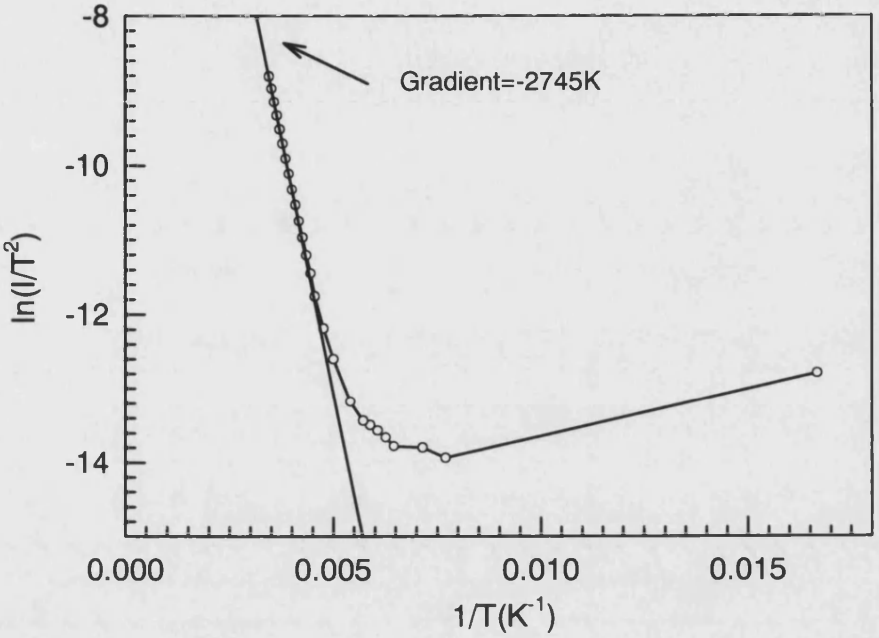

Fig. 7.22 $\ln(I/T^2)$ versus 1/T plot for device NU1223/B (V_{BE}=25mV).

We note that the three-point techniques works for $Al_{0.5}Ga_{0.5}As$ barriers at high temperature as the impedance of the barrier becomes less than the input impedance of the Nanovoltmeter (~$10^{13}\Omega$).

7.4 Hydrostatic pressure measurements – Sample NU1224/B

Since the peaks in the scattered background are most likely related to X-point transport processes, hydrostatic pressure has been applied to the devices to exploit the fact that the hydrostatic pressure reduces X(AlAs)- Γ(GaAs) conduction band offset at a rate of -11meV/kbar leaving the Γ(AlAs)-Γ(GaAs) conduction band offset unchanged (Mendez *et al.* 1986). The hydrostatic pressure measurement technique and specific pressure cell used in this work were described in chapter 5. Measurements under various values of hydrostatic pressure were performed at both 4.2K and 77K.

In this section data obtained from an AlAs emitter barrier device having emitter/base mesas of dimension 45μm×15μm (NU1224/B) will be given.

Three-point current and conductance data of the 15nm AlAs emitter barrier under different hydrostatic pressures are shown in Fig. 7.23 and Fig. 7.24. These data were obtained with the collector contact floating. Clear resonances are present in the emitter barrier conductance data at 4.2K (Fig. 7.24) which become more pronounced at high pressure and are probably signatures of sequential resonant tunnelling via X-point subbands adjacent to the emitter Fermi band in the biased structure. At 77K the resonances are smeared out due to thermal effects. Othaman *et al.* (1993) reported similar resonances in an asymmetrically doped biased 4nm AlAs single barrier structure under hydrostatic pressure.

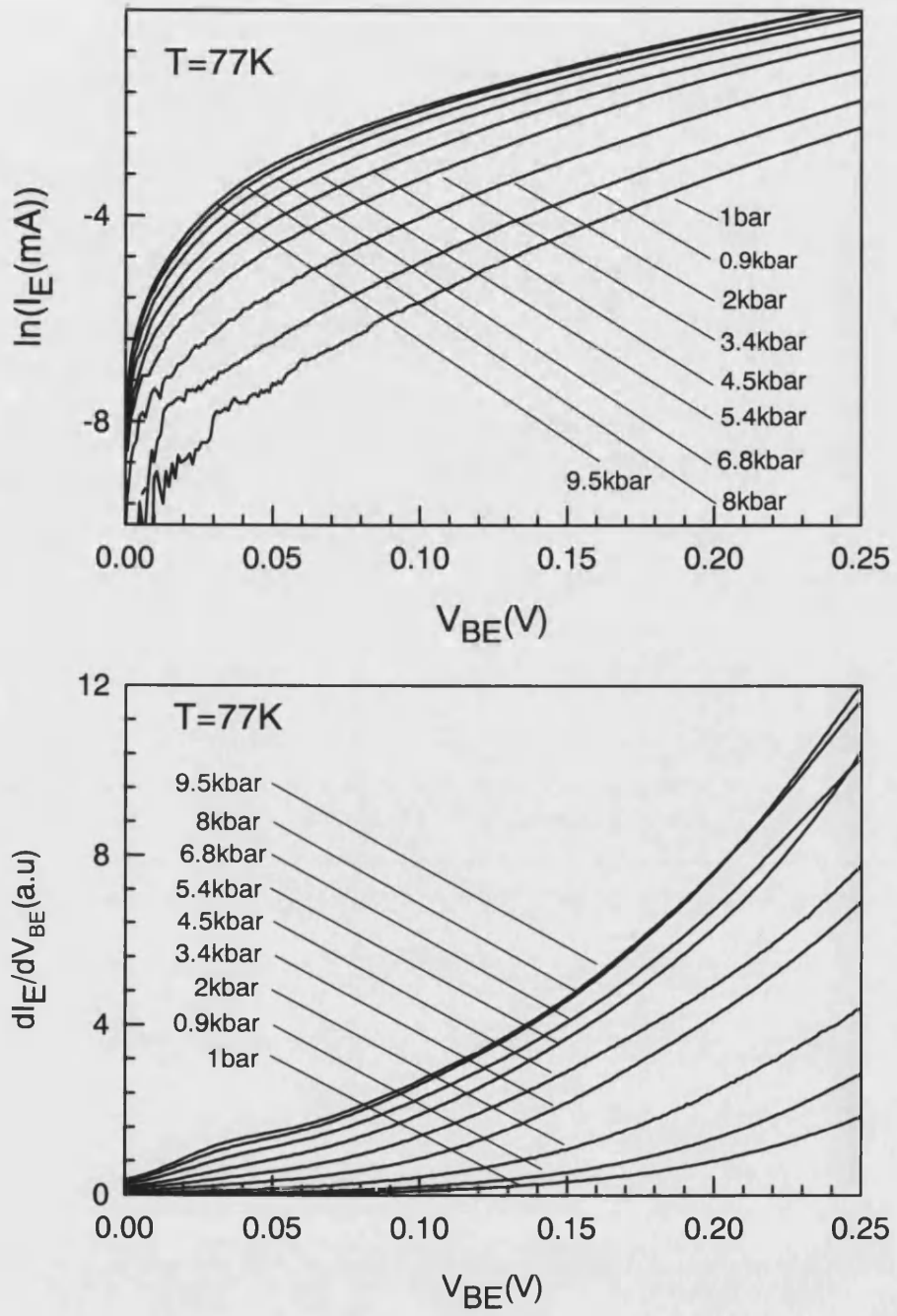

Fig. 7.23 (a) Three-point log(current)-voltage and (b) conductance-voltage characteristics of AlAs emitter barrier measured at 77K under various hydrostatic pressures.

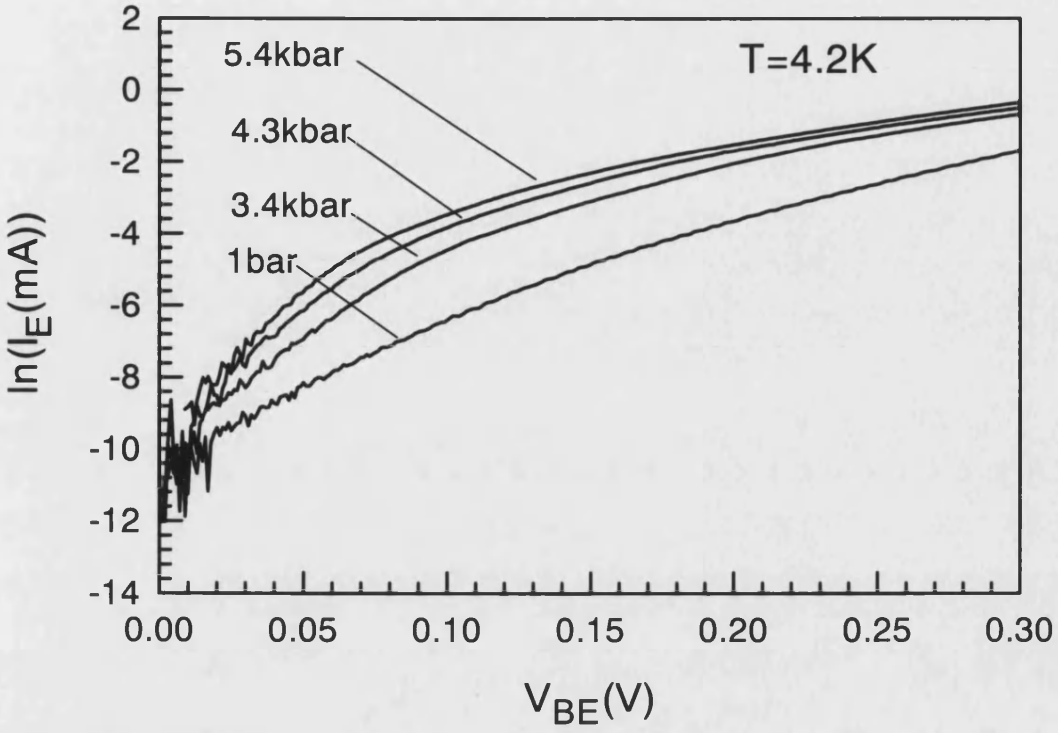

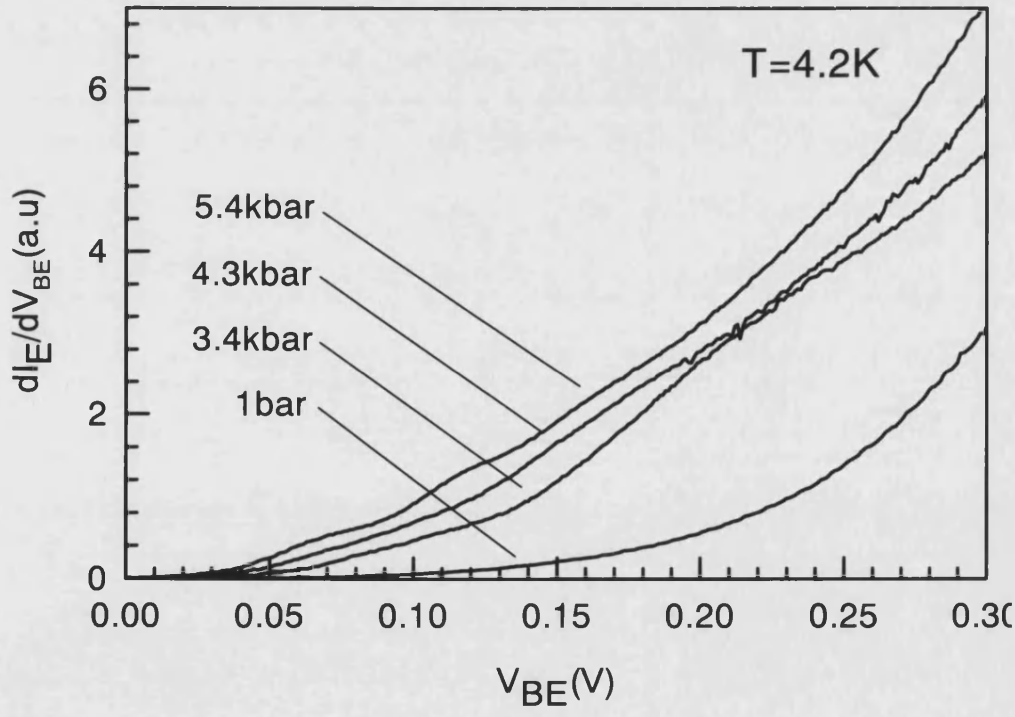

Fig 7.24 (a) Three-point log(current)-voltage and (b) conductance-voltage characteristics of the AlAs emitter barrier measured at 4.2K under various hydrostatic pressures.

In Fig 7.25 a plot of logI against pressure for different values of emitter-base bias is shown.

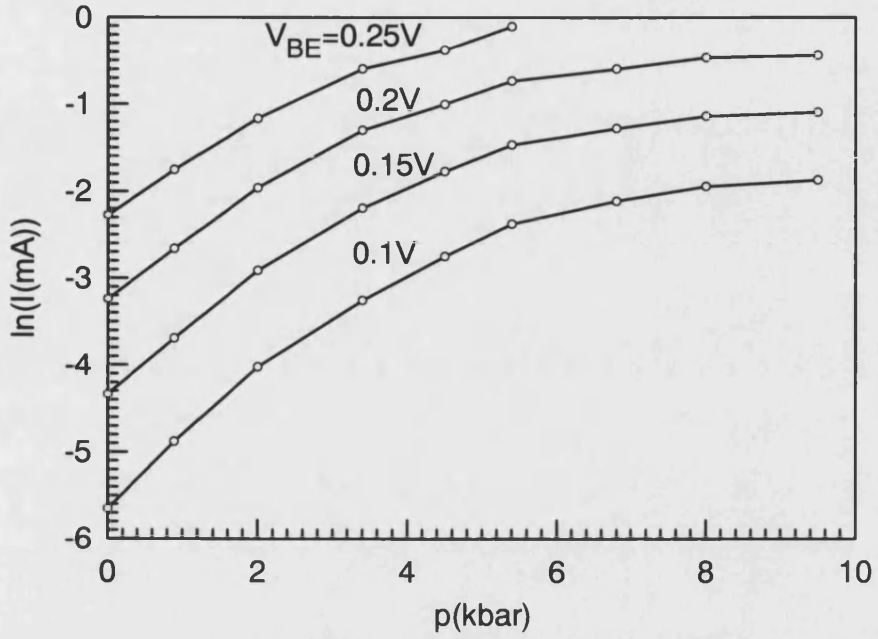

Fig. 7.25 logI versus applied hydrostatic pressure plotted for different values of V_{BE} at 77K.

The exponential increase of current with increasing pressure confirms that X-point related transport dominates in these barriers. Above 6kbar the current is only weakly dependent on pressure suggesting that emitter Fermi level now lies above the X-point in the AlAs layer .

Fig. 7.26 shows common-emitter transconductance plots at 77K for different values of pressure and an injection voltage of 225mV. The transconductance data are normalised by the corresponding injection currents. We see that the quasiballistic peak diminishes for pressures above 2kbar which coincides with the emergence of a second lower energy peak (see Fig. 7.26b). Transconductance spectra collected at 4.2K (Fig. 7.27) also display a similar behaviour. We attribute this to the real space transfer of electrons into one of the X-point bound states adjacent to the emitter Fermi band at this bias. This process will become dominant above pressures such

that the top of the X-point barrier falls below the emitter Fermi level at this bias. These transferred electrons then can tunnel out at a well defined but lower energy (Fig. 7.28). Mendez and Chang (1990) and Austing *et al.* (1993) reported transfer of electrons into X-point subbands in a double barrier resonant tunnelling structure under hydrostatic pressure.

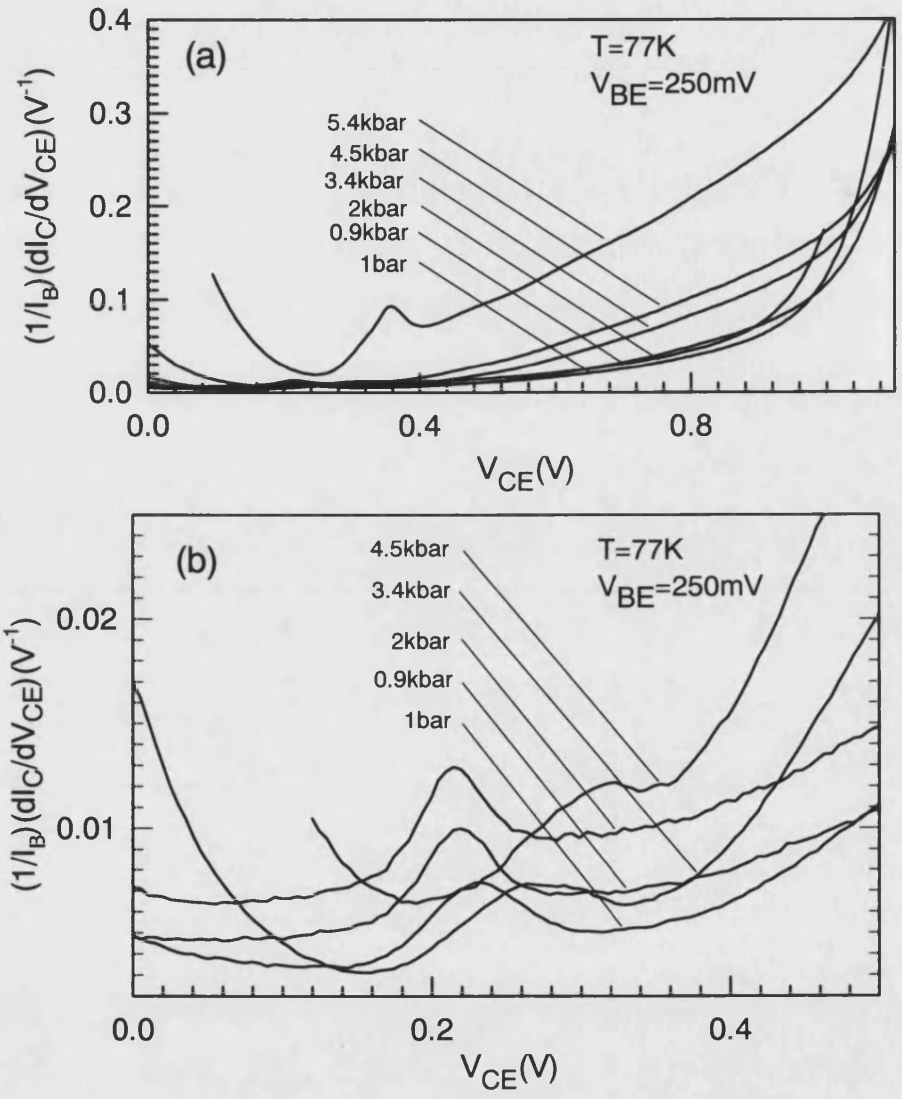

Fig. 7.26 (a) Common-emitter transconductance-voltage characteristics of an AlAs emitter barrier transistor (NU1224/B) normalised by the base current for different values of pressure for an injection voltage of 250mV measured at 77K. (b) the same plot on an expanded scale.

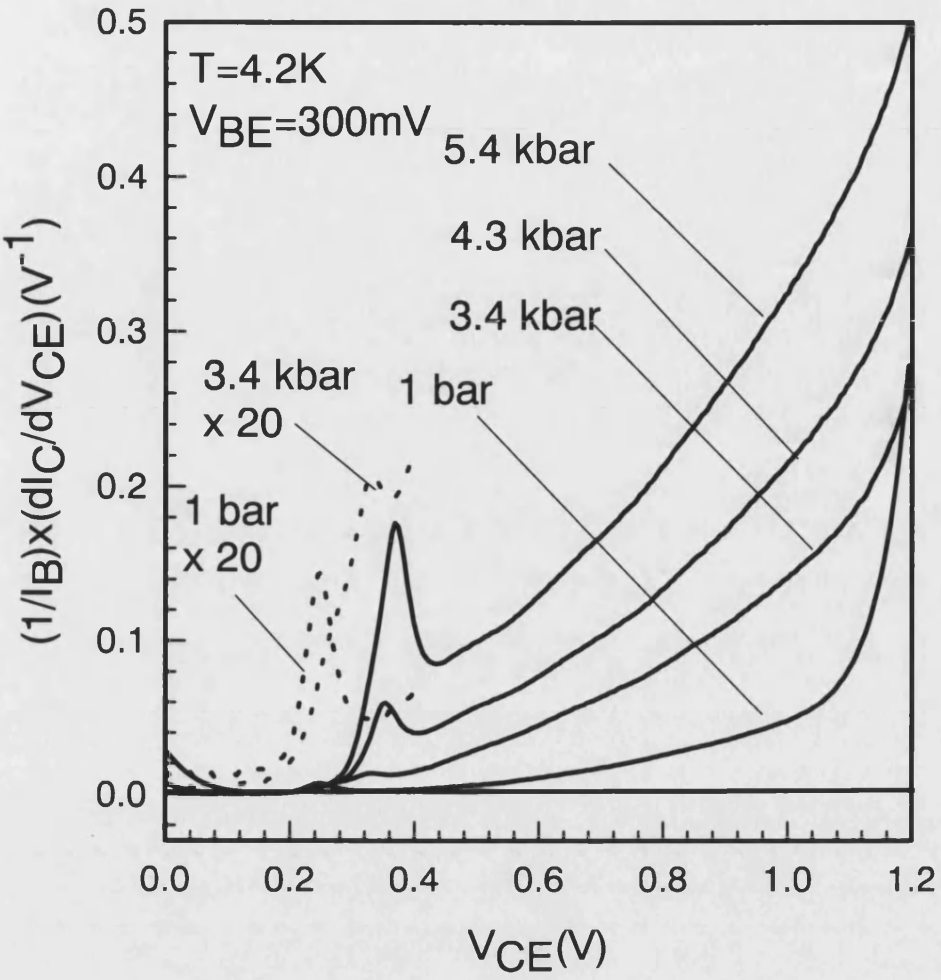

Fig. 7.27 Common-emitter transconductance of an AlAs emitter barrier transistor (NU1224/B) normalised by the base current for different hydrostatic pressures (V_{BE}=300mV) at T=4.2K.

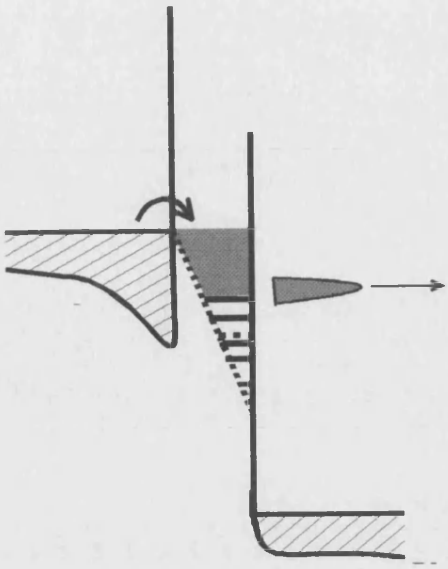

Fig. 7.28 Schematic diagram of real space transfer and re-emission of electrons.

Three-point common-base transconductance data and its derivative under various hydrostatic pressures (V_{BE}=300mV) measured at 4.2K are plotted in Fig. 7.29. Clear peaks are visible in the scattered background. One would expect that the peaks in the scattered background should shift towards lower energy with increasing hydrostatic pressure due to the reduction of the X-point conduction band minima. Othaman *et al.* (1993) observed pressure-induced shift of X-point related resonances in a 4nm AlAs single barrier structure with a 2D emitter region. In our measurements we were not able to identify any systematic pressure-induced shifts of the peaks (Fig. 7.30). However the accumulation of electrons at the X-point quantum well can substantially modify the band structure and hence the positions of the X-point subband edges relative to the emitter Fermi band (Carbonneau *et al.* 1993) making analysis rather complex.

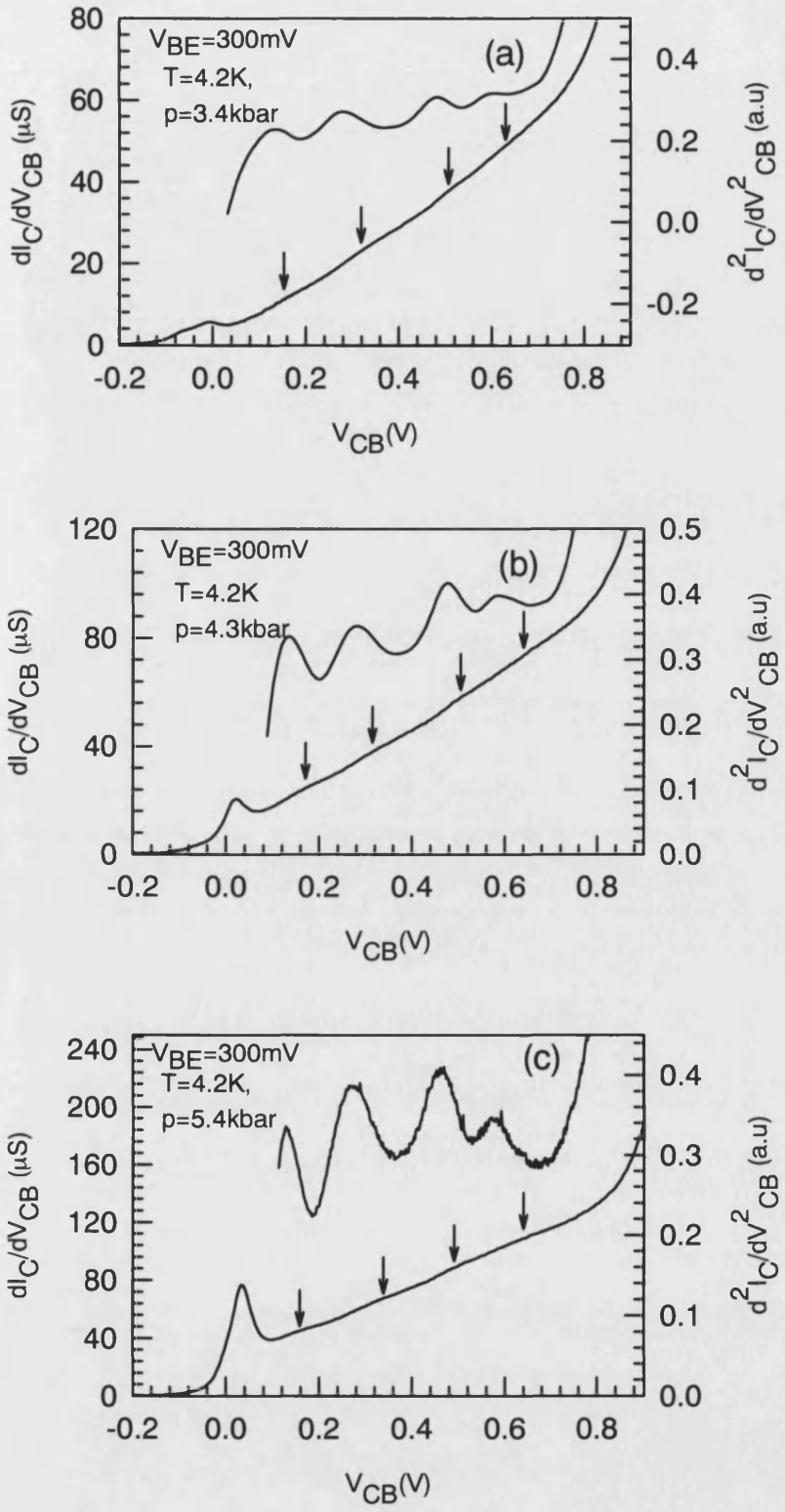

Fig. 7.29 Three-point common-base transconductance and its derivative for the transistor with an AlAs emitter barrier measured at different values of pressure (V_{BE}=300mV, T=4.2K).

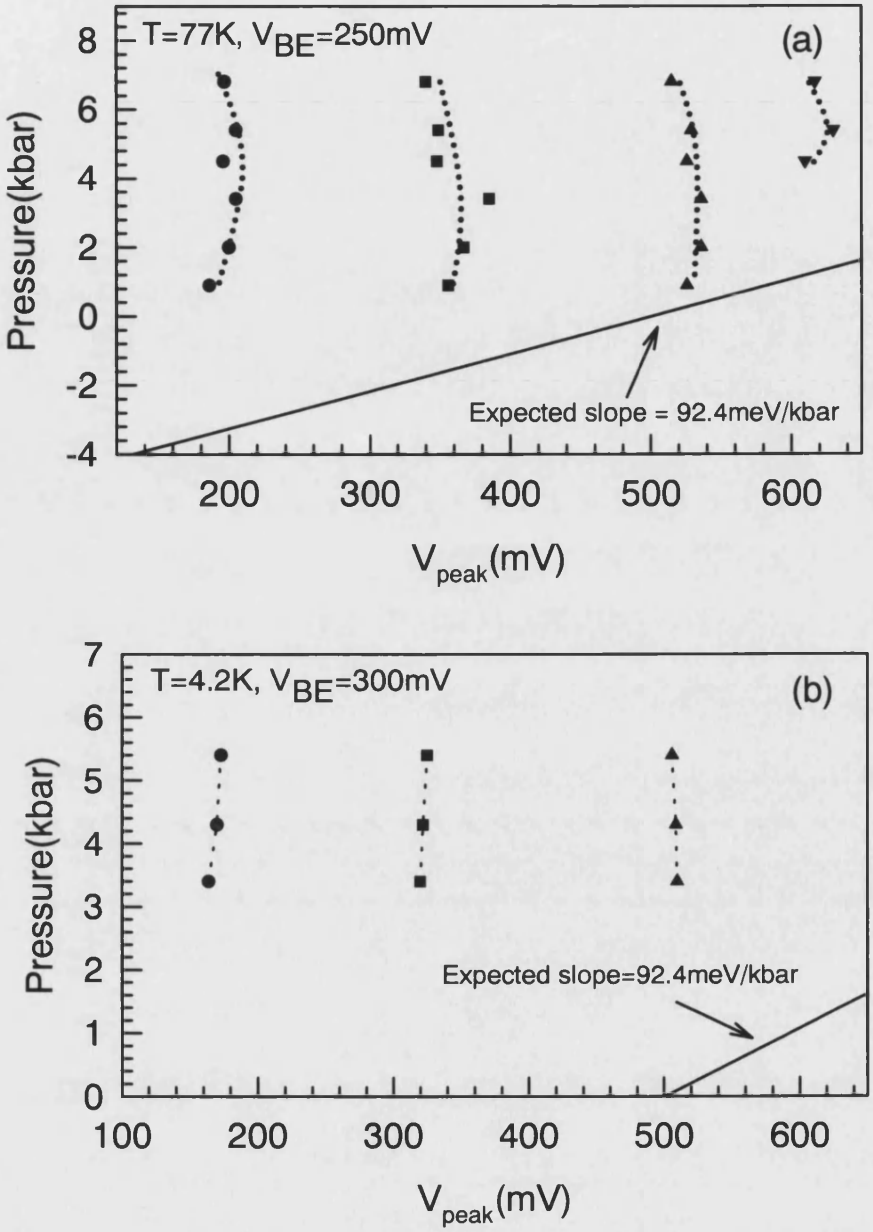

Fig. 7.30 Peak positions versus pressure plot for transistor with AlAs emitter barrier measured at (a) 77K and (b) 4.2K.

7.5 Analysis and Discussions

Given that there is clear evidence for real space transfer of charge into the barrier it seems likely that the peaks in the background of scattered electrons correspond to electrons that have cascaded down the ladder of X-point subbands and subsequently been emitted into the base layer. Finley *et al.* (1998) have recently reported intervalley relaxation of transferred electrons within 4nm AlAs barrier using electroluminescence. The dominance of cascading relaxation down through the X-point subbands is due to a longer tunnelling out time than the intervalley relaxation time (Finley *et al.* 1998).

The peaks in the scattered electron distribution at ambient pressure have been analysed in more detail in order to confirm the speculated barrier relaxation in our sample. Fig. 7.31 shows the three-point common-base tranconductance data at ambient pressure for an injection energy of 300meV as well as its derivative which aids identification of the features.

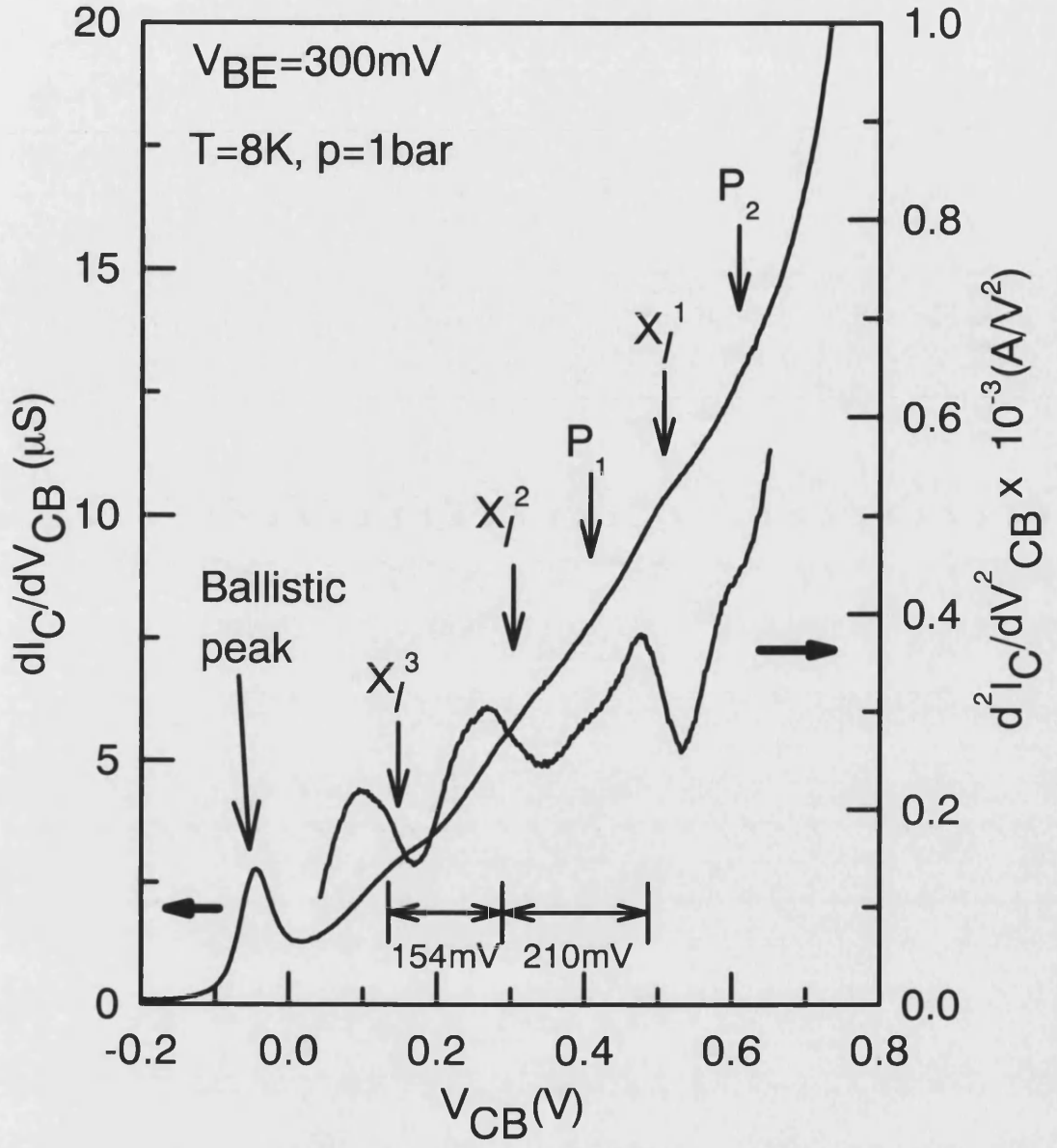

Fig. 7.31 Three-point common-base transconductance and its derivative for the transistor with an AlAs emitter barrier measured at ambient pressure and T=8K (V_{BE}=300mV).

Three clear peaks labelled X_l^1, X_l^2, X_l^3 can be identified as well as weaker shoulder structures labelled P_1 and P_2. In order to compare these positions with those of the X-point subbands the latter have been calculated for our biased 15nm AlAs barrier using exact Airy function solutions of the Schrödinger equation. Band bending at the interfaces has been accounted for using a classical solution of the Poisson equation in these regions. Details of these calculations were given in chapter 6. Fig.7.32 illustrates the calculated positions of the X-point subbands relative to the emitter Fermi energy for an applied bias of 300mV. Using our 7.7 lever rule we find reasonable agreement between the calculated spacings of the first three longitudinal subbands $(X_l^3 - X_l^2 = 26meV, X_l^2 - X_l^1 = 31meV)$ and the experimentally measured peaks with the same labels $(X_l^3 - X_l^2 = 154/7.7 = 20meV$ $, X_l^2 - X_l^1 = 210/7.7 = 27meV)$.

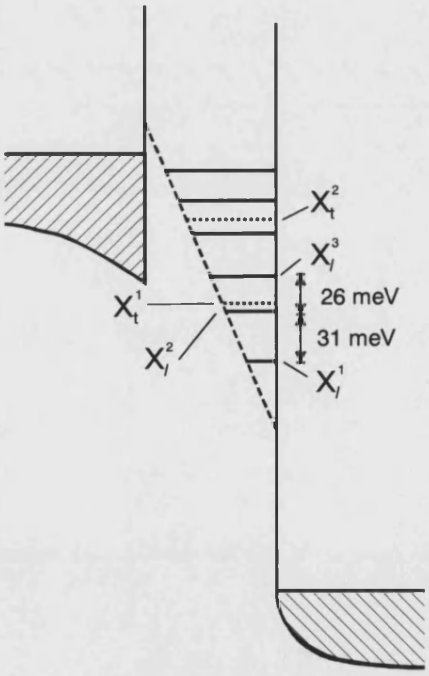

Fig 7.32 Calculated band structure of the emitter barrier and X-point subbands edges at a bias of 300mV.

We are unable to directly relate any of the structures to transverse X-point subbands and presume that these make a much smaller contribution to the current due to the need for a large momentum scattering event out towards the Brillouin zone boundary. The two additional structures P_1 and P_2 (see Fig. 7.31) could, however, possibly represent phonon replicas of peaks emitted from these transverse X-point subbands.

Chapter 8

Conclusions and Future Suggestions

8.1 Conclusions

We have successfully fabricated two types of tunnelling hot electron transistor which are identical except for the composition of the 15nm $Al_xGa_{1-x}As$ emitter barrier; one where transport is dominated by the X-point minima (x=1) and a second more conventional case (x=0.5) where the Γ-point minimum dominates. By defining two separate base contacts we have been able to perform novel three-point measurements in order to eliminate series resistances at the base contacts.

Hot electron spectra collected from the $Al_{0.5}Ga_{0.5}As$ emitter barrier device demonstrate quasiballistic transport of the injected hot electrons through the narrow base region. We estimate that about 30% of the injected electrons are collected with energies close to their injection energies. The general shape of the hot electron spectrum is in reasonable agreement with the modelled spectrum when the scattering of electrons in the doped Base layer is neglected.

In stark contrast hot electron spectroscopy of the 15nm AlAs emitter barrier transistor displays a tiny ballistic fraction (1%) of injected electrons. We also see a large scattered background which increases rapidly towards low energies and contains well defined peaks. These are not present in the device with $Al_{0.5}Ga_{0.5}As$ emitter barrier demonstrating that the majority (99%) of carriers passing through the barrier have suffered substantial inelastic scattering.

From measurements under hydrostatic pressure on the AlAs emitter transistor we find clear evidence of real space transfer of electrons from the emitter electrode into X-point bound states in the barrier adjacent to the Fermi band. These electrons subsequently relax down through the ladder of X-point subbands and are re-emitted at these well-defined energies. The electrons seem to be re-emitted from longitudinal X-point subbands and appear as clear peaks in the large background of scattered electrons. We also see two additional weak structures which could possibly represent phonon replicas of peaks emitted from the transverse X-point subbands.

We find reasonable quantitative agreement between the peaks measured in the scattered electron distribution at ambient pressure and the calculated positions of the lowest energy longitudinal X-point subbands in the AlAs barrier.

8.2 Future Suggestions

A major factor which affects the yield of working transistors is the need to make shallow Ohmic contacts to the buried base layer. In the work reported in this thesis we overcame this problem by defining three emitter mesas, two of which were used as base contacts in three-point measurement to eliminate the series resistance to base. This approach is however not appropriate for the large scale production of devices and failed with the $Al_{0.5}Ga_{0.5}As$ barrier device at low temperatures. Another factor that affects the yield is exposing the buried base layer by selective etching. These two difficulties can be overcome by using *in-situ* implantation during MBE growth to isolate the base contact layer and the emitter as illustrated in Fig. 8.1 (Kaya *et al.* 1996). This would make the fabrication and data analysis much more straight forward.

Due to the grading of the collector barrier it is difficult to interpret the features in the transconductance spectrum in the forward biased region. We have used a simple lever rule to scale the transconductance spectra to the correct energies. Reducing the barrier height of the high-pass collector barrier will allow one to observe the peaks in the scattered spectrum in the reversed biased region of the

collector barrier. Also we should be able to resolve the LO phonon replicas which arise in the base region (Heiblum *et al.* 1989).

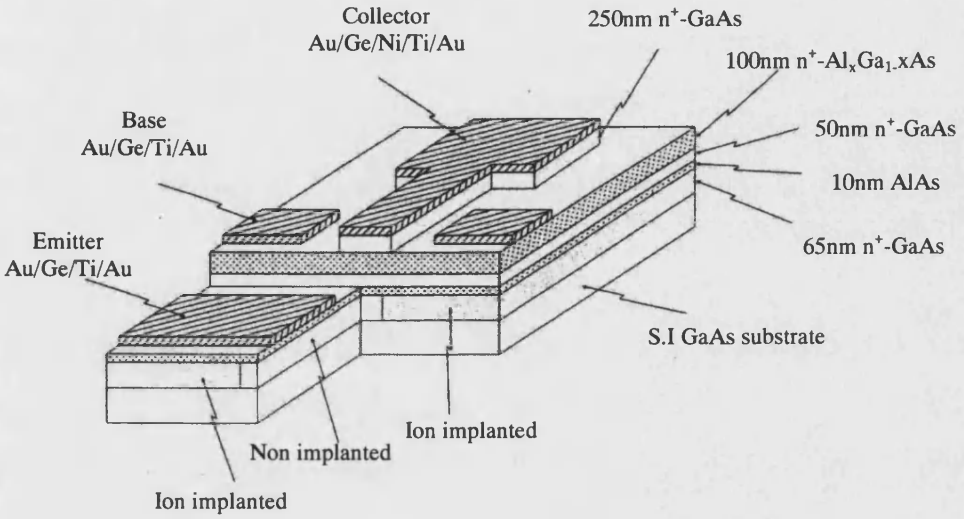

Fig. 8.1 Schematic diagram of transistor structure showing the epilayer sequences and location of ion implantation regions (Kaya *et al.* 1996).

The presence of a large number of X-point subbands within 15nm AlAs barrier makes the analysis rather complex especially at high pressure. Using thinner barriers (for example 10nm thick) it may be possible to observe the expected pressure-induced shift of the resonances in the transcondutance-voltage characteristics of the THETA device. Also, with a suitable choice of AlAs mole fraction (x) the number of subbands which influence the transport processes through $Al_xGa_{1-x}As$ emitter barrier at a given bias can be reduced.

The fact that the majority of electrons relax in energy down through the ladder of X-point subbands may be utilised to make a source of terahertz radiation if non-radiative transitions can be suppressed. The separation between the X-point subbands can be engineered by changing the barrier width or using different AlAs compositions.

The width of the injected electron distribution can be made narrower by using a two-dimensional (2D) emitter electrode where 2D subbands are formed in the accumulation region. By biasing the AlAs emitter barrier is in such a way that the subbands in the accumulation region are in resonance with one of the X-point subbands within the barrier the relative importance of resonant tunnelling between 2D subbands and relaxation of electrons within the barrier can be investigated.

Appendix A

Simulation of I-V characteristics of the THETA device

```
c    subroutines from Numerical Recipes in Fortran are acknowledged
     implicit none
c    ** data elements **
     double precision Eb, Ec, Eint, ss, t1, t2, logt1, logt2, a,
    :    b, epsr, result, kx, Vbe, Vcb, Ef, Efin,  Vibe, Vicb,
    :    Vcbm, Vfbe, Vfcb,h,pi,ele,mres,mGaAs,hbar,d,tem1,tem2,c,
    :    result1
     integer ns, j, m, option
     common /block1/ Ef, kx, Vbe, Vcb
     parameter (h=6.626d-34,pi=3.141592654d0, ele=1.602d-19,
    : mres=9.109d-31)
c    ** executable statements **

c    *** program menu ***
     print *,' '
     print *,' '
     print *,' '
     print *,' '
     print *,'                ** THETA model **'
     print *,' '
     print *,' '
     print *,'                  PROGRAM OPTIONS'
     print *,' '
     print *,'          (1) Emitter-base barrier: log T(E) plot'
     print *,' '
     print *,'          (2) Base-collector barrier: log T(E) plot'
     print *,' '
     print *,'          (3) Ic-Vcb plot (Veb fixed)'
     print *,' '
     print *,'          (4) Ic-Veb plot (Vcb fixed)'
     print *,' '
     print *,'          (5) Ie-Vbe plot'
     print *,' '
     print *,'          (6) Exit'

     print *,'option?'
     read *, option
     if (option.eq.1) then
       print *, 'Enter input parameters >>>>>>>>'
       print *, 'Vbe<V>?'
       read *, Vbe
       print *, 'Initial value of E<V>?'
       read *, Eint
```

```
      print *, 'Final value of E<V>?'
      read *, Efin
      print *, 'Number of steps?'
      read *, ns
      open(1,file='logt1.dat')
      ss = (Efin-Eint)/ns
      do 100, j = 0, ns, 1
        Eb = Eint+(j*ss)
        call tr1(Eb,t1)
        logt1 = log(t1)
        print *, Eb, logt1
        write(1,500) Eb,logt1
100   continue

      print *,' '
      print *,' '
      print *, '          Run complete!'
      print *,' '
      print *, 'Input parameters >>>>>>>>'
      print *,' '
      print *, 'Vbe<V> =', Vbe
      print *, 'Initial value of E<V> =', Eint
      print *, 'Final value of E<V> =', Efin
      print *, 'Step size =', ss
      print *, 'Number of steps =',ns
      print *, 'filename: logt1.dat'

    elseif (option.eq.2) then
      print *,'Enter Input parameters >>>>>>>>'
      print *, 'Vcb<V>'
      read *, Vcb
      print *, 'Initial value of E<V>?'
      read *, Eint
      print *, 'Final value of E<V>?'
      read *, Efin
      print *, 'Number of steps?'
      read *, ns
      open(2,file='logt2.dat')
      ss = (Efin-Eint)/ns
      do 200, j = 0, ns, 1
        Ec = Eint+(j*ss)
        call tr2(Ec,t2)
        logt2 = log(t2)
        print *, Ec, logt2
        write(2,500) Ec,logt2

200   continue

      print *,' '
      print *,'          Run complete!'
      print *,' '
      print *,'Input parameters >>>>>>>>'
      print *,' '
      print *,'Initial value of E<V> =', Eint
      print *,'Final value of E<V> =', Efin
      print *,'Step size<V> =', ss
      print *,'Number of steps =', ns
```

```
      print *,'Filename: logt2.dat'

    elseif (option.eq.3) then
      print *,'Enter input parameters >>>>>>>>'
      print *, 'Vbe<V>?'
      read *, Vbe
      print *, 'Initial value of Vcb<V>?'
      read *, Vicb
      print *, 'Final value of Vcb<V>?'
      read *, Vfcb
      print *, 'Number of steps?'
      read *, ns
      open(3,file='iv2data.dat',STATUS='NEW')

c     *** STEP 1: evaluate k(Vbe) ***
      Ef = 0.055d0
      a = 1.d-10
      b = Ef - 1.d-10
      epsr = 1.00d-3
      m=1
      call qtrap(m,a,b,epsr,result)
      kx = 1.00d0/result
      ss = (Vfcb-Vicb)/ns

c     *** STEP 2: Integrate kx*(Ef-E)*t1*t2 for fixed Vbe ***
      do 300, j = 0, ns, 1
        Vcb = Vicb+(j*ss)
        Vcbm=(Vcb**2.d0)**0.5d0
        if(Vcbm.lt.0.0001d0)then
          goto 300
        endif
        a=Vbe+1.d-10
        b = Ef + Vbe - 1.d-10
        epsr = 1.00d-3
        m=2
        call qtrap(m,a,b,epsr,result)
        print *, Vcb, result
        write(3,500) Vcb, result
300     continue

      print *,' '
      print *,'          Run complete!'
      print *,' '
      print *,'Input parameters >>>>>>>>'
      print *,' '
      print *,'Vbe<V> =', Vbe
      print *,'Initial value of Vcb<V> =', Vicb
      print *,'Final value of Vcb<V> = ',Vfcb
      print *,'Step size<V> =', ss
      print *,'Number of steps =', ns
      print *,'Filename: iv2data.dat'

    elseif (option.eq.4) then
      print *, 'Enter input parameters >>>>>>>>'
      print *, 'Vcb<V>?'
      read *, Vcb
      print *, 'Initial value of Vbe<V>?'
```

```
      read *, Vibe
      print *, 'Final value of Vbe<V>?'
      read *, Vfbe
      print *, 'Number of steps?'
      read *, ns
      open(4,file='iv2data.dat')

c     *** STEP 1: evaluate k(Vbe) ***
      Ef = 0.055d0
      ss = (Vfbe-Vibe)/ns
      do 400, j = 0, ns, 1
        Vbe = Vibe+(j*ss)
        a = 1.d-10
        b = Ef-1.d-10
        epsr = 1.00d-3
        m=1
        call qtrap(m,a,b,epsr,result)
        kx = 1.00d0/result

c     *** STEP 2: Integrate kx*(Ef-E)*t1*t2 for a fixed Vcb ***
        a = Vbe +1.d-10
        b = Ef + Vbe -1.d-10
        epsr = 1.00d-6
        m=2
        call qtrap(m,a,b,epsr,result)
        print *, Vbe, result
        write(4,500) Vbe, result
 400    continue

      print *,' '
      print *,'          Run complete!'
      print *,' '
      print *,'Input parameters >>>>>>>>'
      print *,' '
      print *,'Vcb<V> =', Vcb
      print *,'Initial value of Vbe<V> =', Vibe
      print *,'Final value of Vbe<V> =', Vfbe
      print *,'Step size<V> =', ss
      print *,'Number of steps =',ns
      print *,'Filename: iv2data.dat'

    elseif (option.eq.5) then
      print*,'Initial value of Vbe?'
      read*,Vibe
      print*,'Final value of Vbe?'
      read*,Vfbe
      print*,'Number of steps?'
      read*,ns
      open(5,file='IeVeb.dat')
      ss=(Vfbe-Vibe)/ns
      Ef=0.055d0
      hbar=h/(2.d0*pi)
      mGaAs=0.067d0*mres
      d=(mGaAs*ele)/(2*pi*pi*(hbar**3))

      do 450, j=0,ns,1
        Vbe=Vibe+(j*ss)
```

```
      if (Vbe.gt.Ef) then
        a=1.0d-10
        b=Ef-1.0d-10
        epsr=1.0d-3
        m=1
        call qtrap(m,a,b,epsr,result)
      else
        a=1.0d-10
        b=Ef-Vbe-1.0d-10
        c=Ef-1.0d-10
        epsr=1.0d-3
        m=3
        call qtrap(m,a,b,epsr,result)
        tem1=result*Vbe
        m=1
        call qtrap(m,b,c,epsr,result)
        tem2=result
        result=tem1+tem2
      endif

      result1=d*result*ele*ele*1.0d-4
      write(5,500)Vbe,result1
      print*,Vbe,result1
450   continue

    print*,''
    print*,''
    print*,'          Run complete!'
    print*,''
    print*,'Input parameters >>>>>>>>>>>>>'
    print*,''
    print*,'Initial value of Vbe<V>=',Vibe
    print*,'Final value of Vbe<V>=',Vfbe
    print*,'Step size<V>=',ss
    print*,'Number of steps=',ns
    print*,'Finename:IeVbe.dat'

  elseif (option.eq.6) then
    goto 800
  endif


500 format(e10.4,t15,e10.4)

800 end


c  ************************************************************************

  function f1(E)
  double precision f1, E, Ef, t1, Vbe, Vcb, kx
  common /block1/ Ef, kx, Vbe, Vcb
  call tr1(E,t1)
  f1 = (Ef-E)*t1
  return
  end
```

```
      function f2(E)
      double precision f2, E, Ef, Eb, t1, t2, Vbe, Vcb, kx
      common /block1/ Ef, kx, Vbe, Vcb
      Eb = E - Vbe
      call tr1(Eb,t1)
      call tr2(E,t2)
      f2 = kx*(Ef-(E-Vbe))*t1*t2
      return
      end

      function f3(E)
      double precision f3,E,Ef,t1,Vbe,Vcb,kx
      common /block1/Ef,kx,Vbe,Vcb
      call tr1(E,t1)
      f3=t1
      return
      end

c     ************************************************************************
c     ** Emitter barrier transmission coefficient subroutine **

      subroutine tr1(Eb,t1)
      implicit none
c     ** data elements **
      double precision alpha, beta, V0, Vbe, k1, k3, Vcb,
     :    F, g1b, g2, g3, b(1:2,1:2), c(1:2,1:2), kx,
     :    bar, t1, equ1, equ2, equ3, mGaAs, mAlGaAs, mbzx,
     :    invc(1:2,1:2), a(1:2,1:2), z, x, kappa, gamma,
     :    mrest, ele, Ef, h, pi, hbar, Eb
      parameter(h=6.626d-34, pi=3.141592654d0, ele=1.602d-19)
      common /block1/ Ef, kx, Vbe, Vcb

c     ** input parameters **
      hbar = h/(2.00d0*pi)
      mrest = 9.109d-31
      mGaAs = 0.067d0
      mAlGaAs = 0.105d0
      V0 = 0.353d0
      bar = 15.00d0
      alpha = 1.00d0/3.00d0
      beta = mGaAs/mAlGaAs

c     ***** Executable statements ******

      kappa = ((2.00d9*mrest*ele)/(hbar**2.00d0))**alpha
      gamma = ((2.00d0*mrest*ele)/(hbar**2.00d0))**0.50d0

c     ** calculate k1 and k **

      k1 = gamma*((mGaAs*Eb)**0.50d0)
      k3 = gamma*((mGaAs*(Eb+Vbe))**0.50d0)

c     *** calculate transfer matrix ***

      F = Vbe/bar
      g1b = kappa*1.00d-9*((mAlGaAs*F)**alpha)
      mbzx = -1.00d0*kappa*((mAlGaAs*F)**alpha)*beta
```

```
c    ** Define matrix S2(x=0) **

     x = 0.00d0
     g2 = ((V0-Eb)/F) - x
     z = g1b*g2
     call matairy(z,mbzx,b)

c    ** Define matrix invS2(x=b) and multiply matrices **

     x = bar
     g3 = ((V0-Eb)/F) - x
     z = g1b*g3
     call matairy(z,mbzx,c)
     call inmat(c,z,invc)
     call mulmat(b,invc,a)

c    ** Evaluate t1 **

     equ1 = (4.00d0*k3)/k1
     equ2 = (a(1,1)+(k3*a(2,2)/k1))**2.00d0
     equ3 = ((a(2,1)/k1)-(k3*a(1,2)))**2.00d0
     t1 = equ1/(equ2+equ3)

     return
     end

c    ***************************************************************************
c    ** Subroutine to call Airy function matrix elements **

     subroutine matairy(z,zx,c)
c    ** data elements **
     implicit none
     DOUBLE PRECISION z,ai,bi,aip,bip,zx,c(1:2,1:2),
    :    S17AGF,S17AHF,S17AJF,S17AKF
     INTEGER ifail
      if (z.gt.103.d0) then
        call asyairy(z,ai,bi,aip,bip)
     else
        ifail=0
        ai=S17AGF(z,ifail)
        ifail=0
        bi=S17AHF(z,ifail)
        ifail=0
        aip=S17AJF(z,ifail)
        ifail=0
        bip=S17AKF(z,ifail)
     endif

     c(1,1)=ai
     c(1,2)=bi
     c(2,1)=aip*zx
     c(2,2)=bip*zx
     return
     end
```

```
c   ************************************************************************
c   ** Matrix multiplication subroutine **

    subroutine mulmat(b,c,b1)
c   * local arrays *
    double precision b1(1:2,1:2), b(1:2,1:2), c(1:2,1:2)
c   * parameters *
    integer j, k, l

c   ** executable statements **
    do 35 k = 1, 2, 1
      do 25 l = 1, 2, 1
        b1(k,l) = 0.00d0
        do 15 j = 1, 2, 1
          b1(k,l) = b1(k,l) + (b(k,j)*c(j,l))
15      continue
25    continue
35  continue

    return
    end

c   ************************************************************************
c   ** Matrix inversion subroutine **

    subroutine inmat(c,z,invc)
c   ** local variables and arrays **
    double precision det, c(1:2,1:2), invc(1:2,1:2), z

c   ** executable statements **
    det = (c(1,1)*c(2,2))-(c(1,2)*c(2,1))
    if (det.eq.0.00d0) then
      print *, 'Matrix C has a zero determinant: z =' ,z
    endif

    invc(1,1) = c(2,2)/det
    invc(1,2) = -1.00d0*(c(1,2)/det)
    invc(2,1) = -1.00d0*(c(2,1)/det)
    invc(2,2) = c(1,1)/det

    return
    end

c   ************************************************************************
c   ** Integration subroutine **

c   subroutine from Numerical Recipes in Fortran

    subroutine qtrap(m,a,b,eps,s)
    implicit none
c   ** data elements **
    double precision a,b,s,eps,olds
    integer j,jmax,m
    parameter (jmax=14)

c   ** executable statements **
    olds=-1.d30
```

```
      if (m.eq.1) then
        do 11,j=1,jmax,1
          call trapzd1(a,b,s,j)
          if (abs(s-olds).lt.eps*abs(olds)) return
          olds=s
11      continue
      elseif(m.eq.2)then
        do 12,j=1,jmax,1
          call trapzd2(a,b,s,j)
          if (abs(s-olds).lt.eps*abs(olds)) return
          olds=s
12      continue
      elseif (m.eq.3) then
        do 13,j=1,jmax,1
          call trapzd3(a,b,s,j)
          if (abs(s-olds).lt.eps*abs(olds)) return
          olds=s
13      continue
      endif
      return
      end

      subroutine trapzd1(a,b,s,n)
      implicit none
c     ** data elements **
      double precision f1,a,b,s,sum,x,del
      integer j,it,n,tnm
      external f1
c     ** executable statements **
      if (n.eq.1) then
        s=0.5d0*(b-a)*(f1(a)+f1(b))
        it=1
      else
        tnm=it
        del=(b-a)/tnm
        x=a+0.5d0*del
        sum=0.d0
        do 11, j=1,it,1
          sum=sum+f1(x)
          x=x+del
11      continue
        s=0.5d0*(s+(b-a)*sum/tnm)
        it=2*it
      endif
      return
      end

      subroutine trapzd2(a,b,s,n)
      implicit none
c     ** data elements **
      double precision f2,a,b,s,sum,x,del
      integer j,it,n,tnm
      external f2
c     ** executable statements **
      if (n.eq.1) then
        s=0.5d0*(b-a)*(f2(a)+f2(b))
        it=1
```

```
      else
        tnm=it
        del=(b-a)/tnm
        x=a+0.5d0*del
        sum=0.d0
        do 11, j=1,it,1
          sum=sum+f2(x)
          x=x+del
 11     continue
        s=0.5d0*(s+(b-a)*sum/tnm)
        it=2*it
      endif
      return
      end

      subroutine trapzd3(a,b,s,n)
      implicit none
c     ** data elements **
      double precision f3,a,b,s,sum,x,del
      integer j,it,n,tnm
      external f3
c     ** executable statements **
      if(n.eq.1)then
        s=0.5d0*(b-a)*(f3(a)+f3(b))
        it=1
      else
        tnm=it
        del=(b-a)/tnm
        x=a+0.5d0*del
        sum=0.d0
        do 11,j=1,it,1
          sum=sum+f3(x)
          x=x+del
 11     continue
        s=0.5d0*(s+(b-a)*sum/tnm)
        it=2*it
        endif
        return
        end


c     ** Collector barrier transmission coefficient subroutine **

      subroutine tr2(Ec,t2)
c     ** data elements **
      double precision alpha , V0, V1, Vcb, k1, k4,F0,
     :    F1, g1g, g1b, g2, g3, g4, g5,Vbe,
     :    b(1:2,1:2), c(1:2,1:2), bzx1,bzx2,gra, coll,
     :    t2, equ1, equ2, equ3, invc(1:2,1:2), a(1:2,1:2),
     :    tmp(1:2,1:2), z1, z2, z3, z4,x,
     :    mAlGag,mAlGab, mbzx1,mbzx2,mbzx3, kappa,
     :    gamma,beta1,beta2,beta3, a1(1:2,1:2),
     :    mrest, mGaAs, ele, Ef, h, pi, hbar, kx, Ec,
     :    Vcbm,I0
      parameter(h=6.626d-34, pi=3.141592654d0, ele=1.602d-19)
      common /block1/ Ef, kx, Vbe, Vcb
```

```
c   ** input parameters **
    hbar = h/(2.00d0*pi)
    mrest = 9.109d-31
    mGaAs = 0.067d0
    mAlGag =0.0795d0
    mAlGab = 0.09d0
    V0 =0.07d0
    V1 =0.210d0
    gra =10.00d0
    coll = 100.00d0
    alpha = 1.00d0/3.00d0
    I0=1.0d0

c   ***** Executable statements *****

    kappa = ((2.00d9*mrest*ele)/(hbar**2.00d0))**alpha
    gamma = ((2.00d0*mrest*ele)/(hbar**2.00d0))**0.50d0
    beta1=mGaAs/mAlGag
    beta2=mAlGag/mAlGab
    beta3=mGaAs/mAlGab

c   *** Positive Vcb ***
    if(Vcb.gt.0.d0)then
c   ** calculate k1 and k4 **
     k1 = gamma*((mGaAs*Ec)**0.50d0)
     k4 = gamma*((mGaAs*(Ec+Vcb))**0.50d0)

c   *** calculate transfer matrix ***

     F0=(Vcb/coll)-((V1-V0)/gra)
     F1 = Vcb/coll
        if (F0.lt.0.d0) then
          F0=dabs(F0)
          I0=-1.0d0
        else
          continue
        endif


     g1g = kappa*1.00d-9*((mAlGag*F0)**alpha)
     g1b = kappa*1.00d-9*((mAlGab*F1)**alpha)

     bzx1 = -1.00d0*kappa*((mAlGag*F0)**alpha)*I0
     bzx2 = - 1.00d0*kappa*((mAlGab*F1)**alpha)
     mbzx1 = bzx1*beta1
     mbzx2 = bzx2*beta2
     mbzx3 = bzx2*beta3


c   ** Define matrix S2(x=0) **
     x = 0.00d0
     g2=((V0-Ec)/F0)-(I0*x)
     z1 = ( g1g*g2)

c   ** Define matrix invS2(x=g) and multiply matrices **
     x = gra
     g3=((V0-Ec)/F0)-(I0*x)
```

```
      z2 = (g1g*g3)

      call matairy(z1,mbzx1,b)
      call matairy(z2,bzx1,c)
      call inmat(c,z2,invc)
      call mulmat(b,invc,a1)

c     ** Define matrix S3(x=g) **
      x =0.00d0
      g4 = ((V1-(F1*gra)-Ec)/F1)-(x)
      z3 = (g1b*g4)

c     ** Define matrix invS3(x=c) and multiply matrices **
      x = coll-gra
      g5 = ((V1-(F1*gra)-Ec)/F1)-(x)
      z4 = (g1b*g5)

      call matairy(z3,mbzx2,b)
      call matairy(z4,mbzx3,c)
      call inmat(c,z4,invc)
      call mulmat(b,invc,a)

      call mulmat(a1,a,tmp)
      a1(1,1) = tmp(1,1)
      a1(1,2) = tmp(1,2)
      a1(2,1) = tmp(2,1)
      a1(2,2) = tmp(2,2)


c     *** Negative Vcb ***
     else
      Vcbm=dabs(Vcb)
      if(Ec.lt.Vcbm)then
        pause'Ec is less than Vcb'
        print*,'Ec=',Ec
        print*,'Vcb=',Vcb
        print*,'Vcbm=',Vcbm
      endif

c     ** calculate k1 and k4 **
      k1=gamma*((mGaAs*Ec)**0.5d0)
      k4=gamma*((mGaAs*(Ec-Vcbm))**0.5d0)

      if(Ec.lt.Vcbm)then
        print*,'k1=',k1
        print*,'k4=',k4
      endif


c     ** calculate transfer matrix **
      F0=(Vcbm/coll)+((V1-V0)/gra)
      F1=Vcbm/coll
      g1g=kappa*1.d-9*((mAlGag*F0)**alpha)
      g1b=kappa*1.d-9*((mAlGab*F1)**alpha)


      bzx1=kappa*((mAlGag*F0)**alpha)
```

```
      bzx2=kappa*((mAlGab*F1)**alpha)
      mbzx1=bzx1*beta1
      mbzx2=bzx2*beta2
      mbzx3=bzx2*beta3

c     ** Define matrix S2(x=0) **
      x=0.d0
      g2=((V0-Ec)/F0)+x
      z1=(g1g*g2)

c     ** Define matrix invS2(x=g) and multiply matrices **
      x=gra
      g3=((V0-Ec)/F0)+x
      z2=(g1g*g3)
      call matairy(z1,mbzx1,b)
      call matairy(z2,bzx1,c)
      call inmat(c,z2,invc)
      call mulmat(b,invc,a1)

c     ** Define matrix S3(x=g) **
      x=0.d0
      g4=((V1+(F1*gra)-Ec)/F1)+x
      z3=(g1b*g4)


c     ** Define matrix invS3(x=c) and multiply matrices **
      x=coll-gra
      g5=((V1+(F1*gra)-Ec)/F1)+x
      z4=(g1b*g5)
      call matairy(z3,mbzx2,b)
      call matairy(z4,mbzx3,c)
      call inmat(c,z4,invc)
      call mulmat(b,invc,a)

      call mulmat(a1,a,tmp)
      a1(1,1)=tmp(1,1)
      a1(1,2)=tmp(1,2)
      a1(2,1)=tmp(2,1)
      a1(2,2)=tmp(2,2)
    endif

c     ** Evaluate t2 **

    equ1 = (4.00d0*k4)/k1
    equ2 = (a1(1,1)+((k4*a1(2,2))/k1))**2.00d0
    equ3 = ((a1(2,1)/k1)-(k4*a1(1,2)))**2.00d0
    t2 = equ1/(equ2+equ3)
    return
    end


    subroutine asyairy(z,ai,bi,aip,bip)
    implicit none
c   uses asymptotic expansions
c   returns Airy functions Ai(z),Bi(z) and their derivatives
c   Ai'(z),Bi'(z)
    double precision absz,rootz,x,ONOVX,PI,ONOVRP,expx,expmx,
```

```
     : zpof,zpmof,chi,ai,bi,aip,bip,c1,d1,z,TWTHR,schi,cchi
      parameter(PI=3.141592654d0,c1=6.9444444d-2,
     :  d1=-9.7222222d-2)
      print*,'asymptotic'
      TWTHR=2.d0/3.d0
      absz=dabs(z)
      rootz=dsqrt(absz)
      x=TWTHR*absz*rootz
      ONOVX=(x)**(-1.d0)
      ONOVRP=1.d0/(dsqrt(PI))
      expx=dexp(x)
      expmx=dexp(-1.d0*x)
      zpof=absz**(1.d0/4.d0)
      zpmof=absz**(-1.d0*(1.d0/4.d0))
      chi=x+(PI/4.d0)
c     print*,'chi=',chi
      schi=dsin(chi)
      cchi=dcos(chi)
c     print*,'schi=',schi
      if (z.gt.0.d0) then
            ai=.5d0*ONOVRP*zpmof*expmx
            bi=ONOVRP*zpmof*expx
            aip=-1.d0*.5d0*ONOVRP*zpof*expmx
            bip=ONOVRP*zpof*expx
      elseif (z.lt.0.d0) then
            ai=ONOVRP*zpmof*(schi-(c1*ONOVX*cchi))
            bi=ONOVRP*zpmof*(cchi+(c1*ONOVX*schi))
            aip=-1.d0*ONOVRP*zpof*(cchi+(d1*ONOVX*schi))
            bip=ONOVRP*zpof*(schi-(d1*ONOVX*cchi))
c           print*,'ai=',ai
c           print*,'bi=',bi
c           print*,'aip=',aip
c           print*,'bip=',bip
      endif
      return
      end
```

Appendix B

Calculations using the "Mathcad" software package.

B.1 Calculation of Band Bending

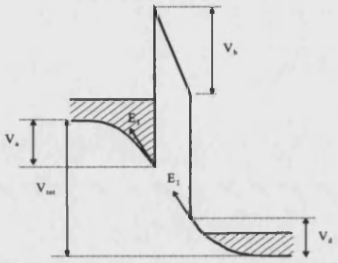

Fig. B.1 A single barrier structure under an appliedbias with band bending at the interfaces included

$$Eg := 13.18 \cdot 8.85 \cdot 10^{-12} \qquad Ea := 10.06 \cdot 8.85 \cdot 10^{-12} \qquad hb := \frac{6.63 \cdot 10^{-34}}{2 \cdot \pi}$$

$$Nd := 1 \cdot 10^{24} \qquad Wb := 15 \cdot 10^{-9}$$

$$e := 1.602 \cdot 10^{-19} \qquad Ef := .054 \cdot e \qquad m := 0.067 \cdot 9.109 \cdot 10^{-31}$$

$$Vbar := .1$$

$$E1 := \frac{Ea}{Eg} \cdot \frac{1}{Wb} \cdot Vbar$$

$$f(Va) := \frac{2}{3 \cdot \pi^2 \cdot Eg} \cdot \left(\frac{2 \cdot m}{hb^2}\right)^{\frac{3}{2}} \cdot \left[\left(\frac{2}{5}\right) \cdot (Ef + e \cdot Va)^{\frac{5}{2}} - \left(Ef^{\frac{3}{2}} \cdot e \cdot Va\right) - \frac{2}{5} \cdot Ef^{\frac{5}{2}}\right]$$

$$Va := 0.04$$

$$root\left[\left(f(Va) - E1^2\right), Va\right] = 0.025$$

$$Va := root\left[\left(f(Va) - E1^2\right), Va\right]$$

$$E1^2 = 2.589 \cdot 10^{13}$$

$$Va = 0.025$$

$$f(Va) = 2.589 \cdot 10^{13}$$

$$Vd := 0.02$$

$$g(Vd) := \frac{2}{3\cdot\pi^2\cdot Eg}\cdot\left(\frac{2\cdot m}{hb^2}\right)^{\frac{3}{2}}\cdot\left[\frac{2}{5}\cdot(Ef - e\cdot Vd)^{\frac{5}{2}} + \left(Ef^{\frac{3}{2}}\cdot e\cdot Vd\right) - \frac{2}{5}\cdot Ef^{\frac{5}{2}}\right]$$

$$Vd := .04267$$

$$root\left[\left(g(Vd) - E1^2\right), Vd\right] = 0.028$$

$$Vd := root\left[\left(g(Vd) - E1^2\right), Vd\right]$$

$$Vd = 0.028 \qquad E1^2 = 2.589\cdot 10^{13}$$

$$g(Vd) = 2.589\cdot 10^{13}$$

B.2 Calculation of subband energies

$$h := 6.626\cdot 10^{-34} \qquad hb := \frac{h}{2\cdot\pi} \qquad e := 1.602\cdot 10^{-19}$$

$$m := 9.1\cdot 10^{-31}\cdot 1.1 \qquad b := 15\cdot 10^{-9} \qquad V0 := 0.35$$

$$Va := 0.225\cdot .62$$

$$F := \frac{Va}{b}$$

$$i := 1..350$$

$$n_i := i \qquad E_i := i\cdot 0.001$$

$$k1_i := \sqrt{\frac{2\cdot m}{hb^2}\cdot\left(V0 - E_i\right)} \qquad k2_i := \sqrt{\frac{2\cdot m}{hb^2}\cdot\left(V0 + Va - E_i\right)}$$

$$gw := \left(\frac{2\cdot m\cdot e\cdot F}{hb^2}\right)^{\frac{1}{3}}$$

$$z0_i := \left(\frac{2\cdot m\cdot e\cdot F}{hb^2}\right)^{\frac{1}{3}}\cdot\left(\frac{-E_i}{F}\right) \qquad za_i := \left(\frac{2\cdot m\cdot e\cdot F}{hb^2}\right)^{\frac{1}{3}}\cdot\left(b - \frac{E_i}{F}\right)$$

$$a1p(n) := \left| \begin{array}{l} j \leftarrow 0 \\ \text{for } i \in n \\ \quad \left| \begin{array}{l} E \leftarrow i \cdot 0.001 \\ z \leftarrow \left(\frac{2 \cdot m \cdot e \cdot F}{hb^2} \right)^{\frac{1}{3}} \cdot \left(\frac{-E}{F} \right) \\ x_j \leftarrow \frac{d}{dz} Ai(z) \\ j \leftarrow j + 1 \end{array} \right. \\ x \end{array} \right.$$

$$b1p(n) := \left| \begin{array}{l} j \leftarrow 0 \\ \text{for } i \in n \\ \quad \left| \begin{array}{l} E \leftarrow i \cdot 0.001 \\ z \leftarrow \left(\frac{2 \cdot m \cdot e \cdot F}{hb^2} \right)^{\frac{1}{3}} \cdot \left(\frac{-E}{F} \right) \\ x_j \leftarrow \frac{d}{dz} Bi(z) \\ j \leftarrow j + 1 \end{array} \right. \\ x \end{array} \right.$$

$K := a1p(n)$

$L := b1p(n)$

$$s1_i := k1_i \cdot Ai(z0_i) - gw \cdot K_i$$

$$s2_i := k1_i \cdot Bi(z0_i) - gw \cdot L_i$$

$$a2p(n) := \left| \begin{array}{l} j \leftarrow 0 \\ \text{for } i \in n \\ \quad \left| \begin{array}{l} E \leftarrow i \cdot 0.001 \\ z \leftarrow \left(\frac{2 \cdot m \cdot e \cdot F}{hb^2} \right)^{\frac{1}{3}} \cdot \left(b - \frac{E}{F} \right) \\ x_j \leftarrow \frac{d}{dz} Ai(z) \\ j \leftarrow j + 1 \end{array} \right. \\ x \end{array} \right.$$

$$b2p(n) := \left| \begin{array}{l} j \leftarrow 0 \\ \text{for } i \in n \\ \quad \left| \begin{array}{l} E \leftarrow i \cdot 0.001 \\ z \leftarrow \left(\frac{2 \cdot m \cdot e \cdot F}{hb^2} \right)^{\frac{1}{3}} \cdot \left(b - \frac{E}{F} \right) \\ x_j \leftarrow \frac{d}{dz} Bi(z) \\ j \leftarrow j + 1 \end{array} \right. \\ x \end{array} \right.$$

$M := a2p(n)$

$N := b2p(n)$

$$s3_i := k2_i \cdot Ai(za_i) + gw \cdot M_i$$

$$s4_i := k2_i \cdot Bi(za_i) + gw \cdot N_i$$

$$A_i := s1_i \cdot s4_i - s2_i \cdot s3_i$$

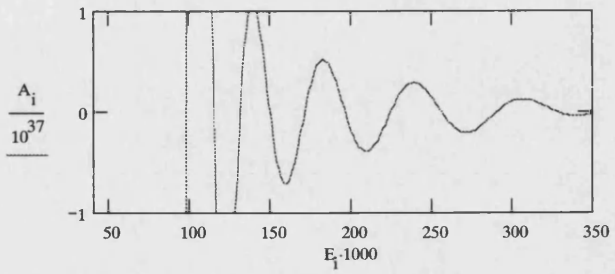

B.3 Calculation of in-plane voltage drop in base

$$m := 0.105 \cdot 9.11 \cdot 10^{-31} \qquad e := 1.6 \cdot 10^{-19}$$

$$hb := \frac{6.63 \cdot 10^{-34}}{2\pi} \qquad EF := 0.055$$

$$w := 15 \cdot 10^{-6} \qquad l := 45 \cdot 10^{-6} \qquad d := 50 \cdot 10^{-9} \qquad z := 15 \cdot 10^{-9} \qquad rho := 2 \cdot 10^{-5}$$

$$V0 := 0.350 \qquad Va := 0.350$$

$$y := \begin{bmatrix} Va \\ 0 \end{bmatrix}$$

$$D(x, y) := \left[\frac{rho}{d} \cdot \frac{m \cdot e^3}{2 \cdot \pi^2 \cdot hb^3} \cdot \int_0^{EF} (EF - EZ) \cdot \exp\left[\frac{-4}{3} \cdot \left(\frac{2 \cdot m \cdot e}{hb^2} \right)^{0.5} \cdot \left(\frac{z}{y_0} \right) \cdot (V0 - EZ)^{1.5} \right] dEZ \right]$$

$$Z := rkfixed(y, 0, w, 100, D)$$

$$n := 0 .. 100$$

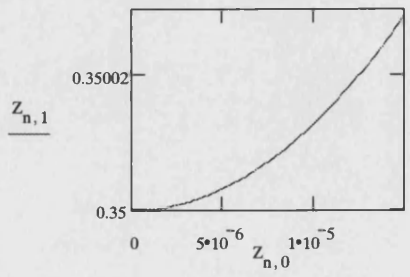

$$J_n := \frac{m \cdot e^3}{2 \cdot \pi^2 \cdot hb^3} \cdot \int_0^{EF} (EF - EZ) \cdot \exp\left[\frac{-4}{3} \cdot \left(\frac{2 \cdot m \cdot e}{hb^2}\right)^{0.5} \cdot \left(\frac{z}{Z_{n,1}}\right) \cdot (V0 - EZ)^{1.5}\right] dEZ$$

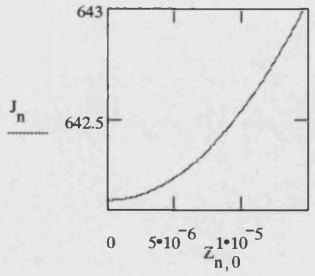

$$IE := \frac{w}{100} \cdot l \cdot \sum_n J_n$$

$$IE = 4.38 \cdot 10^{-7}$$

PRNPRECISION := 7 PRNCOLWIDTH := 15

$O_{n,0} := Z_{n,0}$

$O_{n,1} := Z_{n,1} \cdot 1000$

$O_{n,2} := J_n$

out := "c:\base.dat"

WRITEPRN(out) := O

Appendix C

Evaluation of three-point conductance and its first derivative

Consider a schematic conduction band profile (shown below) of a THETA device under typical biasing condition.

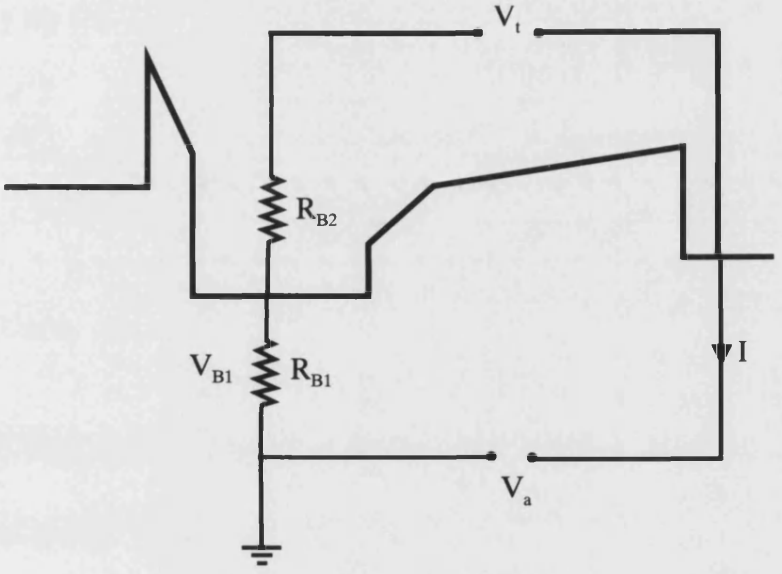

Fig. C.1 Schematic of three-point measurement method

Due to the presence of the series resistances (R_{B1} and R_{B2}) in the base contacts a part of the applied collector-base bias (V_a) drops across R_{B1} while remaining part appears across the collector barrier (V_t).

Let V_{B1} be the voltage drop across R_{B1}.

Using Kirchchoff's circuit rule we write

$$V_a = V_{B1} + V_t \tag{1}$$

The transconductance measured in two-point geometry is given by

$$\frac{dI}{dV_a} = \frac{dI}{dV_t} \times \frac{dV_t}{dV_a} \tag{2}$$

where $\frac{dI}{dV_t}$ is the three-point transconductance.

From equation 1 and 2 we write

$$\frac{dI}{dV_t} = \frac{\frac{dI}{dV_t}}{1 - \frac{dV_{B1}}{dV_a}} \tag{3}$$

similarly the first derivative of the transconductance can be shown to be

$$\frac{d^2I}{dV_t^2} = \frac{\frac{d^2I}{dV_a^2} - \frac{dI}{dV_t} \times \frac{d^2V_t}{dV_a^2}}{1 - \frac{dV_{B1}}{dV_a}} \tag{4}$$

Using data measured in two-point $\left(\frac{dI}{dV_a}, \frac{d^2I}{dV_a^2}\right)$ and three-point geometry $\left(\frac{dV_{B1}}{dV_a}\right)$ three point transconductance $\left(\frac{dI}{dV_t}\right)$ and its first derivative $\left(\frac{d^2I}{dV_t^2}\right)$ can be evaluated using "Mathcad" software.

References

Adachi S., J. Appl. Phys. 58, R1 (1985).

Adachi S. ed., "Properties of Aluminium Gallium Arsenide", Institute of Engineers, London (1993).

Adams A.R., and Dunshan D.J., Semicond. Sci. Technol. 5, 1194 (1990).

Allen S.S., and Richardson S.L., J.Appl. Phys. 79, 886 (1996).

Anderson R.L., Solid State Electron. 5, 341 (1962).

Austing D.G., Klipstein P.C., Higgs A.W., Hutchinson H.J., Smith G.W., Roberts J.S, and Hill G., Phys. Rev. B 47, 1419 (1993).

Batey J., and Wright S.L., J. Appl. Phys. 59, 200 (1986).

Bending S.J., Zhang C., Klitzing K.v., Marclay E., Gueret P., and Meir H.P., Phys. Rev. B 39, 12981 (1989a).

Bending S.J., Bockenhoff E., US patent, US4878095 (1989b).

Bending S.J., Peck A., Leo J., Klitzing K.v., Gueret P., and Meir H.P., Solid State Electron. 32, 1161 (1989c).

Beresford R., Luo L.F., Wang W.I., and Mendez E.E., Appl. Phys. Lett. 55, 1555 (1989).

Blakemore J.S., J. Appl. Phys. 53, R123 (1982).

Blakemore J.S. ed., "Key Papers in Physics Gallium Arsenide", American Institute of Physics, New York (1987).

Bohm D., "Quantum Theory", Dover Publication (1986).

Bonnefoi A.R., Chow D.H., McGill T.C., Burnham R.D., and Ponce F.A., J. Vac. Sci. Technol. B 4, 988 (1986).

Bonnefoi A.R., Chow D.H., and McGill T.C., J.Appl. Phys., 62, 3836 (1987).

Brennan K.F., and Summers C.J., J. Appl. Phys. 61, 614 (1986).

Brill B., and Heiblum M., Phys. Rev. B 49, 14762 (1994).

Brill B., and Heiblum M., Phys. Rev. B 54, R17280 (1996).

Bundy F.P., J. Appl. Phys. 32, 483 (1961).

Carbonneau Y., Beerens J., Cury L.A., Liu H.C., and Buchanan M., Appl. Phys. Lett. 62, 1955 (1993).

Carnahan R.E., Ph.D. Thesis, Georgia Institute of Technology (1994).

Chandra A., and Eastman L.F., J. Appl. Phys. 53, 9165 (1982).

Chang L.L., Esaki L., and Tsu R., Appl. Phys. Lett. 24, 593 (1974).

Delagebeaudeuf D., Delescluse P., Delescluse P., Etienne P., Massies, Laviron M., Chaplart J., and Linh T., Electron. Lett. 18, 85 (1982).

Dellow M.W., Cronin N.J., Bending S.J., Appl. Phys. Lett. 65, 2463 (1994).

Duke C.B., "Tunneling in Solids", Academic Press, New York (1969).

Ermets M.I., "High Pressure Experimental Methods", Oxford University Press, Oxford (1996).

Esaki L., Phys. Rev. 109, 603 (1958).

Esaki L., and Tsu R., IBM J. Res. Develop. 60 (1970).

Esaki L., in "Physics and Application of Quantum Wells and Superlattices", Mendez E.E., and Klitzing K.v. eds., Plenum Press, New York (1987).

Finley J.J., Teissier R.J., Skolnick M.S., Cockburn J.W., Grey R., Hill G., and Pate M.A., Surf. Sci. 361/362, 197 (1996).

Finley J.J., Teisser R.J, Skolnick M.S., Cockburn J.W., Roberts G.A., Grey R., Hill G.,Pate M.A., and Planel R., Phys. Rev. B 58, 10619 (1998).

Frensley W.R., in " Heterostructure and Quantum Devices", Einspruch N.G., and Frensley W.R. eds., Academic Press, San Diego (1994).

Fowler R.H., and Nordheim L., Proc. Roy. Soc. (London) A119, 173 (1928).

Gamow G., Z. Physik 51, 204 (1928).

Geim A.K., Bending S.J., Gueret P., and Meir H.P., Appl. Phys. Lett. 61, 3157 (1992).

Giaever I., Phys. Rev. Lett. 5, 147 (1960).

Gunn J.B., Solid State Commnui. 1, 91 (1963).

Hase I., Kawaki H., Kaneko K., and Wantanabe N., Electron. Lett. 20, 491 (1984).

Hase I., Kawai H., Imanaga S., Kaneko K., Wantanabe N., Electron. Lett. 21, 757 (1985).

Hase I., Kawaki H., Kaneko K., and Wantanabe N., J. Appl. Phys. 59 3792 (1986).

Hayes J.R., Levi A.F.J., and Wiegmann W., Electron. Lett. 20, 851 (1984).

Hayes J.R., Levi A.F.J., and Wiegmann W., Phys. Rev. Lett. 54, 1570 (1985).

Hayes J.R., and Levi A.F.J., IEEE J. Quna. Electron. QE-22, 1744 (1986).

Hatzakis M., Canavello B.J., and Shaw J.M., IBM J. Res. Develop. 24, 452 (1980).

Heiblum M., Solid-State Electron. 24, 343 (1981).

Heiblum M., Nathan M.I., and Chang C.A., Solid-State Electron. 25, 185 (1982).

Heiblum M., Nathan M.I., Thomas D.C., and Knoedler C.M., Phys. Rev. Lett. 55, 2200 (1985a).

Heiblum M., Thomas D.C., Knoedler C.M., and Nathan M.I., Appl. Phys. Lett. 47, 1105 (1985b).

Heiblum M., Anderson I.M., and Knoedler C.M., Appl. Phys. Lett. 49, 207 (1986a).

Heiblum M., Calleja E., Anderson I.M., Dumke W.P., Knoedler C.M., and Osterling L., Phys. Rev. Lett. 56, 2854 (1986b).

Heiblum M., Fischetti M.V., Dumke W.P., Frank D.J., Anderson I.M., Knoedler C.M., and Osterling L., Phys. Rev. Lett. 58, 816 (1987).

Heiblum M., Seo K., Meier H.P., and Hickmott T.W., Phys. Rev. Lett. 60, 828 (1988).

Heiblum M., Galbi D., and Weckwerth M., Phys. Rev. Lett. 62, 1057, (1989).

Heiblum M., and Fischetti M.V., in "Physics of Quantum Electron Devices", Capasso F. ed., Springer-Verlag, Berlin (1990).

Hesto P., Pone J-F., and Castagne R., Appl. Lett. 40, 405 (1982).

Hollis M.A., Plamateer S.C., Eastman L.F., Dandekar N.V., and Smith P.M., Electron. Dev. Lett. 4, 440 (1983).

Jacobini C., Lugli P., "The Monte Carlo Method for Semiconductor device Simulation", Springer-Verlag, Wien (1989).

Jaros M., "Physics and Application of Semiconductor Microstructures", Oxford (1990).

Josephson B.D., Phys. Rev. Lett. 1, 251 (1962).

Kaya I.I., Dellow M.W., Bending S.J., Linfield E.H., Rose P.D., Ritchie D.A., and Jones G.A.C., Semicond. Sci. Technol. 11, 135 (1996).

Kelly M.J., Electron. Lett. 20, 771 (1984).

Kelly M.J, "Low dimensional Semiconductors Materials, Physics, Technology, Devices", Oxford (1995).

Kirkpatrick C.G., Chen R.T., Holmes D.E., and Elliott K.R., in "Gallium Arsenide Materials, Devices, and Circuits", Howes M.J., and Morgan D.V. eds., John Wiley & sons, Chichester (1986).

Kisaki H., Proc. IEEE, 61, 1053 (1973).

Kitano T., Izumi S., Minami H., Ishikawa T., Sato K., Sonoda T., and Otsubo M., J. Vac. Sci. Technol. B 15, 167 (1997).

Lam V.H.Y., Dellow M.W., Bending S.J., Arent D.J., and Gueret P., Condensed Matter and Material Physics Conference (1993).

Lam V.H.Y., Dellow M.W., Bending S.J., Elliott M., Arent D.J., and Gueret P., Semicon. Sci. Technol. 10, 110 (1995).

Landheer D., Liu H.C., Buchanan M., and Stoner R., Appl. Phys. Lett. 54, 1784 (1989).

Larson L.E., Jensen J.F., and Greiling P.T., Computer 19, 21, (1986)

Levi A.F.J., Hayes J.R., Platzman P.M., and Wiegmann W., Phys. Rev. Lett. 55, 2071 (1985).

Lilienfeld J.E., Z.Physik 23, 506 (1922).

Long A.P., Beton P.H., Kelly M.J., and Kerr T.M., Electron. Lett. 22, 130 (1986).

Madelung O. ed., "Semiconductors Group IV Elements and III-V Compounds", Springer-Verlag (1991).

Mathews P., Kelly M.J., Hasko D.G., Peper M., Ahmed H., Peacock D.C., Frost J.E.F., Ritchie D.A., and Jones G.A.C., Electron. Lett. 26, 863, (1990a).

Mathews P., Kelly M.J., Law V.J., Hasko D.G., Peper M., Stobbs W.M., Ahmed H., Peacock D.C., Frost J.E.F., Ritchie D.A., and Jones G.A.C., Phys. Rev. B 42, 11415 (1990b).

Mead C.A., Proc. IRE 48, 359 (1960).

Mendez E.E, Calleja E., and Wang W.I, Phys. Rev. B 34, 6026 (1986).

Mendez E.E, in "Physics and Application of Quantum Wells and Superlattices", Mendez E.E., and Klitzing K.v. eds., Plenum Press, New York (1987).

Mendez E.E, Chang L.L., Surf. Sci., 173 (1990).

Moreau W.M., "Semiconductor Lithography", Plenum Press, New York (1988).

Mori T., Ohnishi H., Imamura K., Muto S., and Yokoyama N., Appl. Phys. Lett. 48, 1779 (1986).

Oppenheimer J.R., Phys. Rev. 31, 66 (1928).

Osburn G.C., J. Vac. Sci. Technol. 17, 1104 (1980)

Othaman Z., Geim A.K, Bending S.J, Syme R.T., and Smith R.S, Semicond. Sci. Technol. 8, 1483 (1993).

Othamann Z.B., Ph.D. Thesis, University of Bath (1995).

Palevski A., Heiblum M., Umbach C.P., Knoedler C.M., Broers A.N., and Koch R.H., Phys. Rev. Lett. 62, 1776 (1989a).

Palevski A., Umbach C.P.,Heiblum M., Appl. Phys. Lett 55, 1421 (1989b).

Pavesi L., and Guzzi M., J. Appl. Phys. 75, (1994).

Petrov M.V., Parihar S.R., and Lyon S.A., Phys. Rev. B 54, 13869 (1996).

Rauch C., Strasser G., Unterrainer K., Hvozdara L., Boxleitner W., Gornik E., Brill B., Meirav U., Superlatt. and Microstructu., 22, 143 (1997).

Robert J.L., Mercy J.M., Bousquet C., and Raymond A., in "Two dimensional systems, Heterostructures and Superlattices", Baur G., Kuchar F., and Heinrich H. eds., Springer Verlag, Berlin (1984).

Rossmanith M., Syassen, Böchenhoff E., Ploog K., and Klitzing K.v., Phys. Rev. B 44, 3168 (1991).

Rossmanith M., Syassen, Böchenhoff E., Ploog K., and Klitzing K.v., Appl. Phys. Lett. 63, 937 (1993).

Sekiguchi Y., Kuwahara T., Kobayashi F., and Iio S., Jpn. J. Appl. Phys. 3 L180 (1992).

Shannon J.M., IEE. J. Solid-st. Electron. Dev. 3, 142 (1979).

Shur M.S., and Eastman L.F., Solid State Electron. 24, 11 (1981).

Singh J., "Semiconductor Devices: An Introduction", McGraw-Hill, New York, (1994).

Solomon P.M., in "The Physics and Fabrication of Microstructures and Microdevices", Kelly M.J., and Weisbuch C. eds., Springer-Verlag, Berlin (1986).

Spratt J.P., Schwarz R.F., and Kane W.M., Phys. Rev. Lett. 6, 341 (1961).

Sprinzak D., Heiblum M., Levinson Y., and Shtrikman H., Phys. Rev. B 55, R10185 (1997).

Sze S.M., "Physics of Semiconductor Devices", Jonh Wiley & Sons, New York (1981).

Sze S.M., "Semiconductor Devices, Physics and Technology, Jon wiley & Sons, New York (1985).

Teisser R.J., Finley J.J., Skolnick M.S., Cockburn J.W., Pelouard J.-L, Grey R., Hill G.,Pate M.A., and Planel R., Phys. Rev. B 54, R8329 (1996).

Thompson J.D., Rev. Sci. Instrum. 55, 231 (1984).

Tsu R.and Esaki L., Appl. Phys. Lett., 22, 562 (1973).

Weill A., in "The Physics and fabrication of microstructures and microdevices", Kelly M.J., and Weisbuch C., eds., Springer-Verlag, Berlin (1986).

Weisbuch C. and Vinter B.' "Quantum Semiconductor Structure", Academic Press, London (1991).

Wight D.R., in "Gallium Arsenide Materials, Devices, and Circuits", Howes M.J. and Morgan D.V. eds., John Wiley & sons, Chichester (1986).

Williams R.E., " Gallium Arsenide Processing Techniques, Artech House Inc. (1984).

Yokoyama N., Imamura K., Ohshima T., Nishi H., Muto S., Kondo K., and Hiyamizu S., Jpn. J. Appl. Phys. 23, L311 (1984).

Yokoyama N., Imamura K., Muto S., Hiyamizu S., and Nishi H., Jpn. J. Appl. Phys. 23, L853 (1985).

Yu E.T., McCaldin J.O., and McGill T.C., in Solid State Physics 46, Academic Press, Boston (1992).